REVIEW PAPER

Review of Environmental Monitoring by Means of Radio Waves in the Polar Regions: From Atmosphere to Geospace

Lucilla Alfonsi[1] · Nicolas Bergeot[2] · Pierre J. Cilliers[3] · Giorgiana De Franceschi[1] ·
Lisa Baddeley[4] · Emilia Correia[5,6] · et al. [full author details at the end of the article]

Abstract

The Antarctic and Arctic regions are Earth's open windows to outer space. They provide unique opportunities for investigating the troposphere–thermosphere–ionosphere–plasmasphere system at high latitudes, which is not as well understood as the mid- and low-latitude regions mainly due to the paucity of experimental observations. In addition, different neutral and ionised atmospheric layers at high latitudes are much more variable compared to lower latitudes, and their variability is due to mechanisms not yet fully understood. Fortunately, in this new millennium the observing infrastructure in Antarctica and the Arctic has been growing, thus providing scientists with new opportunities to advance our knowledge on the polar atmosphere and geospace. This review shows that it is of paramount importance to perform integrated, multi-disciplinary research, making use of long-term multi-instrument observations combined with ad hoc measurement campaigns to improve our capability of investigating atmospheric dynamics in the polar regions from the troposphere up to the plasmasphere, as well as the coupling between atmospheric layers. Starting from the state of the art of understanding the polar atmosphere, our survey outlines the roadmap for enhancing scientific investigation of its physical mechanisms and dynamics through the full exploitation of the available infrastructures for radio-based environmental monitoring.

Article Highlights

- The polar regions are open windows to outer space, providing unique observations of geospace, and of the ionized and neutral atmosphere
- Many instruments and a multidisciplinary approach are crucial for making improvements in our observing and modelling capabilities
- The full exploitation of recent research infrastructures and an identification of common actions will address important scientific questions

🖄 Springer

1 Introduction

The polar regions are natural laboratories that provide the opportunity to carry out scientific observations and experiments that cannot be performed elsewhere. The Arctic and Antarctica are preferred sites for investigating the physics of solar–terrestrial interaction and the atmosphere because the atmosphere at the polar regions is open to the direct entrance of solar particles and has been demonstrated to be highly sensitive to anthropogenic as well as natural causes of global climate change. These exceptional peculiarities pertain to both polar regions. Among the six priorities for Antarctic science described by Kennicut et al. (2014), two are related to the atmosphere and the geospace, namely to "define the global reach of the Antarctic atmosphere and the Southern Ocean" and to "observe space and the universe". Moreover, for what concerns the Arctic, both the atmosphere and geospace offer valid contributions to the understanding of the science of climate change, being a pillar of the European Arctic policy (https://eeas.europa.eu/arctic-policy/eu-arctic-policy_en).

Cooperation and teamwork are the common threads of all international efforts dedicated to facilitate scientific research in the polar regions while at the same time keeping the operations sustainable with due consideration of the fragile nature of polar environment. Indeed, all the nations that are interested in operating on the Antarctic continent must comply with the Antarctic Treaty (https://ats.aq/documents/keydocs/vol_1/vol1_2_AT_Antarctic_Treaty_e.pdf), which regulates the types of activities that can be carried out. The treaty conception lies in curbing the race to conquer and profit in any form from a still inviolate land. Instead, the treaty supports the performance of peaceful scientific experiments, stimulating collaboration among the nations, aimed at sharing efforts and scientific discoveries for the benefit of humanity. Since the discovery of the Arctic and of Antarctica, a large number of scientists have spent their lives to advance the knowledge of peculiar phenomena occurring uniquely in the polar regions, such as the aurorae. The collaborative investigations conducted during the International Polar Years (IPY) held in 1882–1883, 1932–1933, 1957–1958, and 2007–2009 united thousands of scientists from all over the world around a broad variety of disciplines, from physics to social sciences. The IPY programmes have significantly facilitated data and infrastructures sharing, favouring the establishment of common platforms that, in recent years, developed into e-platforms (such as databases, repositories, and access portals). Under the IPY programmes, the physics of the atmosphere and the solar–terrestrial interactions were among the high priority fields of study, and during IPY 2007–2009 the ICESTAR (Interhemispheric Conjugacy Effects in Solar-Terrestrial and Aeronomy Research) Scientific Research Program, endorsed by the Scientific Committee on Antarctic Research (SCAR, https://scar.org/), highlighted the advantages of the interhemispheric approach for a better understanding of the polar atmosphere (Alfonsi et al. 2008a). Since then, the research on the solar–terrestrial interaction and the atmosphere proceeded with a more pronounced global view, looking at the connections between the poles (see, e.g. Feng et al. 2020; Jin and Xiong 2020; Kim 2021; Reidy et al. 2018; Smith et al. 2020; Swarnalingam et al. 2022), as in the case of the SCAR Expert Group GRAPE (GNSS Research and Application for Polar Environment, http://grape.scar.org/). Thanks to the collaborations matured within GRAPE and extended to closely related fields of expertise, we are now able to gather contributions from a significant part of the scientific community to deal with the physics of the lower and upper atmosphere in the polar regions and to critically review the current capabilities. Our survey moves from a recent white paper (Bergeot et al. 2020) to a broad overview representative of the international efforts dedicated to optimise and maximise what can be gained by the scientific

community in the framework of geospace and of atmospheric research in the polar regions. This review aims to identify gaps in the knowledge to stimulate further collaborations among individuals and institutions and encourage the synergism of polar researcher efforts. The final goal is to inform and inspire the next generation of polar scientists.

Section 1 of this paper surveys the polar research infrastructures. Section 2 analyses scientific contributions of long-term (years) continuous data series covering solar cycles 23 and 24. Section 3 focuses on case studies and main findings of selected events occurring during solar cycles 23 and 24. Sections 2 and 3 also include original results to support and integrate past achievements published in the open literature. The paper closes with a summary of the capacities gained to date and presents a gap analysis to highlight what is still missing in order to draw a possible roadmap for pursuing polar geospace and atmospheric research.

2 Infrastructure at Polar Latitudes

The International Geophysical year 1957–1958 (IGY, Chapman 1959), the International Polar Year 2007–2008 (IPY, Krupnik et al. 2011), and International Heliophysical Year 2007 (IHY, Davila et al. 2006) left an important heritage in terms of network instrumentation, data sharing, expertise exchange, and increasing awareness of the current scientific capabilities. This led to an increasing interest in ground networks of GNSS (Global Navigation Satellite Systems) stations (e.g. POLENET, IGS Wilson et al. 2008; Dow et al. 2009; Jiao and Morton 2015), ionosondes and digisondes (e.g. GIRO, Reinisch and Galkin 2011), HF (High Frequency) backscatter radars (e.g. SuperDARN, Greenwald et al. 1995; Chisham et al. 2007, Nishitani et al. 2019), Ultra-High or Very High Frequency (UHF, VHF) incoherent scatter radars (e.g. EISCAT, Rishbeth and Williams 1985; RISR, Gillies et al. 2016; EISCAT_3D), Very Low Frequency (VLF) radio receivers (Thomson et al. 2007), auroral imagers with all-sky, medium or narrow fields of view (e.g. MIRACLE, ALIS, Brändström et al. 1999; Brändström 2003, etc.), and magnetometers (INTERMAGNET and SuperMAG, Gjerloev 2009; Love and Chulliat; 2013). The number of ionospheric scintillation monitors receivers (ISMRs) (e.g. EDAS, Peng and Morton, 2013), VLF antennas (e.g. AWDAnet, Lichtenberger et al. 2008), High-Power Large Aperture (HPLA) radars, and microwave humidity sounders are growing through both national and international initiatives, and existing instrumentation is also being replaced or upgraded. One such major replacement is EISCAT_3D, which is planned to become operational during 2023. In this section, we describe the current state of the research infrastructures/networks (Fig. 1) that are used to study the geospace environment and the atmospheric neutral components at high latitudes.

2.1 GNSS for Atmospheric Monitoring

GNSS networks are widely used for atmospheric research purposes. Using multi-frequency receivers, tropospheric water vapour, also called precipitable water (PW), and ionosphere-plasmasphere parameters (e.g. Total Electron Content, TEC, and ionospheric scintillation) can be retrieved (e.g. Pezzopane et al. 2019). Several GNSS networks are now available over polar regions. The networks have grown since the beginning of the twenty-first century thanks to the IPY 2007–2008. Presently, many Antarctic and Arctic GNSS stations form part of a multinational consortium called POLENET (http://polenet.org/), which
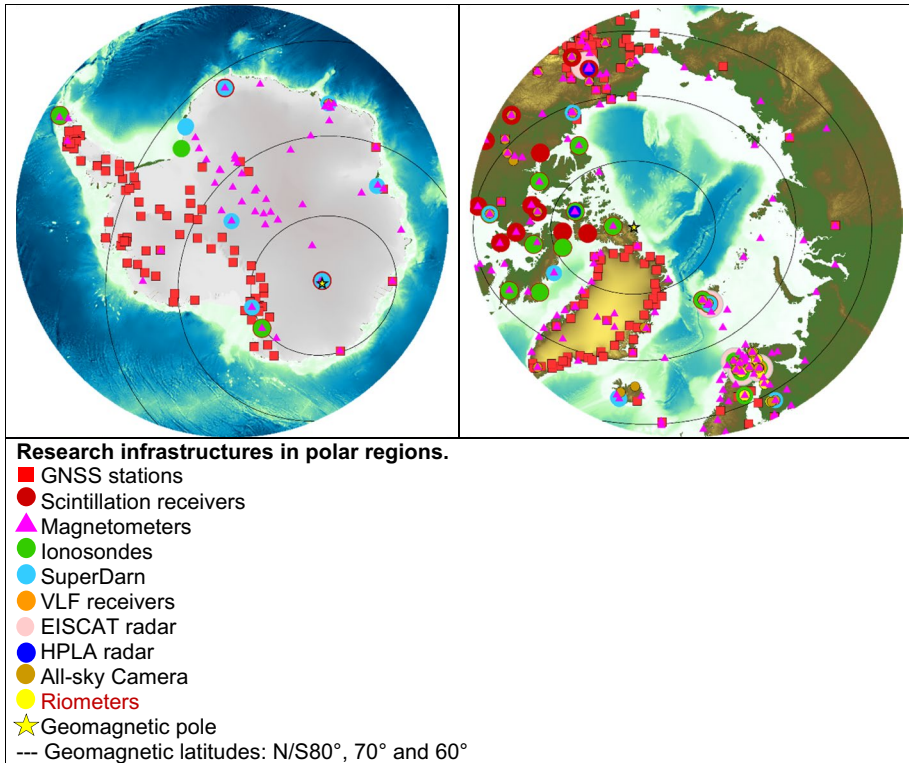
Fig. 1 Scientific instrumentation infrastructure in Antarctica and Arctic regions (selected established stations to indicate the coverage of measurements)

delivers long-term and campaign data. Other important networks include the International GNSS Service (IGS) network (Dow et al. 2009) and UNAVCO network (https://www.unavco.org/data/gps-gnss/gps-gnss.html) that are dedicated to geodesy purposes.

The exploitation of GNSS signals for ionospheric monitoring opens a new area and facilitates the study of ionospheric scintillation. Several manufacturers produced ionospheric TEC and scintillation monitor receivers for scientific uses, e.g. Novatel GPStation6, Septentrio PolaRx5S. These ISMRs provide ionospheric scintillation indices (originally defined using single-frequency receiver by Van Dierendonck et al. 1993), as measured by dual (GSV4004) or multi-frequency (Septentrio PolaRxS) high rate (50 Hz) receivers as well as conventional geodetic data in the standard RINEX format. Among the retrieved parameters, the most used are the phase scintillation index (σ_Φ) and the amplitude scintillation index (S4), provided by the receivers' firmware over different time intervals (1, 3, 10, 30, 60 s) but usually taken over 1 min, the slant and the vertical uncalibrated TEC (sTEC and vTEC, respectively), calculated every 15 s, and the Relative TEC (ROT) calculated every 15 s.

To our knowledge, the first ISMRs were installed in 2001 in northern Europe by the Institute of Engineering Surveying and Space Geodesy (IESSG) of the University of Nottingham. Their network covered the region from 53° N to 70° N (Aquino et al. 2005). The longest data series of the same type at high latitudes have been collected by INGV through

receivers deployed in the Arctic (Ny-Ålesund and Longyearbyen, Svalbard) and Antarctica (Mario Zucchelli station, Concordia station, and SANAE station) that started their operations in 2003 and are still working (De Franceschi et al. 2006, 2019). In Canada, the Canadian Geodetic Survey of Natural Resources Canada provides regional and global TEC maps and monitors ionospheric GNSS phase irregularities using real-time IGS high rate network (Ghoddousi-Fard 2011, 2014), also the CHAIN (Canadian High Arctic Ionospheric Network) at the University of New Brunswick has been delivering TEC and scintillations parameters since 2008 (Jayachandran et al. 2009).

Another approach to study the GNSS signals is by the reconfigurable software-defined radios (SDR). For example, the Satellite Navigation and Sensing (SeNSe) Lab at the University of Colorado Boulder has established a network of event-driven data acquisition systems (EDAS) for ionospheric scintillation and space weather monitoring. Its core component is an array of reconfigurable software-defined radios (SDR) that samples all open GNSS signals at 25 MHz (Peng and Morton, 2013). Because of the high sampling rate of EDAS, a real-time, event-driven architecture was implemented to store the raw baseband samples only when major disturbances in the signals are detected. The detection is accomplished by a machine learning algorithm operating on measurements generated from a Continuously operating Data Acquisition System (CDAS, Jiao et al. 2017a,b). The CDAS outputs are used as inputs to the machine learning algorithm to detect space weather events, satellite signal anomalies, as well as radiofrequency interferences (RFI), to trigger the SDR data storage operation when a signal disturbance event is detected, and to alert the remote monitoring centre of the event.

2.2 Riometer for detecting D-region ionisation events

The Relative Ionospheric Opacity Meter (Riometer) is designed to monitor the cosmic radio noise from the galaxy, typically at frequencies of 30–40 MHz. The diurnal variation in the cosmic background noise at any given location is a stable sidereal-time periodic function called the Quiet-Day Curve (QDC). Hence, all reductions in the received power from its QDC levels can be used as a measure for the relative Cosmic Noise Absorption (CNA) in the ionosphere. The CNA is fundamentally caused by Joule heating of the free electrons in the collisional plasma, and therefore, the observed CNA serves as a measure for the excess ionisation occasionally taking place in the collisional D-region ionosphere. The ionisation can be caused by either energetic particle precipitation (electrons and protons), especially in the high latitudes, or by excess photoionisation (Solar X-ray flares) in the dayside ionosphere. The majority of the CNA events are associated with energetic particle precipitation at energies of $E > 30$ keV.

A typical riometer setup is either a wide beam or an imaging riometer. Wide-beam riometer chains in the Northern hemisphere are found in the Fennoscandian sector operated by Sodankylä Geophysical Observatory (https://www.sgo.fi/Data/Riometer/riometer.php), and in Canada maintained by the University of Calgary (https://aurora.phys.ucalgary.ca/norstar/rio/index.html, Rostoker et al. 1995) and Natural Resources Canada (Fiori and Danskin 2016). In addition, Tromsø Geophysical Observatory runs similar instruments in Skibotn in Northern Norway, in Ny-Ålesund, and in Longyearbyen (http://www.tgo.uit.no/riometer/index.html). Furthermore, a newly deployed pan-Arctic ground-based network of riometers is an integral part of the PWING chain (http://www.isee.nagoya-u.ac.jp/dimr/PWING/en/), which is the ground component of the ERG spacecraft mission. In Antarctica, at least the Syowa station of the National Institute of Polar Research in Japan

conducts long-term CNA monitoring (http://polaris.nipr.ac.jp/~uap-mon/uapm/ATLAS. html). Two imaging riometers (arrays of narrow-beam antennas) are operated in the mainland Fennoscandia, at Kilpisjärvi and Andenes, by the University of Lancaster (Browne et al. 1995) as well as another two in Svalbard, at Longyearbyen (no longer available) and Ny-Ålesund, maintained by the Technical University of Denmark (Stauning et al. 1996) and the Polar Research Institute of China, respectively. The newest member in the riometer family is a radio receiving system Kilpisjärvi Atmospheric Imaging Receiver Array (KAIRA), at Kilpisjärvi (McKay et al. 2015), which forms an interferometric image of a CNA at a single frequency (38.1 MHz) and in addition 22 individual beams over the sky covering the whole frequency range of 17–59 MHz. The multi-frequency capability, called "spectral riometry", has several advantages, most notably robustness against artificial Radio Frequency Interference (RFI) occurring often in limited frequency bands, as observing the whole frequency spectrum enables reconstruction of the CNA over the interferences either by a simple interpolation or by fitting the theoretical absorption spectrum to the observed data (see, Kero et al. 2014). The Finnish riometer chain operated by the Sodankylä Geophysical Observatory has recently had the traditional La Jolla riometers (30.0 and 32.4 MHz) replaced by new wide-beam spectral riometers measuring over the band of 20–55 MHz with a dense frequency resolution (Fig. 2). Additionally the Swedish
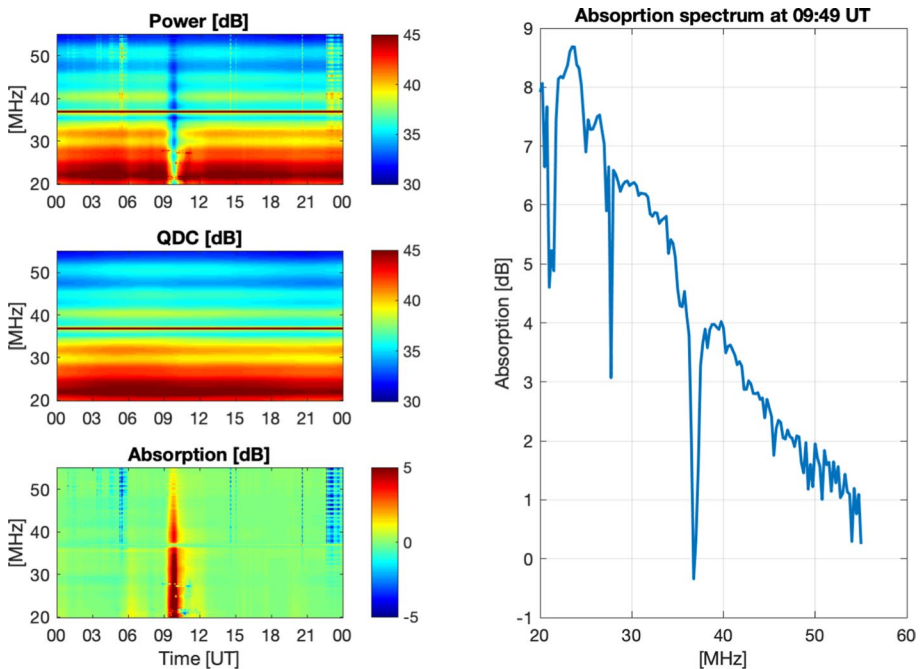

Fig. 2 An example of spectral riometer data (Sodankylä, Feb 16 2021). The upper left panel shows the received cosmic radio noise power in decibels over the whole frequency band 20–55 MHz and the middle panel illustrates the corresponding QDC in the same decibel scale. The lowermost left panel shows the absorption (QDC-Power). The right panel shows a typical absorption spectrum at the peak of the CNA event (09:49 UT). The data contains several frequencies associated with RFIs that result in peaks of "reduced" or even "negative" absorption, most notably the one at 38 MHz caused by the nearby meteor radar. These RFIs can be easily excluded from the spectral riometry data by a simple interpolation over the RFI outliers unlike in the traditional single-frequency riometry

Institute of Space Physics has recently replaced its two La Jolla riometers at Kiruna and Lycksele with two wide-beam, wide-band SDR riometers of the Finnish design (https://www.rfsorcerers.com/img/file.php?id=54804). These are now located at the Tjautjas ALIS station (moved from Kiruna to minimise RFI) and the Lycksele ionospheric observatory. At SANAE-IV in Antarctica, an 8×8 beamforming riometer at 38.2 MHz, and two wide-angle riometers at 30.0 MHz and 51.4 MHz have been operated as part of the South African National Antarctic Programme since April 1997; the imaging riometer at 38.2 MHz was decommissioned in December 2019 and is no longer available. At Comandante Ferraz, the Brazilian Antarctic Station in King George Island, two wide-angle riometers at 30.0 MHz and 38.2 MHz have been operated since March 2009. Other riometers in Antarctica are, for example, operating at stations Maitri, Halley and ZongShan.

The scientific community providing riometer data is renewing the collaboration through the Global Riometer Array (GLORIA) initiative (Alfonsi et al. 2008a) to provide a common platform for sharing data. The platform is currently under development.

2.3 Ionosondes for the Vertical Sounding of the Ionosphere

Ionosondes use a low-power HF transmitter to transmit a series of pulsed or chirped frequency sweeps, generally ranging from 0.1 to 30 MHz over 1 or 2 min. The HF signal, once transmitted into the ionosphere, undergoes mode splitting into O- or X-mode polarisation with respect to the magnetic field. Additionally, the propagation through the ionised medium of the ionosphere depends on the frequency of the transmitted signal, f_t and on the natural frequency of the ionospheric plasma (the so-called plasma frequency, f_p), which has the following relationship with the electron density (n_e):

$$f_p = \omega_p / 2\pi = \left(\frac{n_e e^2}{m_e \epsilon_0} \right)^{\frac{1}{2}} / 2\pi$$

with e being the electron charge, m_e the electron mass, and ϵ_0 the permittivity of free space.

In the case of the O-mode polarisation, at the altitude where the frequency of the transmitted signal is approximately equal to the plasma frequency, $f_t \approx f_p$, the radar beam can be totally or partially reflected. The ionospheric echo intensity is detected for a range of time delays (or virtual ranges) at each radio frequency, f_t. This is called an ionogram. Some ionosondes produce only O-mode ionograms, whereas others also receive the X mode polarisation. From the ionograms, the critical frequencies of the ionospheric E and F layers and the heights of those layers can be read out. This procedure is usually referred to as ionogram scaling. Using an inversion procedure, it is also possible to obtain the vertical electron density profile. Four main types of ionosonde are in use: the simple pulsed ionosonde, which originally showed echo delay time versus transmitted frequency on an oscilloscope (which was then imaged on photographic film), is the original type. Such instruments have been running continuously e.g. in Northern Finland since the International Geophysical Year 1957 and represent some of the longest-running ionospheric measurements in the world. The ionosonde at Sodankylä was replaced by a CW chirp sounder in 2005. This instrument has separate transmitter and receiver locations and transmits a continuous frequency sweep while receiving simultaneously. The received linearly polarised signals are combined into the O- and X-mode circular polarisations, and a windowed FFT is then applied to produce the ionogram. This instrument runs one sounding per minute. The sampling rate is 500 kHz and the frequency range is 500 kHz–16 MHz. Other chirp

sounders also exist, some of which are military instruments. Other more 'modern' versions of the ionosondes are the dynasonde and digisonde. A dynasonde uses the raw data of the received signal to conduct real-time analysis without resorting to FFTs. These instruments typically have spaced receiver antennas and several receiver channels. Parameters that can be derived include Doppler velocity and electron density profiles, and directions of echo arrival (Zabotin et al. 2006 and references therein). A digisonde uses pulse phase modulation and pulse compression to correlate the received signal with the transmitted pulse. In addition to electron density, it is also possible to obtain Doppler velocity and angle of arrival information if a set of multiple antenna units are used (Reinisch et al. 2009).

There are several ionosonde, dynasonde and digisonde systems either currently in operation or previously having provided long-term datasets across the polar region. Their relatively low power and maintenance make them ideal instruments for remote locations. The fast temporal resolution (1–2 min generally, although some can operate at sub-minute intervals) makes it possible to reveal rapid changes in the ionosphere (Enell et al. 2016), as well as ionospheric plasma- wave dynamics and meteor echoes (Kozlovsky et al. 2018; MacDougall and Jayachandran 2005; Verhulst et al. 2017).

Across the northern polar regions, there are several ionosonde networks such as CHAIN, with six active ionosondes across Northern Canada, as well as individual active stations, e.g. at Tromsø (69.66 N, 18.94E, https://dynserv.eiscat.uit.no/, 1995-present), at Sodankylä Geophysical Observatory (67.37 N, 26.63E, https://www.sgo.fi/Data/RealTime/ionogram.php 1957-present), at Kiruna, Lycksele and Uppsala by the Swedish Institute of Space Physics ionosondes (https://www.irf.se/en/observatory-activities/ionosondes/), and at Eielson, Alaska (64.4 N, 147 W, USA).

Historically there have also been stations in Svalbard (Norway, 78.2 N, 15.9E: CADI ionosonde: 1997–2014; EISCAT dynasonde: 2009–2015; CADI ionosonde: 2020 -), at Qaanaaq (77.5 N 290.8, Greenland), at the Comandante Ferraz Brazilian Antarctic Station (62.11S, 58.41 W, 2009–2015, 2022 -) and at Mario Zucchelli Station (74.7S, 164.1E) (operated by INGV till 2012), amongst others. Several of these stations will soon be working again. Data from a large number of these systems are available online.

In the southern polar regions we mention also the digisondes operating at Zhong Shan station by the Center for Space Science and Applied Research of the Chinese Academy of Sciences, and at Jang Bogo by the Korea Polar Research Institute (whose data are available at https://giro.uml.edu/didbase/), and the ionosondes operating at Casey (66.30S, 110.50E), Mawson (67.60S, 62.88E), Davis (68.58S, 77.96E) and Scott Base (77.80S, 166.80E) by the Space Weather Service of the Australian Government Bureau of Meteorology (https://www.sws.bom.gov.au/World_Data_Centre/2/1/28). It is also worth mentioning the US network, including the ionosonde located at South Pole station, the Halley station ionosonde run by the British Antarctic Survey, the ionosonde operated at the French station of Dumond D'Urville. The global ionosonde network (Fig. 3) has contributed to decades of time-series data of the polar ionosphere. A full list of stations and data availability can be found here: https://www.ngdc.noaa.gov/stp/IONO/ionohome.html.

The global distribution of ionosondes also offers the major data source for the International Reference Ionosphere (IRI) model (http://irimodel.org/) which is used throughout the world by atmospheric research communities as well as in real-time modelling of the ionosphere (see, e.g., http://madrigal.haystack.mit.edu/models/IRI/index.html). The Empirical Canadian High Arctic Ionospheric Model (E-CHAIM) project involves "the development of a regional, fully three-dimensional, electron density model for use at high latitudes" (Themens et al. 2017, 2019).
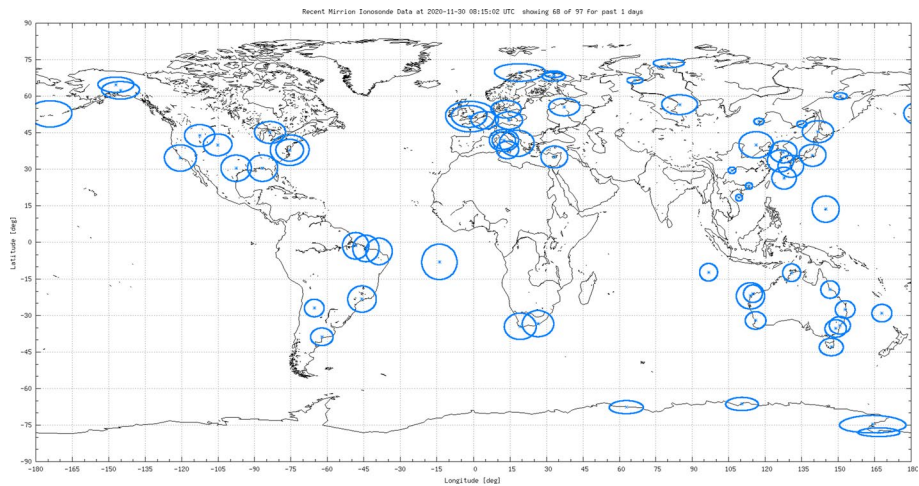
Fig. 3 Map of ionosonde stations currently uploading data to the NOAA Master Ionosonde Data Set (MIDS). Image courtesy of https://www.ngdc.noaa.gov/stp/IONO/rt-iono/

2.4 VLF Instrumentation for Radio Wave Propagation Physics

Very Low Frequency (VLF) is the ITU designation for radio frequencies (RF) in the range of 3–30 kHz. For most locations on Earth, the dominant sources of VLF waves are generated by lightning discharges, except at narrow frequency bands where manmade VLF transmitters dominate. At mid- and high- latitudes VLF waves naturally generated in space can be received on the ground. Examples of such waves are whistlers (generated by lightning), plasmaspheric hiss, and chorus. The occurrence and properties of these waves tell us about the nature of the space around the Earth and can be continuously monitored from high-latitude polar sites at a comparatively low cost. All the waves, along with ULF-band and EMIC (Electromagnetic Ion Cyclotron) waves, are thought to be important drivers of the loss of energetic electrons from the radiation belts. Whistler-mode chorus is increasingly accepted to be a highly important driver of acceleration processes in the radiation belts, energising electrons with tens of keV energy to hundreds or thousands of keV.

VLF measurements in Finland started in the 1970s. Subsequently, different types of VLF receivers were used to study the wave propagation physics in the polar ionosphere (Manninen et al. 2016; Titova et al. 2007; Turunen et al. 1980). Those receivers were situated at different locations in Northern Finland and always far away (> 9 km) from power transmission lines and human settlements. The antennas used with these receivers are orthogonal magnetic loop antennas with an effective enclosed area that has increased from 58 to 2300 m^2 over several years. In 2005 the measurements started to be recorded digitally. Many new kinds of VLF phenomena, such as hiss clouds and structured hiss bands (Macotela et al. 2019; Manninen et al. 2016), justified the design of a new type of VLF receiver that started operation in 2006 at a fixed location in northern Finland at Kannuslehto (67.74°N, 26.27°E; $L = 5.45$). With this receiver, VLF emissions are recorded during different campaigns in the frequency range of 0.2–39 kHz by using two mutually orthogonal magnetic loop antennas oriented in the geographic north–south and east–west directions. Each loop is 10×10 m in size with 10 turns, which yields an effective area of 1000 m^2. The noise level of the receiver is 10–14 nT^2/Hz, and the frequency response is almost

flat in a frequency range of 2.5 to 39 kHz. Furthermore, its sensitivity is usually very high, and hence it can detect signals below the natural noise level. During the campaigns, the recordings are built continuously and can be accessed at no cost on the website http://www.sgo.fi/pub_vlf in the form of 1-min, 1-h, and 24-h total power spectrograms.

Many naturally occurring VLF waves at frequencies above 4–6 kHz could not be studied using ground-based data because strong radio atmospherics (sferics) hide all such waves. To study these VLF waves, researchers have applied special digital tools which filter out strong impulsive sferics (Manninen et al. 2016). Sferics are a particular type of VLF emission that are caused by lightning discharges (Volland 1995) and propagate thousands of km in the Earth-ionosphere waveguide. The removal of sferics by digital filters uncovered completely new types of high-frequency daytime VLF emissions with various unusual spectral structures that have never been seen before.

In some parts of Antarctica, ground-based observations of whistlers can be used to provide continuous monitoring of the plasmasphere (the cold plasma environment is a vital component in the description of the processes in space that couple waves and particles). Because the lightning activity is extremely low in the Antarctic, this region is also very well suited to remote sensing of lightning activity—the lower background noise levels and longer propagation paths provide high accuracy timing observations of radio pulses generated by lightning ('sferics') which can be used in lightning location systems (e.g. World Wide Lighting Location Network, WWLLN; Rodger et al. 2006). Koronczay et al. (2019) estimated the prime source regions of whistlers observed by the AWDAnet network of VLF receivers over a 12 year period (2007–2018), utilising instruments across the globe, including four Antarctic stations.

The VLF measurements at Comandante Ferraz Brazilian Antarctic Station started in 1984, and digitally since 2006. In addition to the investigation of the ionospheric forcing from space, the VLF technique has also been used to investigate the ionospheric effects produced by the impact of the planetary and gravity waves generated below the ionosphere (Correia et al. 2011, 2013b, 2020).

Monitoring of manmade VLF waves (generally from military transmitters) allows low-cost continuous remote sensing of the lower ionosphere. Either communication transmitters or lightning provides powerful sources of VLF waves which propagate many thousands of kilometres, trapped between the lower edge of the ionosphere and the conducting ground/sea. Networks of narrow-band VLF monitors have been deployed in polar regions particularly to study highly energetic electrons and protons lost into the polar atmosphere through precipitation. These include solar proton events (rare, wide-spread over high latitude regions, and intense), radiation belt precipitation (common, long-lasting, highly variable), and substorm precipitation (very common, short-term, highly variable). One example of such a network, with sites around the coast of Antarctica, is the Antarctic-Arctic Radiation-belt (Dynamic) Deposition—VLF Atmospheric Research Konsortium (AARDDVARK) (Clilverd et al. 2009).

The AARDDVARK VLF network has been applied to the long-term determination of energetic electron precipitation into the auroral atmosphere (Neal et al. 2015) and for the development of a model of energetic electron precipitation during geomagnetic storms (Van de Kamp et al. 2016). Another application is the identification of solar flares through their effect on the D-region ionosphere. The increased ionisation from X-ray flares changes the electron density in the bottom side ionosphere (dayside). Since the signals monitored by networks such as AARDDVARK are fairly constant in power and frequency it is possible to utilise amplitude (Wenzel et al. 2016) or phase (Lotz and Clilverd 2019) perturbations of these signals to identify and classify flares. These perturbations are superimposed

on diurnal variations in narrowband signal phase and amplitude caused by solar irradiance. The shape of the diurnal variations are seasonal and the function of the transmitter/receiver pairs is utilised. Therefore, long-term studies such as the one from Cresswell-Moorcock et al. (2015) are necessary to model the diurnal changes so that short-term variations such as those caused by flares (and other phenomena such as solar proton events, precipitation, etc.) can be identified accurately.

Array for Broadband Observations of VLF/ELF Emissions (ABOVE) is a ground-based array of VLF radio receivers in Canada (Cully et al. 2014) monitoring electromagnetic waves in a frequency range from 100 Hz to 75 kHz. It has been applied to study the energetic electron injection events (Ghaffari et al. 2020).

2.5 SuperDARN for Ionospheric Observations

SuperDARN (Super Dual Auroral Radar Network) is a global network of 35 HF low-power radars, looking into Earth's upper atmosphere spanning from mid-latitudes and extending into the polar regions. The radars operate continuously and observe the ionosphere directly and, since mainly space plasma processes are field-aligned in nature, phenomena in the magnetosphere can map along magnetic field lines, to be observed in the ionosphere. The network consists of 23 radars in the Northern Hemisphere and 12 radars in the Southern Hemisphere.

At the high latitudes, field lines extend to the very distant magnetosphere and so processes happening many 10's and 100's of Earth radii away can be readily detected by these radars.

The southern and northern hemisphere radars and their fields of view are shown in Fig. 4.

SuperDARN's presence began in the Antarctic with the Halley radar (HAL in Fig. 4(b)), which saw first light in January 1988. Concerning the North Hemisphere, the first radar
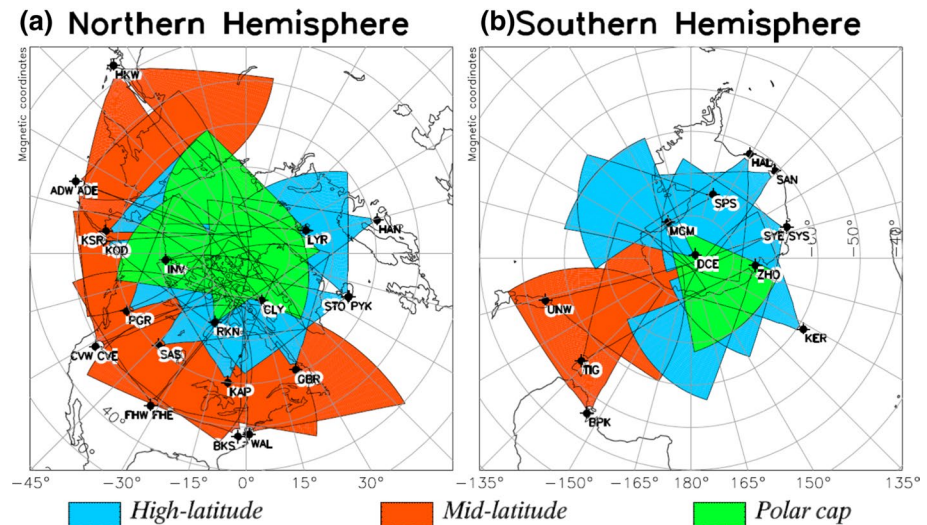

Fig. 4 SuperDARN field of view. The figure is available on http://vt.superdarn.org/tiki-index.php?page=Radar+Overview

was installed in 1983 at Goose Bay, Canada (GBR in Fig. 4(a)), see Greenwald (2021) for the early history of SuperDARN. Following the installation of HAL, 11 more radars have been added in the southern hemisphere. Five radars are not situated on the Antarctic continent but, all except Buckland Park (BPK), have fields of view, or part thereof, which look over the continent. One more radar started operation in January 2019. It is located at Concordia (Dome C-Antarctica) near the Dome C East radar (DCE in Fig. 4(b)) and it is named Dome C North (DCN). DCE and DCN are located very close to the Antarctic geomagnetic pole making them the highest geomagnetic latitude radars. In the northern hemisphere, more than 20 radars have been installed after the GBR installation and, in the last 15 years, the SuperDARN coverage has expanded notably also at mid-latitudes with the addition of a chain of radars across North America and the northern Pacific Ocean into eastern Asia. The last radar installed in the northern hemisphere is the Chinese radar deployed nearby the Jiamusi city, China. The Jiamusi radar (JME) saw the first light in August 2018.

The primary products of a SuperDARN radar are backscattered power, Doppler velocity, and spectral width of the scattering targets. The seminal product of the SuperDARN network is the ionospheric convection map, produced for both hemispheres with a 2-min cadence. Due to the high conductivity of space plasmas, field lines are frozen to the plasma, resulting in a convection electric field in the rest frame of the magnetosphere, setting up the **ExB** convection. This convection is observed in the Doppler velocity measurements of the radars.

2.6 High-Power Large Aperture Radars and Ionospheric Incoherent Scatter

High-power large aperture (HPLA) radars are powerful instruments for studying space-Earth interaction within the fields of aeronomy, meteors, and space debris, among others. Among the most important uses of HPLA radars is in studies of ionospheric incoherent scatter. The theory of ionospheric scattering of VHF/UHF radiowaves was originally based on the concept of Thomson scattering, which is re-radiation by free electrons of incident electromagnetic wave energy. The Thomson cross-section per electron is extremely small, $\sigma_R = 4\pi \left(\frac{q_e^2}{4\pi\epsilon_0 m_e c^2} \right)^2 = 10^{-28} \, \text{m}^{-2}$. This is the reason for using high power and large collecting antennas, as considered by Gordon (1958), leading to the design of the well-known very large radar in Arecibo, Puerto Rico.

However, this first understanding soon turned out to be incomplete. In the actual ionospheric plasma, scattering arises from electron density modulations by thermally excited wave motions of the ions, resembling the Bragg-scattering in a crystal. The theory of incoherent scatter spectra was developed by Farley et al. (1961), Dougherty and Farley (1961) and many others. The most prominent feature of the theoretical spectrum is a double-peaked central line caused by ion-acoustic waves, containing information about the temperatures of the ions and electrons as well as the line-of-sight Doppler velocity. Scatter lines shifted by the electron plasma frequency and gyro frequency can also sometimes be detected. Electron density is measured either by calibrating the total power received in the ion line or from the plasma frequency.

Although larger than originally predicted by the simple Thomson theory, the received power as given by the radar equation (which takes into account transmitter power, antenna gain, range, and scatter cross-section) is on the order of 10^{-18} times the transmitter power. Typical HPLA radars transmit at a peak pulse power on the order of 1 MW and thus receive a signal of about 1 pW. This makes atmospheric and cosmic background noise an important

consideration. The operation frequency has to be selected as a trade-off between scatter strength and background noise. For ionospheric incoherent scatter, HPLA radars usually operate at frequencies in the VHF and UHF bands from 200 MHz to 1 GHz, whereas middle atmospheric HPLA radars use a frequency around 50 MHz or lower.

The process of how the radar works can be explained through a so-called range/time diagram. The high-power radio wave is transmitted, going virtually un-attenuated through the ionosphere. At any height, the electrons scatter the signal isotropically. As the transmission is often modulated in several respects, the received signal must go through rather complicated decoding processes. As an example, to get high range resolution it is necessary to transmit a relatively short pulse but to get high spectral resolution the pulse must be rather long. These conflicting requirements vary for different ionospheric layers, so complicated modulation principles are often used to satisfy these conditions. After forming the spectral components for all range intervals, the signal goes into a fitting procedure comprising an iterative comparison with theoretical spectra. Since an essentially exact incoherent scatter theory exists, the results give very detailed information on the ionosphere via the parameters derived. The four main parameters derived are the electron density, the electron and ion temperatures, and the ion bulk flow velocity. However, depending on the analysis procedure and altitude region, one can also fit other parameters such as collision frequency, ion composition, negative and cluster ions, and so on. The NRLMSISE-00 (Picone et al. 2002) and IRI 2016 (Bilitza et al. 2017) empirical atmospheric models are normally used for this purpose. One can also set constraints on parameters or vary the integration in time and/or space to increase the accuracy. Combining the derived parameters with other data or models gives a wealth of further physical quantities describing the ionosphere and neutral atmospheres, such as neutral wind, electric fields, and conductivities in various directions.

Most HPLA radars are in the northern hemisphere with the notable exception of the Jicamarca radar in Peru, which is at the magnetic equator.

2.7 EISCAT and AMISR to Detect Disturbances in the Ionosphere

EISCAT, originally the European Incoherent Scatter Scientific Association, was established in the early 1970's to develop a large radar for the northern auroral oval, a location where direct magnetosphere-atmosphere interaction takes place. EISCAT started operations in 1981 with a tristatic UHF (930 MHz band) radar (Folkestadet al. 1983) in northern Fennoscandia; transmitter at Tromsø (69 N, 19 E), remote receivers in Kiruna (67° N, 20° E), and Sodankylä (67° N, 26° E). A VHF radar (224 MHz) with a 120×40 m cylindrical antenna was added to the Tromsø site in 1985. Due to interference from mobile communication in the 930 MHz band, the two remote sites have been converted to the VHF radar frequency, that is, at present, the VHF radar is a tristatic system. The tristatic capability makes EISCAT unique in the world among incoherent scatter radars, since full ion vector velocities can be measured, and hence the vector electric field at the point of intersection be calculated.

The next major step forward for EISCAT was taken in 1996 when the EISCAT Svalbard radar (ESR, Wannberg et al. 1997) became operational. This system, with two parabolic antennas, is located at 78° N geographic latitude in the cusp and dayside auroral oval region, thus another region of major interest for studies of direct and indirect space-Earth interactions. The ESR receiver was designed to use state-of-the-art digital signal processing and software-based decoding.

The Tromsø transmitter site is co-located with the so-called Heating facility, originally constructed by the Max Planck Institute in 1979 (Stubbe et al. 1982) and later transferred to EISCAT. This is a powerful transmitter (about 1 MW of CW power) operating at 4–8 MHz and capable of Effective Radiated Power (ERP) up to 1 GW at the highest frequency. The Heating facility is intended for active ionospheric modification experiments, where the incoherent scatter radars, optical instruments, and VLF receivers are used as detectors. Receiver capabilities were added in 2010, making the heating facility a flexible HF radar.

EISCAT data are available at https://eiscat.se/ according to access rules in the EISCAT statutes. Graphical overview data are free to download but must not be published without appropriate co-authorship.

The future of EISCAT is the EISCAT_3D radar, which is now under construction and will replace the EISCAT mainland radars (McCrea et al. 2015). EISCAT_3D will provide observations of both the scalar ionospheric parameters and velocity vectors from a volume, hence the 3D in its name. In contrast with the present radars, which run on a campaign basis, EISCAT_3D will allow a continuous low power overview mode. Such three-dimensional ionospheric studies will further our understanding of the coupling of atmospheric layers and the magnetosphere, and also be of major importance for improving satellite navigation at auroral latitudes thanks to the gained knowledge on the regional ionospheric structuring which adversely affect GNSS signal propagation. EISCAT_3D will also be a flexible HPLA radar for meteor and space debris studies.

In the initial stage, EISCAT_3D will consist of three stations with up to 10 000 antennas each (Fig. 5 Artistic rendering of the future EISCAT_3D transmitter site in Skibotn, Norway.). One station (Skibotn, Norway) will have transmitters and receivers, and there will be two receive-only, multiple beam sites at Karesuvanto in Finland and Kaiseniemi in Sweden. The system hardware will be installed during 2022 and first data will be available in 2023.
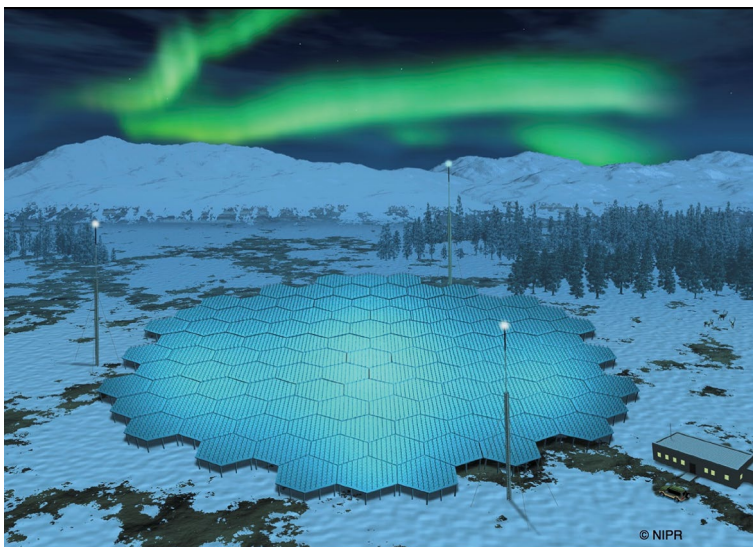

Fig. 5 Artistic rendering of the future EISCAT_3D transmitter site in Skibotn, Norway. Credit: National Institute of Polar Research (NIPR)

The advanced modular incoherent scatter radar (AMISR, Valentic et al. 2013) facility in the American sector has been used to conduct studies of the upper atmosphere and to observe space weather events since 2007. Unlike traditional ISRs, AMISR consists of 1000 s antenna element units to transmit and receive and thus can image the ionosphere at different directions nearly simultaneously, which significantly increases the temporal resolution of the measurements. This feature is particularly useful for monitoring the rapidly evolving high-latitude plasma dynamics. There are currently two US-supported AMISR radars, i.e. Poker Flat Incoherent Scatter Radar (PFISR) and Resolute Bay Incoherent Scatter Radar-North (RISR-N) (shown in Fig. 6), and one Canadian supported RISR-C. PFISR is located at ~65° geomagnetic latitude and looking poleward, which covers subauroral and auroral zones, while the two RISR radars are located at ~82° geomagnetic latitude and deep in the polar cap. The AMISR data can be accessed through the SRI AMISR website (https://amisr.com/amisr) and the University of Calgary portal (https://data.phys.ucalgary.ca/sort_by_project/RISR-C/).

2.8 Optical Imagers for Auroral Studies

Optical imagers are commonly used together with the radio observations of the ionosphere in the polar regions to study the effects of the auroral activity. Often they are equipped with narrow filters to record auroral emissions at particular wavelengths. The most commonly used filters are for 557.7, 427.8, and 630.0 nm. Monochromatic wide band (greyscale) imagers and standard colour cameras are also used. Networks of auroral imagers are installed in the Arctic, for example in Svalbard, in Fennoscandia, or in Canada, while in Antarctica the number of all sky auroral cameras is still limited. An example of an imager network is the Auroral Large Imaging System (ALIS). ALIS is a set-up of six CCD (Charged Coupled Device) cameras located in Northern Sweden with mutual distances around 50 km and an average field-of-view of 90° (Brändström, 2003). The system has been originally designed for auroral tomography, but the sensitive imagers with the collection of narrowband filters for > 10 wisely selected wavelengths have appeared to be useful also in studies on radio-induced aurora (Gustavsson, 2000), polar stratospheric clouds, and meteors. While ALIS has been a system for campaign measurements only, its successor ALIS_4D runs continuously (http://www.alis4d.irf.se/). In ALIS_4D, CCD technology is replaced with EMCCD (Electron Multiplying CCD) imagers whose performance allows higher sensitivity and sampling rate when compared to the old system. Both ALIS and

Fig. 6 Poker Flat Incoherent Scatter Radar (left) and Resolute Bay Incoherent Scatter Radar—North (right). Photo credit: Craig Heinselman

ALIS_4D station locations and fields-of-view have been planned so that the optical system supports in optimal way measurements by the EISCAT and EISCAT_3D incoherent scatter radars.

The MIRACLE (Magnetometers—Ionospheric Radars—All-sky Cameras Large Experiment) is a network of ground-based instruments, which was originally established to support the ESA Cluster mission of four satellites. The network has five cameras in Northern Finland and Sweden, as well as two cameras on Svalbard. Two of the Fennoscandia camera systems are EMCCD imagers equipped with narrow-band filters for the dominating visual wavelengths and their nearby wavelengths for background subtraction (Sangalli et al. 2011). The oldest camera of the network has an intensified CCD. The two remaining cameras are colour cameras under renovation to be replaced with imagers belonging to Boreal Auroral Camera Concept (Sigernes et al. 2017). MIRACLE cameras have wide fields-of-view and they have traditionally been used in magnetosphere-ionosphere coupling studies as all-sky images of auroras provide nicely a wider context for localised satellite observations (Juusola et al. 2016). As the camera network has been collecting data continuously during the dark season over several years, its data has enabled statistical studies on the appearance of different auroral structures (Partamies et al. 2014). MIRACLE cameras have been used extensively to support also auroral tourism (Kauristie et al. 2016).

The Northern Solar Terrestrial Array (NORSTAR) (Donovan et al. 2003) is an optical and radio facility designed to remotely sense auroral precipitation on a continental scale. NORSTAR consists of CCD-based All-Sky Imagers (ASIs), Meridian Scanning Photometers (MSPs), and riometers. It includes the ground-based ASIs to support the NASA Time History of Events and Macroscale Interactions during Substorms (THEMIS) project (Mende et al. 2008).

2.9 Magnetometers for Geomagnetic Parameters

The observation of the Earth's magnetic field variation from polar areas is carried out through a variety of magnetometers installed in Antarctica and the Arctic including proton magnetometers, which give the scalar absolute values of the total field, fluxgate magnetometers which give 3-axis vector data, and induction coil magnetometers devoted to recording the so-called geomagnetic micropulsations from the electric field induced in a coil (e.g. Francia et al. 2009; Pilipenko and Engebretson 2002; Regi et al. 2018; Villante et al. 2000).

Some countries have a long and continuing tradition in performing magnetic observations, and in managing observatories, especially in inhabited territories of old continents or in those territories under the influence of the countries who exercised expansionistic politics in the past. INTERMAGNET (the INTERnational Real-time MAGnetic Observatory NETwork), a world-wide consortium of institutes operating ground-based magnetic observatories and setting observatory standards, was developed from a pilot scheme between USGS (United States Geological Survey) and BGS (British Geological Survey) in 1987, and now incorporates data from approximately 150 observatories into a unified database (https://www.intermagnet.org/).

In Europe, many countries have contributed to recording the magnetic field since the middle of the eighteenth century: UK, Germany, and France to cite those most prominent, which can boast long series of data of crucial importance in reconstructing the field of the past. It should not be a surprise that such countries were spontaneously interested in supporting magnetic recordings from remote and isolated lands (including those in open oceans) under their control. In the USA, USGS established its first magnetic observatory in

1900 at Cheltenham, MD (it moved to Fredericksburg, VA, in 1956) and now includes 11 sites in the continental USA and 3 on US islands.

In addition to magnetic observatories, many other arrays of fluxgate magnetometers have been deployed in support of studies of the upper atmosphere, ionosphere, and magnetosphere, many using instruments identical to or similar to those used by magnetic observatories, but because in contrast with magnetic observatories, they are not supported by repeated absolute calibrations and often not supported by trained local personnel, they are designated as variometer arrays. These arrays were often developed for specific research studies, but continue to operate and now serve a variety of research purposes. For example, the Geophysical Institute Magnetometer Array (GIMA) of fluxgate magnetometers was installed in 1995 in Alaska and was initially funded by NASA as part of a Poker Flat Research Range upgrade. GIMA is primarily used to observe the magnitude and location of the auroral electrojet in support of sounding rocket missions and global current experiments. Similarly, the Magnetometer Array for Cusp and Cleft Studies (MACCS), located in former Northwest Territories (now Nunavut) in Canada, was originally deployed in 1992 as part of the US Geophysical Environment Modelling (GEM) Boundary Layer Campaign to study the interactions of the solar wind with the outer magnetosphere and its high latitude footpoint on the ground.

A different approach was applied in the case of the polar sectors of our planet. Here, the geographic difference between the Arctic and Antarctica, with islands embracing an iced open ocean in the first case, and oceans surrounding a continent in the second case is reflected in the nations who are operating there: Canada, Sweden, Russia, Finland, Norway and Denmark are the nations who are in front of the Arctic. Differently, the Antarctic continent was relatively late to be explored because of its remoteness and very harsh environmental context, and besides the interest of those southern hemisphere nations overlooking the white continent (Chile, Argentina, South Africa, New Zealand, and Australia), also different nations are now operating there: USA, Italy, Spain, Ukraine, Japan, Germany, Russia and China. In addition to the large number of INTERMAGNET observatories in Arctic regions, many variometer arrays provide magnetic field data in both the Arctic and Antarctic regions. Many of these contribute data to centralised data servers such as SUPERMAG (https://supermag.jhuapl.edu/), CDAWEB (https://cdaweb.gsfc.nasa.gov/), and THEMIS (http://themis.igpp.ucla.edu/overview_data.shtml). Figure 7 shows Ultra Large Terrestrial International Magnetometer Array (ULTIMA) as of December 2014.

Fig. 7 Ultra Large Terrestrial International Magnetometer Array (ULTIMA) (Credit: Dr. Peter Chi, UCLA)
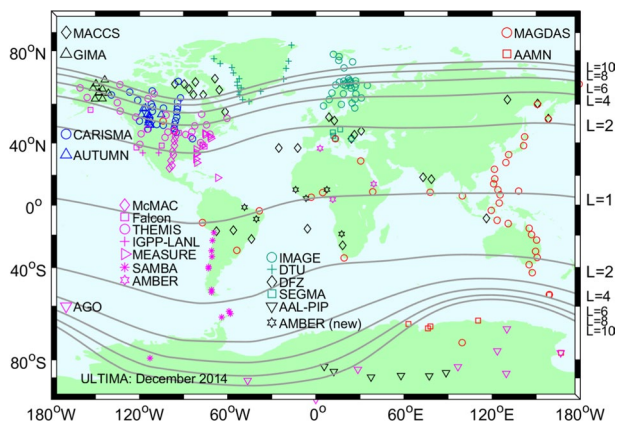
Finally, the most remote ground geomagnetic observatories, at Concordia station (Italy and France) and Vostok station (Russia), located in the inner part of the Antarctic plateau at a distance of more than 1000 km from the coast, are worthy to be mentioned for acknowledging the efforts, sustained by people and organisations involved in collecting and distributing geomagnetic data of high quality. They guarantee the recording, storage, and distribution of data from points located in very remote areas of the Earth: all year round, absolute measurements are manually executed once a week, and time-series recordings are available for the interested communities in quasi-real-time. Data from those remote points, besides being useful for various applications, are extremely useful for contributing to generate reliable models of the Earth's magnetic field, like the IGRF model (International Geomagnetic Reference Field), updated and released every 5 years (Di Mauro et al. 2014).

Table 1 summarises the principal variometer arrays located in the Arctic and Antarctica.

The Magnetic Induction Coil Array (http://mirl.sr.unh.edu/ulf_status.html) is an outgrowth of induction coil magnetometer observations in conjugate hemispheres beginning in 1979 at Siple Station, Antarctica, and Roberval, Quebec. Systems were installed at the South Pole in 1982 and McMurdo, Antarctica in 1985; data from these locations have been recorded almost continuously since then. Systems at northern cusp latitudes, roughly magnetically conjugate to the South Pole, were installed at Sondrestromfjord, Greenland in 1984 (discontinued in 2018) and at Iqaluit, Canada in 1993. Systems were installed at the British Antarctic Survey's multi-instrument Automated Geophysical Observatory (AGO) sites A80, A81, and A84 in 1996 and operated until 2004, and installed at Halley and Rothera in 2005 and 2015, respectively. A set of 4 closely-spaced induction coils was installed at Svalbard (Arctic Norway), 3 in 2006 and 1 in 2008. A system at the northern magnetic footpoint of GOES 13 was installed at Sanikiluaq, Canada in 2015. More recent activity has involved colleagues from South Korea, who have replicated the sensors, resulting in the installation of 3 new systems at Antarctic sites: Neumayer, Jang Bogo, and King Sejong. Induction magnetometers were also included in the AAL-PIP array in Antarctica beginning in 2008. Current activity includes the fabrication of two new systems to be installed by Chinese colleagues. Induction coil studies have for many years been augmented by the multi-instrument capabilities available at Siple (abandoned in ~1988), BAS and US AGOs, South Pole, McMurdo, and Svalbard, as well as induction coils and other instruments at the Arctic and Antarctic sites operated by other nations, and particle and field instruments on numerous spacecrafts.

Magnetometers at these high latitudes have provided data for many studies of the ground signatures of interactions of the solar wind with the outer magnetosphere and its high latitude footpoint on the ground, including sudden impulses, travelling convection vortices, and possible ground signatures of dayside reconnection. They also provide supporting information for studies of magnetospheric and ionospheric processes (flows and ULF waves) in the high-altitude cusp, the magnetopause boundary layers, the outermost closed field line regions of the magnetosphere, and the open flux regions of the polar cap, plasma mantle, and magnetotail (e.g. Neudegg et al. 2002; Rodger and Smith 1989).

An amazing example of how magnetometers' data can be used for geospace activity indication is given by the Polar Cap (PC) index, introduced in 1985 by Troshichev and Andrezen (1985). The PC index is calculated separately for Northern and Southern hemispheres (PCN and PCS, correspondingly) by magnetic data from the near-pole stations Thule (Greenland) and Vostok (Antarctica) by the method put forward by Troshichev et al. (2006). In 2013 the International Association of Geomagnetism and Aeronomy (IAGA) approved the PC index as an indicator of energy that enters into the magnetosphere during solar wind-magnetosphere coupling (http://www.iaga-aiga.org/index.php?id=res3-2013).

Table 1 Variometer arrays

Location	Arrays name	Website	Useful references
Arctic	IMAGE—International Monitor for Auroral Geomagnetic Effects	http://space.fmi.fi/image	Tanskanen (2009)
	Greenland Magnetometer arrays	https://www.space.dtu.dk/MagneticGroundStations	
	CANMOS—Canadian Magnetic Observatory System	http://geomag.nrcan.gc.ca/data-donnee/sd-en.php	Nikitina et al. (2016)
	CARISMA—Canadian Array for for Realtime Investigations of Magnetic Activity	http://www.carisma.ca/	Mann et al. (2008)
	AUTUMN—Athabasca University THEMIS UCLA Magnetometer Network	http://autumn.athabascau.ca/TBS_autumnquery.php http://autumn.athabascau.ca/TBS_autumnxquery2.php	Connors et al. (2016)
	AUTUMNX—Arctic Quebec, Canada		
	GIMA—Geophysical Institute Magnetometer Array	www.gi.alaska.edu/monitors/magnetometer	
	MACCS Magnetometer Array for Cusp and Cleft Studies	http://space.augsburg.edu/maccs/index.html	Engebretson et al. (1995)
Antarctica	AAL-PIP Autonomous Adaptive Low-Power Instrument Platform	http://mist.nianet.org/	Clauer et al. (2014)
	British Antarctic Survey (BAS) LPM	https://data.bas.ac.uk/full-record.php?id=GB/NERC/BAS/AEDC/00263	Kadokura et al. (2008)
	SAMBA—South American Meridional B-Field Array	http://magnetometers.bc.edu/index.php/samba2	
	South Pole Station, McMurdo, and US AGOs—Antarctica	South Pole Station, McMurdo, and US AGOs – Antarctica	Engebretson et al. (1997) Lanzerotti et al. (1990)

This concept is based on the following experimental evidences (Troshichev et al. 2014, 2018; Troshichev and Sormakov 2015, 2018, 2019a, 2019b): (1) the PC index responds to changes of the solar wind electric field (EKL), the EKL increase being followed by the PC growth with the delay time $\Delta T \sim 12$–20 min; (2) influence of EKL on the polar cap magnetic activity proceeds by means of field-aligned currents (R1 FAC system) flowing within the closed magnetosphere; (3) the PC index growth always precedes the magnetic substorms development, the substorm growth phase duration and substorm intensity being specified by the PC growth rate; (4) the substorms start when the PC index reaches the threshold level (1.5 ± 0.5 mV/m) and last as long as PC continues to be in excess of this level, the substorm intensity (the AL index) being linearly related to the PC value; (5) the magnetic storms start when the PC index steadily (on a time lapse more than 1 h) exceeds the threshold of > 1.5–2 mV/m, the storm intensity (Dst_{MIN}) being linearly related to the values PC_{MAX} preceding the storm maximum; (6) the magnetic activity (PC and AL indices) correlates (increases or decreases) with the solar wind pressure (leaps or drops) only if the solar wind pressure impulses are accompanied by the corresponding changes of EKL. In addition, the PC index ensures the possibility to verify whether or not the solar wind, fixed far upstream of the magnetosphere (in the Lagrange point L1), encountered the magnetosphere in reality. In such a way the utility of the solar wind data, presented at the OMNI website, for examination of the solar wind-magnetosphere coupling can be validated.

Thus, the PC index can be successfully used to monitor the state of the magnetosphere (space weather monitoring) and readiness of the magnetosphere to produce substorms or storms (space weather nowcasting). A great advantage of the PC index application over other methods based on the satellite data is a permanent on-line availability of information on the solar wind energy input into the magnetosphere. A special procedure agreed by the Arctic and Antarctic Research Institute (AARI) and Space Institute of the Danish Technical University (DTUSpace) ensures the on-line production of the PCS and PCN indices, which are presented at the websites http://pcindex.org and www.space.dtu.dk/wdc/pcn-index.

High latitude ground magnetometer data are also often combined with data from high altitude spacecraft such as Cluster, Polar, THEMIS, and MMS for studies of ULF waves, and are routinely incorporated into several multi-array regional and global empirical modelling efforts and databases (e.g. the Assimilative Mapping of Ionospheric Electrodynamics, AMIE, and the Spherical Elementary Current Systems, SECS).

The focus of induction coil magnetometer studies has been on wave phenomena in the upper ULF band (Pc3–4, Pc 1–2, Pi 1) that appear as modulations in auroral and VLF emissions as well as in magnetic fields, and has included conjugate studies. Some sites provide the opportunity to study the coupling of solar wind energy to the magnetosphere and ionosphere near the dayside polar cusp/cleft regions, the polar cap, and nightside auroral regions. Others observe EMIC waves (Pc 1–2) in the region of the radiation belts.

2.9.1 Microwave Humidity Sounders

Microwave humidity sounders are intended to determine the atmospheric humidity profile from observations around the 183 GHz water vapour absorption line (Eymard 2002). They have been operationally observing humidity profiles in low and mid-latitudes since the launch of SSM/T2 aboard the DMSP-F11 satellite in 1992. However, in the polar regions, the low water vapour content causes the weighting functions to peak near the surface so that the profile can no longer be determined (Kuo et al. 1994).

However, Miao et al. ([2001](#)) have suggested a procedure to determine Antarctic vertically integrated water vapour column values up to 7 kg/m^2. Later on, the method has been extended up to 15 kg/m^2 by Melsheimer and Heygster ([2008](#)) by including observations around 90 GHz and information about the relation between the emissivities at these frequencies. More systematic usage of the humidity in polar regions from these sensors, which is based on the continuously available humidity sounders since 1999 (Table 2) requires a thorough validation with the retrievals based on surface observations, e.g. from radiosondes and GPS observations. The work of Triana-Gómez et al. ([2020](#)) contributes to this goal with a scheme to screen artefacts in the water vapour retrieval caused by the high ice content in convective clouds. The satellite-based sensors of Table 2 all adhere to a Sun-synchronous orbit so that, provided a careful inter-calibration is made, even the diurnal cycle can be sampled at different times for the whole polar regions. Note that each sensor crosses the polar regions twice and at two different times during one orbit, once with ascending and once with descending flight direction. Until now, the diurnal cycle could only be observed at a few sites with GPS stations, where the measurements were obtained continuously.

3 Long-term Scientific Achievements

This section gives a summary of results achieved through the exploitation of long-term data series (from seasons to several years) acquired by the infrastructures described in the first section.

3.1 Troposphere

Being the most important natural greenhouse gas and responsible for the largest known feedback mechanism for amplifying climate change, the role of water vapour is crucial in a warming climate. The water vapour radiation feedback is recognised as one of the most important contributors for the Arctic amplification (the rate of the Arctic climate change is two times larger than the global one), among other amplification factors (poleward energy transports, snow/ice albedo and cloud-radiation feedbacks, Rinke et al. [2019](#)). However, as atmospheric water vapour is highly variable, both in space and in

Table 2 Humidity sounders in orbit, with platforms, launch year, and approximate Equator crossing times (ECT)

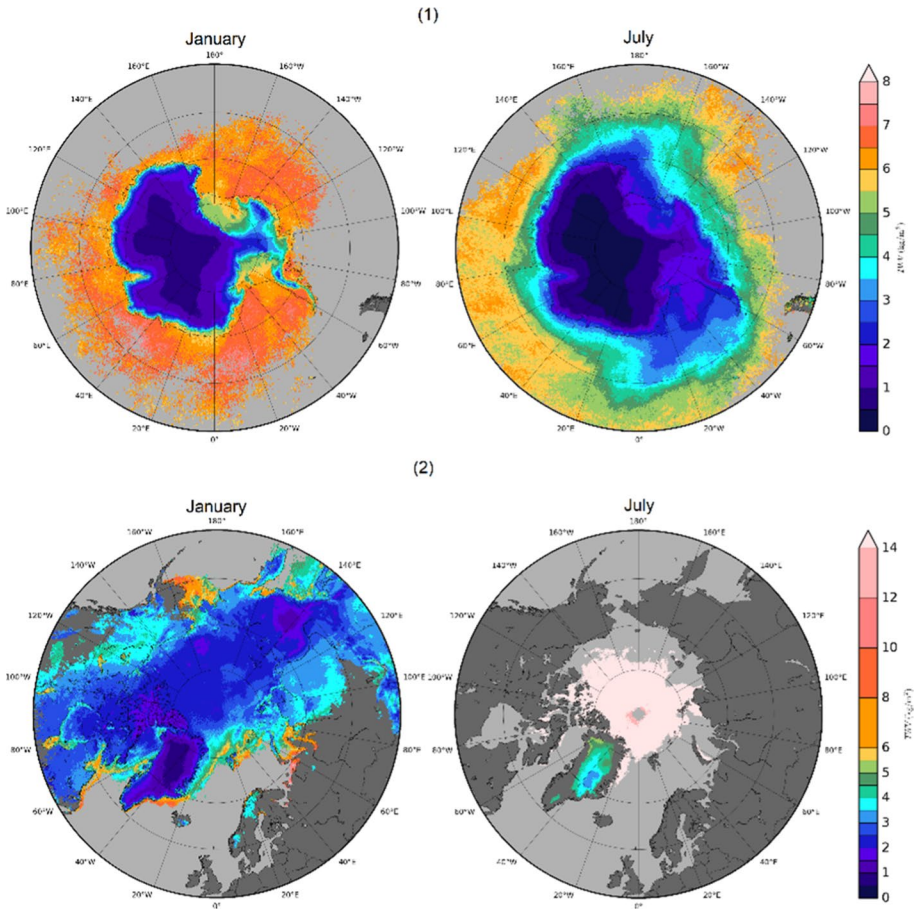| Platform	Sensor	Launch year	ECT (Local Time)
NOAA15	AMSU-B	1999	07:00
NOAA16	AMSU-B	2000	21:00
NOAA17	AMSU-B	2002	07:00
NOAA18	MHS	2005	20:00
NOAA19	MHS	2009	20:00
Metop-A	MHS	2016	09:30
Metop-B	MHS	2012	09:30
Metop-C	MHS	2018	09:30

(1)

(2)

Fig. 8 Monthly mean values of PW for representative months of summer and winter for (top) Antarctic and (bottom) the Arctic, for the year 2007. Retrieval based on L1C NOAA-17 swath data, maps gridded to $0.25° \times 0.25°$ using Gaussian weighting with 12.5 km search radius and 4 neighbours. Data from https:// seaice.uni-bremen.de/water-vapor/ in swath format. For details see Triana-Gómez et al. (2020)

time, measuring it remains a demanding and challenging task. This is in particular true at high latitudes, where the amount of water vapour is minimal (see e.g. Alraddawi et al. 2018) and instrument operation sometimes difficult.

3.1.1 PW Retrieved by Microwave Humidity Sounders and Cross-Validation with GNSS, Radiosondes and ERA-Interim Model

Continuous measurements by GNSS and regular measurements of precipitable water (PW) by radiosondes provide surface-based measurements to complement remote sensing of PW using humidity sensors on low Earth-orbiting satellites, which provide wide coverage, but intermittent observations, over any particular location. One of the key challenges of PW observations over high latitude regions is the low levels of PW in these areas. This paragraph highlights the cross-calibration and synergism achievable by using complementary instruments available in the polar regions.

Different techniques have been used to detect atmospheric water vapour: satellite microwave humidity sounders, GNSS, and radiosondes. The results have been compared against each other and with the European Centre for Medium-Range Weather Forecasts (ECMWF) Era_Interim model (Dee et al. 2011) values for the selected 2006–2007 time period. In Fig. 8, the example of monthly means PW for each hemisphere is mapped in winter and summer for 2007 (Triana-Gómez et al. 2020). They have been determined from the daily data available at https://seaice.uni-bremen.de/water-vapor/ in swath format. For details see Triana-Gómez et al. (2020).

A climatological study of PW in the polar regions by Negusini et al. (2021), was based on the 20-year time series (1998–2017) of GPS observations, acquired, among the others, at five coastal Antarctic and Arctic stations as mapped in Fig. 9. The time series have been processed, adopting homogeneous and consistent reprocessing strategies. From the GPS data, 1-h average values of local integrated PW have been computed each six hours (00:00, 06:00, 12:00, and 18:00 UTC). The GPS observations were sampled every 30 s, with a cut-off elevation angle of 10°, corresponding to a 34 km footprint diameter at 3 km height. The GPS results were validated using the radiosounding (RS) measurements collected over the same periods and locations; RS data were analysed minimising and removing the known error sources and the instrumental biases, correcting raw pressure, temperature, and relative humidity measurements. The humidity sounder data processed have been collected by the AMSU-B sensor onboard the NOAA-17 satellite. For comparison, PW values were selected that satisfy the following two conditions: (1) satellite data within ± 1 h from the integrated GPS measurements (00:00, 06:00, 12:00, and 18:00 UTC) and (2) satellite path within a 50 km radius around the GPS station. The ERA-Interim reanalysis dataset by ECMWF covers the period from 1979 to 31 August 2019 and, unlike in-situ observations, reanalysis data yields spatially complete and coherent records of meteorological variables including PW. The horizontal resolution is $1.5° \times 1.5°$ each six hours (00:00, 06:00, 12:00, and 18:00 UTC). The closest grid points to the 10 coastal GPS stations were considered.

The GPS, ERA-Interim, AMSU-B, and RS time series in Fig. 10 (Arctic) and Fig. 11 (Antarctic) present generally consistent patterns and reasonable seasonal evolution, with dry winters and wet summers. There is no consistent dry or wet bias of one technique
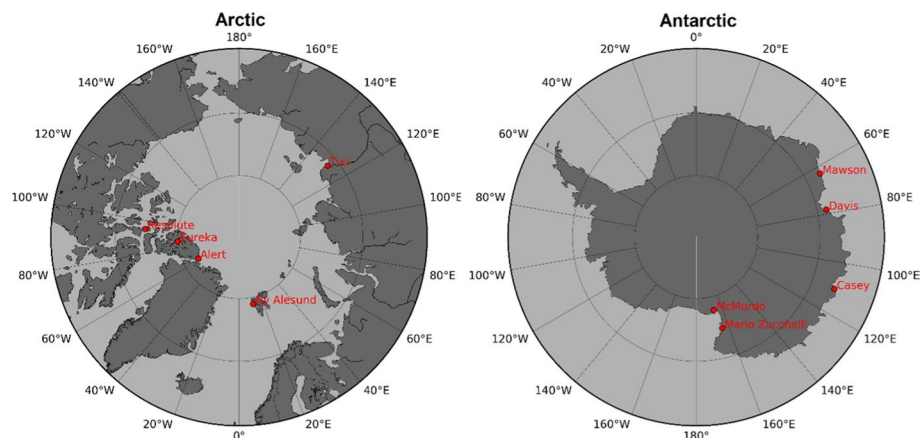

Fig. 9 Location of the GPS and co-located radiosonde stations in the Arctic (left) and Antarctic (right)
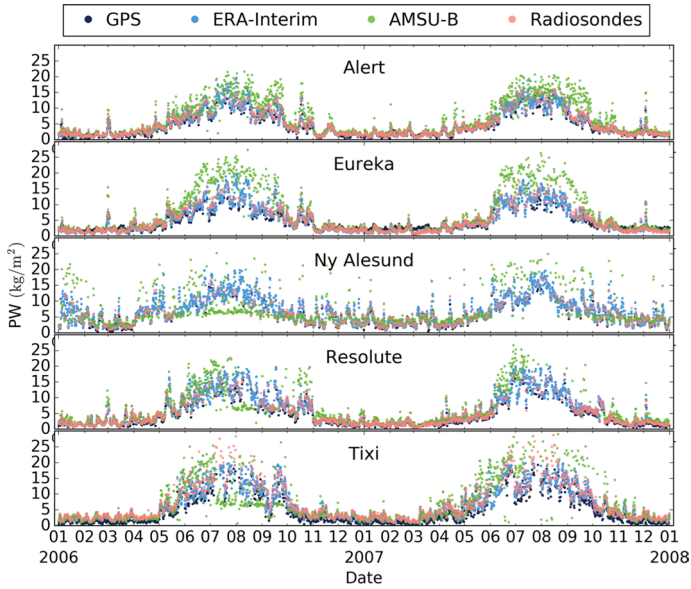
Fig. 10 Time series of PW at five Arctic stations. Based on data from https://seaice.uni-bremen.de/water-vapor/ in swath format. For details see Triana-Gómez et al. (2020)
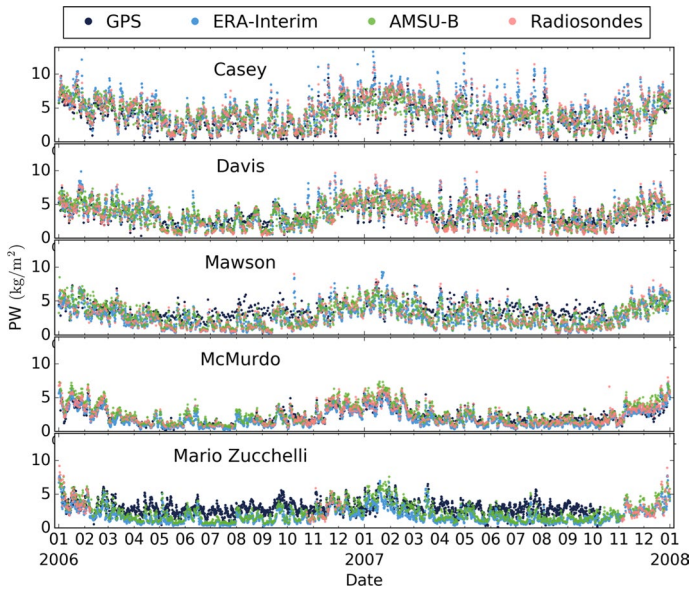
Fig. 11 Time series of PW at five Antarctic stations. Based on data from https://seaice.uni-bremen.de/water-vapor/ in swath format. For details see Triana-Gómez et al. (2020)

with respect to the others. In the Arctic (Fig. 10) the agreement between the datasets is worse during the summer months, mainly due to "spikier" data, i.e. maxima in PW values. This is consistent with the results for the three Antarctic stations (Fig. 11) situated at lower latitudes (Casey, Davis, Mawson). Moreover, ERA-Interim data in McMurdo and Mario Zucchelli generally indicate lower PW than all other datasets. The seasonal cycle is more pronounced in the Arctic than in Antarctica.

Scatter plots and regressions comparing the four datasets have been considered for all the stations. Figure 12 shows the resulting fit parameters for the Arctic with summer and winter results separated. The highest correlations (0.94 and 0.96) are reached between radiosondes and GPS, supporting the reliability of both methods. For evaluating the AMSU-B based retrievals, the GPS-based values were selected as they offer the additional advantage of being available continuously, minimising the error caused by the time lag between the observations.

Among the Antarctic cases, the AMSU-B retrieval shows the best agreement in terms of high correlation coefficient R^2 and low Root-Mean-Square Deviation (RMSD) at McMurdo. This corresponds to the low PW variability at this station, as seen in the time series in Fig. 11. The influence of terrain elevation variation within the AMUS-B
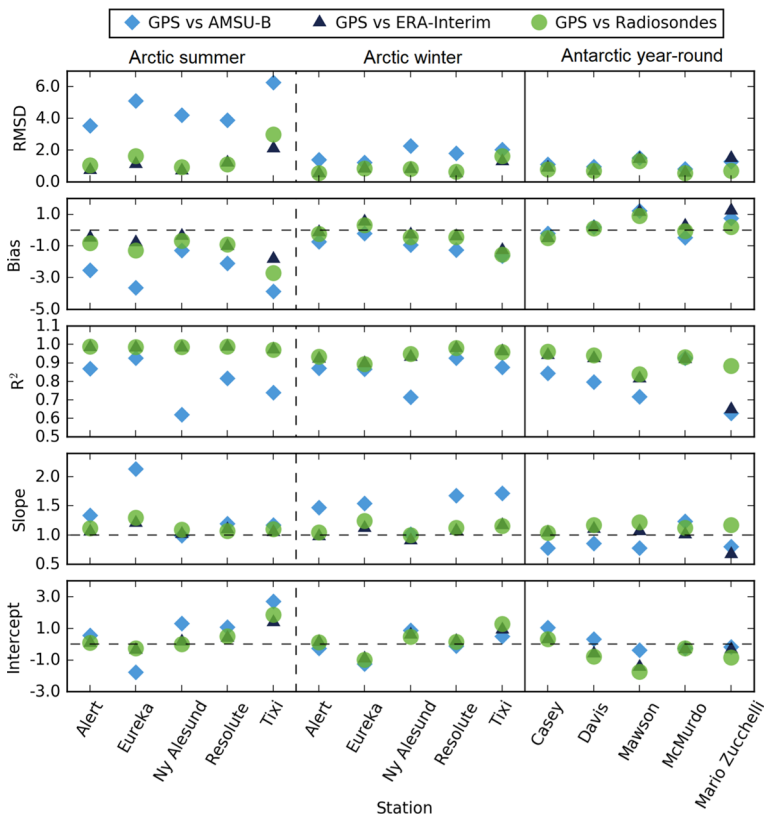
Fig. 12 Values of fit parameters intercept and slope of the regression line, correlation coefficient R^2, bias, and RMSD for the time series intercomparison at the ten GPS stations. RMSD (Root-Mean-Square Deviation), bias and intercept are in kg/m^2, slope and R^2 are absolute numbers

Table 3 List of IGS stations used in this paper with their geographic latitude and longitude, and their altitude

Name	City	Country	Lat (°)	Lon (°)	Alt (m)
CAS1	Casey	Antarctica	−66.28	110.52	39.41
DAV1	Davis	Antarctica	−68.58	77.97	27.14
FAIR	Fairbanks	USA	64.98	−147.50	307.76
KIRU	Kiruna	Sweden	67.86	20.97	362.08
MAW1	Mawson	Antarctica	−67.61	62.87	30.48
MCM4	Ross Island	Antarctica	−77.84	166.67	150.46
METS	Kirkkonummi	Finland	60.22	24.40	75.76
REYK	Reykjavik	Iceland	64.14	−21.96	26.56
SVTL	Svetloe	Russia	60.53	29.78	60.98
SYOG	East Ongle Island	Antarctica	−69.01	39.58	27.76
WHIT	Whitehorse	Canada	60.75	−135.22	1419.57
YELL	Yellowknife	Canada	62.48	−114.48	207.61

footprint around the GPS station has been investigated with the global relief model ETOPO1 (Amante and Eaktins 2009), leading to the conclusion that the terrain elevation variations play a minor role in the retrieval for this case study. Taking the retrievals from all five Antarctic stations together, it has been found that, on average for the Antarctic, $PW_{AMSU} < PW_{GPS} < PW_{ECMWF}$, with all three average bias values below 0.6 kg/m².

The higher RMSD values in the Arctic summer correlate with higher disagreement seen at PW values over 7 kg/m² for all methods. In the case of AMSU-B, such disagreement at higher PW values can be explained by a change in the PW retrieval algorithm to another mode which in addition uses the 89 GHz observations and needs a relation between the 150 GHz and 89 GHz emissivities which may not be as tight as the retrieval requires. However, this disagreement can also be seen between the other two methods and GPS-based retrieval so that generally retrieval of higher PW values seems only to be possible with higher uncertainty, for all investigated methods.

For all ten stations and seasons, the bias is smaller than the RMSD. Hence, the variability of data is larger than the systematic difference between the compared datasets. This, coupled with the fact that the RMSD is of the same order as found for previous PW studies at high latitudes (Buehler et al. 2012; Palm et al. 2010), corroborates the confidence in the AMSU-B based PW retrieval.

The procedure introduced by Triana-Gomez et al. (2020) to retrieve PW from microwave humidity sounders in polar regions offers daily Arctic-wide and Antarctic-wide maps of PW. Such information has not been available before and is needed to improve polar weather prediction and climate studies. For an operational use of the data, a more extended validation is required for which the necessary GPS and radiosondes data are available.

As global warming is particularly pronounced in the Arctic (Arctic Amplification), a stronger increase in PW is expected, which should be observed Arctic-wide. As the Central Arctic is covered by the Arctic Ocean, the method will have to be combined with PW retrievals over the open ocean based on satellite-based microwave imagers such as AMSR-E and AMSR2. This merged dataset is in progress. Despite the present limitations of the method, it performs adequately when compared to GPS. After a careful inter-calibration of retrievals from different humidity sounders, climatological time series can be analysed for trends and change patterns.

Because the Sun-synchronous orbits of the humidity sounders have different equator crossing times and the swaths of consecutive orbits overlap at high latitudes, the diurnal cycle, although expected small, can also be investigated on a hemisphere-wide scale.

3.1.2 Long-term Variability of the GPS-Derived Precipitable Water Vapour Retrievals at High Latitudes

Three different datasets are used to investigate and interpret the long-term variability of PW amounts at high latitudes ($> 60°$). Firstly, the PW time series derived from the International GNSS Service (IGS) repro1 tropospheric product (Zenith Total Delays, ZTDs, Byun and Bar-Sever, 2009), homogeneously reprocessed from 1996 to 2010, at 5 Antarctic coastal sites and 7 Arctic sites form the basis of this study (see Table 3 for the site details).

Secondly, at those site locations, also UV/VIS PW satellite retrievals by GOME, SCIA-MACHY and GOME-2 (called GOMESCIA hereafter), and thirdly Numerical Weather Prediction (NWP) model reanalysis (ERA-Interim of the European Centre for Medium-Range Weather Forecasts) PW are considered. The surface pressure at and the weighted mean temperature above the GPS sites, needed to convert the ZTDs to PWs, are also taken from ERA-Interim, but are corrected for an altitude difference between the model surface grid and the GPS site. The GOMESCIA dataset used here is the "Climate" water vapour product (Beirle et al. 2018), and is only available as monthly means. At the winter months of the highest latitude sites (especially at Antarctica), no measurements are available for GOMESCIA. To compare different datasets, we therefore show the correlation coefficients between the available PW monthly means in Fig. 13. Two main conclusions can be drawn
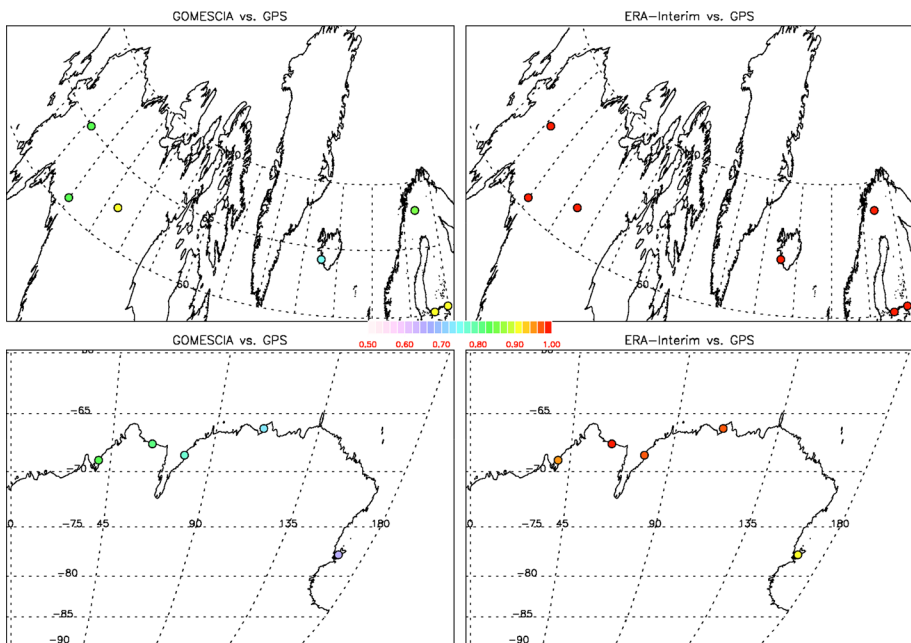
Fig. 13 Correlation coefficients between the monthly means of GOMESCIA and GPS (left) and ERA-Interim and GPS (right) for the Arctic stations (upper panels) and the Antarctic stations (lower panels)

from this figure: (1) the datasets compare better with each other for the Arctic than for the Antarctic sites, and (2) the agreement between GPS and ERA-Interim is better than the one between GPS and GOMESCIA, the purely observational datasets. We should mention here that no GPS-based dataset is assimilated in the ERA-Interim reanalysis.

The linear trends, calculated as the slope of the linear regression line fitted (by minimising the least squares) through the monthly anomaly PW time series during the 1996–2010 period, are shown in the three upper panel plots of Fig. 14 for different datasets. Overall, a moistening occurs for most of the sites at both the Arctic and Antarctic during this time
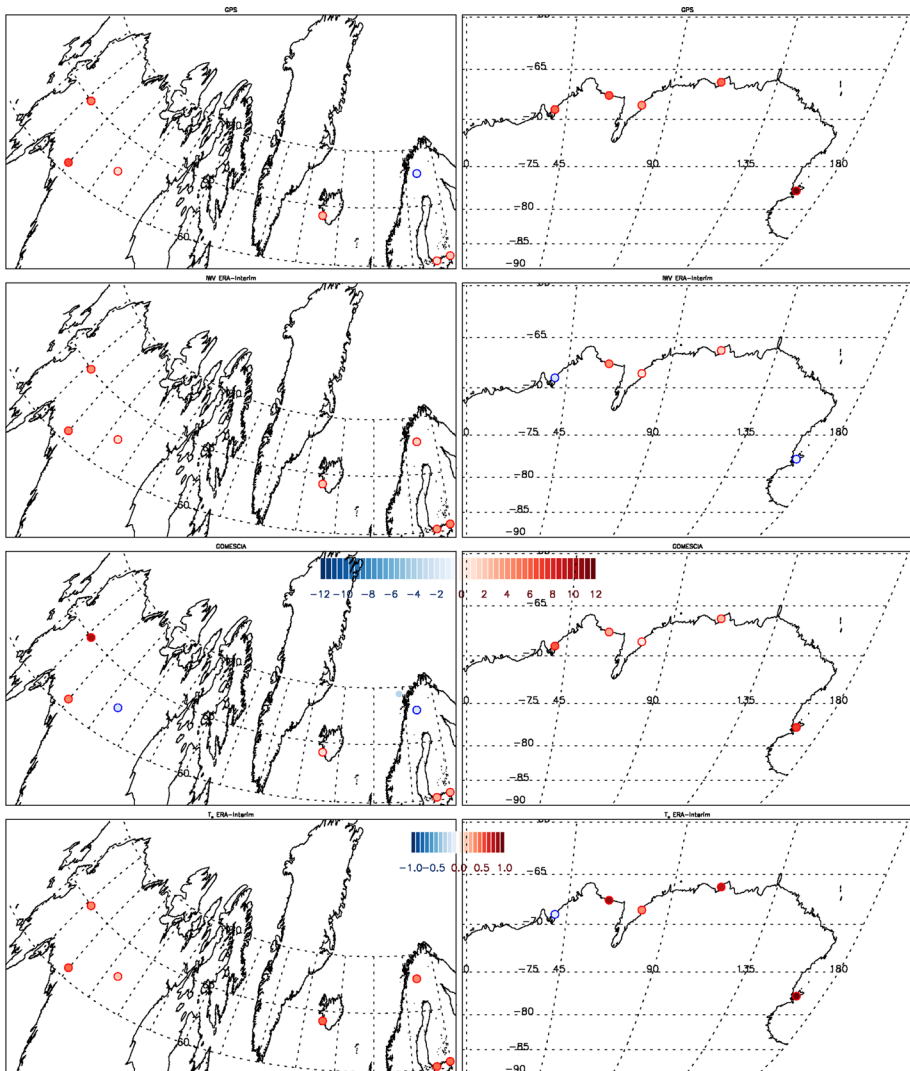
Fig. 14 PW trends [%/decade] for GPS, GOMESCIA, and ERA-Interim (from top to bottom) for the period Jan 1996–Dec 2010 for the Arctic (left) and Antarctic (right sites). For illustration, the lowest panels show the ERA-Interim surface temperature trends [°C/decade] for the same period
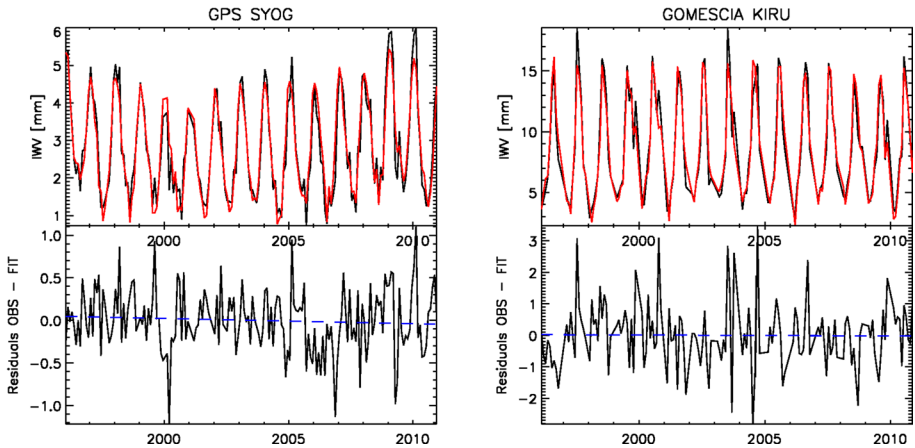
Fig. 15 Examples of the stepwise multiple linear regression fits (in red) to (left) the GPS monthly mean PW time series (in black) of SYOG (East Ongle Island, Antarctica) and (right) the GOMESCIA PW time series (in black) of KIRU (Kiruna, Sweden). The lower panels show the residuals between the observations and fitted time series of the upper panels (black minus red), with a linear fit to the residuals in blue (negative trend in both cases, but not significant)

frame, which seems to be associated with a warming (see lower panels of Fig. 14). The spatial consistency in the sign and the magnitude of the trends, at both the Arctic and the Antarctic sites, seems higher between GPS and GOMESCIA than for ERA-Interim. Parracho et al. (2018) also concluded that the uncertainties in current reanalysis like ERA-Interim remain quite high above Antarctica, and the spread between models is important. Rinke et al. (2019) found that four reanalyses agree on the spatiotemporal trend patterns for the Arctic, but substantially disagree on the regional trend magnitudes. If we average out different PW trend estimates, we found the highest moistening over Antarctica (GPS: 7.4±3.2%/decade, GOMESCIA: 4.9±4.2%/decade, ERA-Interim: 0.8±2.5%/decade), but a closer agreement between the mean moistening values over the Arctic (GPS: 2.7±2.3%/decade, GOMESCIA: 2.4±3.0%/decade, ERA-Interim: 3.3±2.2%/decade). However, taking into account the effect of auto-correlation and variability (see e.g. Weatherhead et al. 1998) 15 years of monthly data are not enough to detect a trend with a magnitude of 0.3 mm/decade (largest Arctic reanalysis median trend, Rinke et al. 2019) at a 95% confidence level with probability 0.90.

Therefore, we concentrate on the interpretation of the inter-annual variability, not necessarily dominated by one linear trend, by means of a stepwise multiple linear regression. With this approach, we fit the monthly means of different PW time series by the sum of the long-term means, a linear trend, and the monthly mean time series of candidate explanatory variables, if contributing statistically significantly to the PW variability. These explanatory variables are surface meteorological variables like temperature, pressure, precipitation (this latter only for the Arctic sites), but also teleconnection patterns (e.g. recurring and persistent, large-scale patterns of pressure and circulation anomalies that span vast geographical areas, see Van Malderen et al. 2018; Wagner et al. 2021) or climate/oceanic indices like the North Atlantic Oscillation (NAO), the El Niño Southern Oscillation (ENSO), etc. In general, the stepwise multiple linear regression fits are obtained by a procedure for which the following sequence of steps is performed: (1) explorative assessment of possible relationships between explanatory variables and PW by means of correlation maps, (2) check

the independence of the explanatory variables and remove those variables which have a strong correlation, (3) fit the monthly PW time series with all remaining explanatory variables individually, and (4) stepwise fit by including in each step an additional explanatory variable, in sequence of their explained variance derived in the previous step; only keep the variables which contribute significantly to the regression. A detailed description of the method can be found in Van Malderen et al. (2018) and the regression fits are shown for 2 sites (SYOG and KIRU) in Fig. 15, where examples of the stepwise multiple linear regression fits are presented (upper panel). The lower panels show the residuals between the observations and fitted time series of the upper panels. The used variables in the multiple linear regression equation were:

- For SYOG: the PW the long-term means, the surface temperature, the Atlantic Multi-decadal Oscillation, the Stratospheric Aerosol Optical Depth, the Pacific Decadal Oscillation, and the Tropical Southern Atlantic Index (explaining 91.56% of the variability);
- For KIRU: the PW long-term means, the surface temperature, the precipitation, the Eliassen-Palm flux, the Atlantic Multidecadal Oscillation, the North Atlantic Oscillation, the East Atlantic/West Russia oscillation, the Scandinavia and the Polar/Eurasia index (explaining 93.63% of the variability).

First of all, we found that the multiple linear regression fits explain very high percentages of the PW variabilities, both for the Arctic (GPS: 97.25%, ERA-Interim: 97.51%, GOMESCIA: 93.12%) and the Antarctic (GPS: 91.59%, ERA-Interim: 94.73%, GOMESCIA: 91.50%) and for the three datasets. The GOMESCIA PW time series do not fit as well, especially for the Arctic stations. The explained variabilities are higher for the Arctic sites than for the Antarctic sites, which might be explained by the fact that a higher number of explanatory variables is actually used in the regression for the Arctic sites. As a matter of fact, for all Antarctic sites and the three datasets used, the surface temperature is used as explanatory variable in the regression analysis, and explains the bulk of the remaining variability, after the long-term PW mean. For about half of the Antarctic sites, the Atlantic Multidecadal Oscillation (AMO) is also an important proxy in terms of the explained variability. As the AMO has a strong seasonal signal in its time series, the selection might be triggered by remaining seasonality in the time series, which could not properly be accounted for by the surface temperature and the long-term means. For the other explanatory variables, there is less consistency in their use for different sites and datasets. As the AMO does not show a clear trend, the surface temperature increase seems to be the main driver for the observed moistening over Antarctica.

For almost all the Arctic sites, besides the long-term means, also the surface temperature, tropopause pressure, and precipitation are present in the regression fits as explanatory variables, for the three datasets. The dominant presence of the tropopause pressure (and explaining high percentages of the variability for the North American Arctic sites) might be explained by the link of the PW variability with the time variability of the vertical extent of the troposphere, in which the bulk of the water vapour resides. Next to those meteorological variables, several indices related to the location of the North Atlantic jet stream and storm track, transporting heating, moisture, and momentum from eastern North America to western and central Europe, are also retained as explanatory variables. In particular, the North Atlantic Oscillation index is present in about 75% of the North American stations for the three datasets, while for the European sites, the East Atlantic, East Atlantic/West Russia and Polar/Eurasia indices are prominent. Their associated temperature and precipitation

patterns are indeed situated in Europe (see http://www.cpc.ncep.noaa.gov/data/teledoc/telecontents.shtml). In contrast with its presence for the Antarctic sites, the link between the Atlantic Multidecadal Oscillation, also frequently present as explanatory variable, and the PW variability of the Arctic sites is scientifically well established.

We also conclude that the Antarctic moistening seems to be dominantly driven by the surface warming there, while the Arctic PW variability at the sites can be explained by the combination of surface temperature, tropopause temperature, precipitation, and the North Atlantic atmospheric circulations.

3.2 Atmosphere, Mesosphere, and Ionosphere Coupling

For many years gravity waves (GWs) were extensively studied mainly at low and mid-latitude (see, e.g., review by Hocke and Schlegel, 1996; Oyama and Watkins 2011). GWs in the auroral ionosphere are still less understood. Furthermore, higher-frequency waves (acoustic waves, AWs) were poorly investigated because the standard mode of ionosonde operation typically is one sounding per 15 min. Therefore, to make further progress in this field, more frequent observations at high latitudes are required. Such observations are available from the Sodankylä Geophysical Observatory (SGO) ionosonde, located in the auroral zone, operating with a time resolution of 1-min. Kozlovsky et al. (2013) used this ionosonde data to study travelling ionospheric disturbances (TIDs) during the interval 10–16 local time. Their analysis shows that TIDs of periods from 5 min to 2 h exhibit minima in winter and maxima in summer. These annual variations anticorrelate with variations in true height, namely, the largest relative amplitudes occur in summer, when TIDs were observed at minimal heights. The authors suggest that the summer increase in shorter-period TIDs is due to the lowering of the reflection to the height where the Brunt-Väisälä period is smaller and, hence, shorter-period GW exist. The authors also showed that the summer maxima were most prominent during minimal solar activity and that this annual variation seems less prominent when solar activity increases.

Obtaining high-rate data from the mesosphere-lower thermosphere region is a challenge, and continuous ground observations of the mesospheric wind and temperature in the vicinity of the stratospheric polar vortex edge are still rare. Furthermore, sudden stratospheric warming (SSW) manifestations, often observed in the northern hemisphere, at the polar high altitudes > 100 km are even less experimentally documented than those in lower altitudes. A network of instruments allows for their detailed study (Lukianova et al. 2015; Rietvield et al. 2008). SSW observations in the southern hemisphere are rare, especially the strong ones. This is attributed to the topography and weaker planetary wave forcing, however, there is a smaller network of ground-based instruments for observations (Krüger et al. 2005; Yamazaki et al. 2020).

In the northern hemisphere, the ionosonde measurements routinely performed at SGO provide an important new data set. Lukianova et al. (2015) studied mesosphere-ionosphere anomalies using data recorded by the rapid-run SGO ionosonde during a period around the major SSW of 2009. They found among other the following features:

1. Mesospheric cooling is almost of the same value as stratospheric warming (~ 50 K), but the former decay faster than the latter. Furthermore, the mesospheric minimum occurs 1 day ahead of the stratospheric maximum.

2. Just after the mesospheric temperature reaches its minimum, the GWs occurrence in the ionosphere with periods of 10–60 min decay abruptly while the GWs with longer periods are not affected. The effect of such weakening of the mesosphere-ionosphere coupling may be explained by selective filtering and/or increased turbulence near the mesopause.

In addition to the SGO ionosonde, the dynasonde located in Tromsø, with typically 6-min time resolution, is available (Rietveld et al. 2008) and revealed to be an interesting further resource to study the thermospheric gravity wave activity (Zabotin et al. 2015).

In the southern hemisphere, airglow all-sky imagers have been used since 2007 at the Brazilian Antarctic Station (EACF) to investigate mesospheric gravity waves, from which data it is possible to obtain the GWs properties as horizontal wavelength, period, phase speed and propagation direction (Bageston et al. 2009, 2011a, b). More recently, the VLF measurements at EACF also started to be used to characterise the GWs in the lower ionosphere. GWs produce fluctuations of the electrical conductivity in the D region, which are detected as VLF amplitude and phase variations. So GWs parameters, such as period and time duration, can be obtained from the spectral analysis of VLF signal fluctuations (Correia et al. 2020).

3.3 Climatology of the Ionosphere

Long-term studies of the polar ionosphere have been made using various techniques including VLF, GNSS-TEC, auroral imaging, ionosondes, scintillation monitors, riometers, satellite in situ data, SuperDARN radars, and combinations of these instruments.

To obtain a climatological assessment of the polar ionosphere the description of the medium should be done for at least one solar cycle to account for different levels of solar activity. A purely empirical approach is not always applicable because of the paucity of data, both in terms of the length of the series and coverage. In these cases, the use of climatological models can support the reconstruction of the full picture. The most completed data series are those derived from the ionosonde observations because the vertical sounding was the first experimental setup put in place to probe the ionosphere. At high latitudes, the coverage and the data availability are limited due to severe environmental conditions. Nevertheless, to date, the scientific community can rely on almost six solar cycles worth of data also thanks to contributions made during the International Geophysical Year (IGY) (Alfonsi et al. 2008a and references therein). Thanks to these contributions, several empirical and semi-empirical models have been proposed to reconstruct the global behaviour of the ionosphere (including the high latitude ionosphere). Among others, we mention the International Reference Ionosphere (IRI) and the NeQuick models. The IRI model is based mainly on ionosonde data and supported by measurements acquired by incoherent scatter radars, the ISIS and Alouette topside sounders, and in situ instruments on several satellites and rockets (https://iri.gsfc.nasa.gov/). The NeQuick model is based on a series of electron density profiles derived from the inversion of ionograms (https://t-ict4d.ictp.it/nequick2) (Radicella and Leitinger 2001; Nava et al. 2008; 2011).

A purely empirical assessment derived from historical ionosonde data is the primary resource of several papers that investigated possible signatures of anthropogenic (greenhouse effect; Rishbeth 1990) and natural (geomagnetic variation; Mikhailow and Marin 2001) phenomena possibly affecting the long-term changes of the ionosphere (Laštovička 2017). In this framework, some attempts have been made to study the climatology of the

ionosphere at high latitudes (Alfonsi et al. 2008b and references therein; Roininen et al. 2015 and references therein).

The riometer data, accounting for the absorption of the cosmic radio noise by free electrons in the ionosphere, can provide important information on the ionospheric conditions affecting HF communication at high latitudes. Statistical analysis of riometer data, when compared to the flux of the precipitating electrons, can reveal the loss of electrons from the magnetosphere (see, e.g., Kellerman et al. 2015 and references therein). Continuous monitoring of energetic particle precipitation by riometers allows long-term global studies, such as statistical behaviour of solar proton and electron precipitation impact regions in the atmosphere (e.g. Kilpua et al. 2020; Heino et al. 2019; Heino and Partamies 2020). The two-dimensional CNA distribution, in turn, facilitates more detailed spatial distribution studies of hard precipitation regions in comparison with other observations (e.g. Grandin et al. 2017a,b). The new spectral riometer measurements will provide better means of inverting the actual D-region electron density profiles, and consequently the energetic particle precipitation spectra, from the riometer data (Kero et al. 2014).

As mentioned in Sect. 1, since the early measurements in 1965, the Sodankylä Geophysical Observatory has operated and maintained the Finnish Riometer Chain, having long-term continuous riometer observations at Kevo ($L=6.5$), Kilpisjärvi ($L=5.9$), Ivalo ($L=5.5$), Sodankylä ($L=5.1$), Rovaniemi ($L=4.8$), Oulu ($L=4.3$), and Jyväskylä ($L=3.7$). Furthermore, in collaboration with the University of Lancaster (UK), riometers have been operated in Abisko ($L=5.6$), in Ramfjord ($L=6.45$), in Hornsund ($L=13.1$), as well as the imaging riometer IRIS ($L=5.9$). Concerning the magnetosphere, these stations are located in L shells between 3.7 and 6.5, i.e. mapping all the relevant magnetic latitudes of the outer Van Allen radiation belt and the auroral oval and hence providing a unique spatial coverage for monitoring various energetic particle precipitation populations.

In their early paper, Ranta and Ranta (1977) concluded, by using the Finnish riometer chain data, that the diurnal variation in absorption has one maximum near noon at latitudes $< 62°$N and two maxima, one in the morning and another at midnight at latitudes $> 62°$N. The first maximum is associated with the solar controlled photochemistry (recombination) and the latter was found to be magnetospherically controlled, i.e. at the northern stations (Kevo, Ivalo, Sodankylä, Oulu) the riometer absorption was found to correlate much better with magnetic activity than with sunspot number. Since then the riometer chain data has been used in various long-term and case studies of space weather-related ionisation events, such as electron precipitation, solar proton events, and solar X-ray flares, in the polar latitudes. Some of the recent studies are listed in the next section.

Kilpua et al. (2020) studied electron precipitation associated with the interplanetary coronal mass ejections (ICME), i.e. the coronal mass ejection observed close to the Sun (CME) when it moves in the interplanetary space. In their superposed-epoch-analysis of the riometer chain data gathered during 1997–2012, they found that the fraction of ICMEs causing enhanced absorption was high (mostly 80%–95%) at auroral latitudes (IVA, SOD, and ROV) and the sub auroral station, OUL, but dropped clearly at the lowest-MLAT station, JYV. In particular, the impact of the so-called "sheath" periods of the ICMEs were found to be considerably lower at JYV than at the other stations. In a somewhat similar statistical manner, Grandin et al. (2017a) studied the impact of the solar wind high-speed streams on the high-latitude ionosphere. These events were divided into two categories, labelled "long" and "short", depending on the duration of the solar wind speed increase to a maximum value. They found that the long events produced more CNA events than
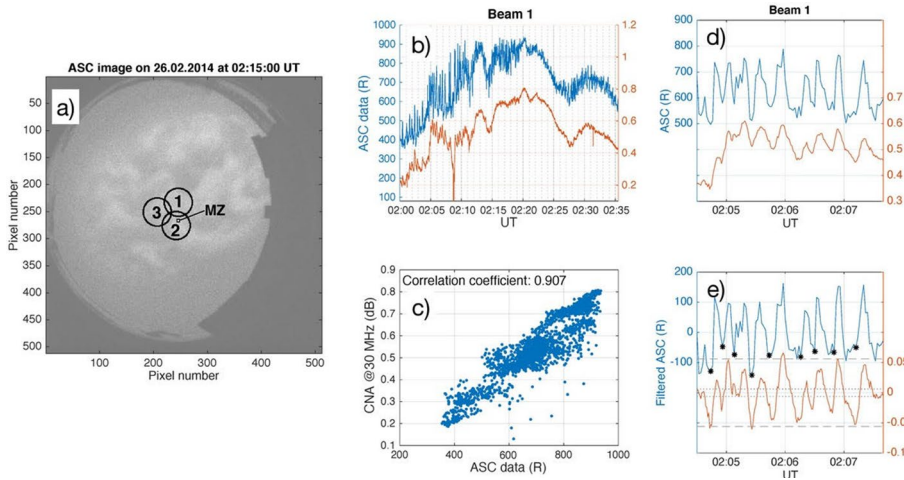
Fig. 16 Correlations between CNA and optical data are seen by Grandin et al. (2017b). Panel **a** Position of the KAIRA beams number 1, 2, and 3 on an example Kilpisjärvi all-sky image. Panel **b** Time series of the 427.8 nm auroral emission (blue) and cosmic noise absorption (orange) between 02:00 and 02:35 UT within KAIRA beam number 1. Panel **c** correlation between cosmic noise absorption and 427.8 nm auroral emission. Panel **d** as panel b, but zoomed in. Panel **e** high-pass-filtered optical (blue) and CNA (orange) data

the short HSS events and produced CNA down to $L = 4.5$, but at $L = 3.8$ the CNA was not noticeably affected by HSS events.

One of the several riometer studies has focused on the energetic electron precipitation caused by pulsating aurorae. Grandin et al. (2017b) used the individual spectral riometer beams of the KAIRA facility in conjunction with the pulsating aurora patches and found a clear pulse-to-pulse correlation with the cosmic radio noise absorption and the optical signals (Fig. 16). This was the first direct observation of the one-to-one correlation between the pulsating aurora optical signatures and an identical modulation found in the high-energy precipitation flux using spectral riometry (Kero et al. 2014).

Tesema et al. (2020) combined a dataset of All-Sky auroral images, EISCAT radar experiments, and KAIRA riometer data to study the energetics of different types of pulsating aurorae, i.e. amorphous pulsating aurora (APA), patchy pulsating aurora (PPA), and patchy aurora (PA). Their findings suggest that the precipitating electrons responsible for APA have a lower energy range than PPA and PA types. Among the three categories, the magnitude of the maximum electron density shows higher values at lower altitudes and in the late magnetic local time (MLT) sector (after 5 MLT) during PPA than during PA or APA. They also found significant ionisation down to 70 km during PPA and PA, which corresponds to energy levels of ~200 keV of the precipitating electrons.

Another focus area in riometer studies has been Solar Proton Events (SPEs), especially for verifying the cut-off magnetic latitudes of these events (see, e.g., Rogers et al. 2016; Heino et al. 2019; Heino and Partamies 2020).

In addition to the detection of energetic particle precipitation, the riometer technique can be used also for investigating photoionisation events, most notably Solar X-ray Flares, as most recently done by Ogunmodimu et al. (2018) by using the IRIS imaging riometer data.

In recent decades, additional data sources have been used for reconstructing the long-term behaviour of the ionosphere. On the ground, the HF backscattering data from the SuperDARN network and the EISCAT, Poker Flat Incoherent Scatter Radar (PFISR) and Resolute Bay Incoherent Scatter Radar (RISR) campaigns gave a significant input. For instance, the SuperDARN line-of-sight velocity data collected in the two hemispheres allowed us to derive a climatological model of the ionospheric convection parameterised by the Interplanetary Magnetic Field (IMF) condition and the dipole tilt angle (Pettigrew et al. 2010). More than 30 years of data from the EISCAT Tromsø radar have been recently analysed by Bjoland and collaborators (2017) to study the features of the E-region ion temperature and the peak height of the Hall conductivity. Vickers et al. (2014) used the EISCAT Svalbard radar to study the quiet-time (Kp < = 2) polar neutral thermosphericdensity change at 350 km altitude over 13 years (2000–2012). They found a ~ 5% decrease over 13 years, which is consistent but slightly greater than previous satellite drag studies at lower latitudes. Yamazaki et al. (2017) used the EISCAT Svalbard (1999–2014, 16 years) and Tromsø UHF (1981–2014, 34 years) radars to study ion field-aligned velocity climatology for both geomagnetically quiet (Kp ≤ 2 +) and active times (Kp ≥ 3-). They found during daytime, the direction of the average field-aligned ion velocity reverses from downward to upward around 350 km. The reversal height increases with solar activity. During nighttime, the average field-aligned ion velocity is predominantly upward at all heights from 175 to 475 km. The magnitude of the night-time field-aligned ion velocity increases with geomagnetic activity. The magnitude of the average field-aligned ion velocity is on the order of 10 m/s. The results were similar for both the polar cap (Svalbard) and auroral oval (Tromsø).

On shorter time scales (of a few years), the in-situ data, such as those provided by CHAMP, COSMIC, and Swarm satellites, can also provide additional insights into the ionospheric climatology. For example, Arras et al. (2008) published a study on the global distribution of sporadic E derived from small-scale fluctuations of the GPS L1 SNR (Signal-to-Noise Ratio) applied to CHAMP, GRACE, and FormoSat-3/COSMIC radio occultation measurements. Another example of climatological study from in situ data is given in the paper by Spicher et al. (2017) that presents the spatial and seasonal distributions of the polar cap patches, which are regions of enhanced plasma density which can result in significant plasma structuring, identified by the Swarm satellites between December 2013 and August 2016. Using the RISR Canadian face data (RISR-C), Ren et al. (2018) statistically analysed the plasma properties of polar cap patches, including vertical profiles of plasma density, temperature, flux, and their day-night asymmetries. Recently, Ren et al. (2020) used three years of PFISR data and characterised the ion upflow and downflow in the subauroral and auroral zone. They found that ion upflows occur more often on the nightside than on the dayside and are often associated with plasma temperature and density enhancements. The upflows also prefer to occur during enhanced solar and IMF drivers and geomagnetic activities.

The climatology of the ionospheric scintillation was first provided through the use of semi-empirical models, such as the WideBand MODel (WBMOD) (Fremouw and Secan, 1984). The WBMOD is a global model based on a collection of empirical models that describes the geometry, orientation, strength, and motion of the ionospheric irregularities, combined with a propagation model that calculates the effects these irregularities will have on a given system. An upgrade was released to model the ionospheric scintillation at high latitudes (Secan et al. 1997). Another semi-empirical tool, the WAM model, has been proposed to reproduce the high latitude scintillation (Wernik et al. 2007). An alternative attempt to scintillation modelling has been done by

Beniguel (2002), who proposed the Global Ionospheric Propagation Model (GIM). Like the WBMOD, the WAM and GIM combine the information provided by in-situ electron density data with a propagation model to provide the scintillation climatology.

With the beginning of the GPS era in the 1990s, the exploitation of GNSS signals from ground-based receivers opened the possibility to derive an empirical climatology of TEC and ionospheric scintillation in high latitude regions. Among the pioneers are Spogli et al. (2009), Prikryl et al. (2011) and Jiao et al. (2013).

3.3.1 VLF and GNSS to Identify the Long Term Main Features of the Ionosphere

The AARDDVARK VLF network has been applied to the long-term determination of energetic electron precipitation into the auroral atmosphere (Neal et al. 2015) and for the development of a model of energetic electron precipitation during geomagnetic storms (Van de Kamp et al. 2016). VLF has also been used in long term studies such as the one from Cresswell-Moorcock et al. (2015) which are necessary to model the diurnal changes in narrowband signal phase and amplitude caused by solar irradiance so that short-term variations such as those caused by flares (and other phenomena such as solar proton events, particle precipitation, etc.) can be identified accurately from VLF data.

The TEC as observed using geodetic GNSS receivers in the polar regions has been used for several long-term studies of the polar ionosphere in combination with VLF and scintillation studies. The long-term maximum daytime (12:00 LT) ionospheric electron density variations were investigated from GPS-TEC and VLF observations at Estação Antártica Comandante Ferraz (EACF, 62.1°S, 58.4°W) from 2004 to 2011. The observations have shown the following long-term variation that is controlled by the 11-year solar cycle (Correia et al, 2011, 2013a,b): the ionospheric conditions are affected by electrodynamic processes, which during quiet geomagnetic periods are associated with the seasonal variation in the solar illumination and with the 11-year solar cycle. These processes can result in steeper electron density gradients in the ionosphere and strong irregularities, which produce fluctuations in the amplitude and phase of GNSS signals. Moreover, the long-term daytime GPS-TEC at the geomagnetic mid-latitude station EACF showed that its correlation with solar radiation intensity is different between the summer and winter seasons. In winter the GPS-TEC at EACF shows no significant correlation with solar flux, which can be attributed to the high solar zenith angles during this season (Correia et al, 2013a). In summer the GPS-TEC is higher during low solar activity, but when the solar activity increases TEC is higher during the equinoxes (Correia et al. 2013a). Similarly, using GPS TEC measurements for a duration of 5 years (2013–2017), Shreedevi et al 2019 studied the morphological variations in the plasma density at the Indian Antarctic station Bharati (69.40 S, 76.18 E; 76.69S MagLat, 126.93E MagLon) during both quiet and magnetically disturbed periods. They showed that plasma density at the polar cusp station Bharati during magnetically quiet periods exhibit semi-annual variation and a strong dependence on solar activity. Based on the nature of plasma density variations during 23 geomagnetic storm events (during 2013–2017), the storm time response of the TEC at Bharati was shown to depend on the onset time of the storm. Further, they concluded that the dynamic nature of the location of the polar cusp station with respect to the position of the polar cap played an important role in deciding the plasma distribution at Bharati. These results are in agreement with the importance of the solar flux intensity and solar zenith angle on

the ionosphere ionisation processes, especially at higher latitudes (Bhawre et al. 2011; Purohit et al. 2011). The winter anomaly was not observed in the GPS-TEC measurements acquired at EACF, which is in agreement with Torr and Torr (1973) and Zhao et al. (2007). They also observed peak electron densities higher in summer than winter in the South Pacific-South Atlantic regions, and suggested this was due to particle precipitation in these regions, that surround the South Atlantic Magnetic Anomaly (SAMA). On the other hand, the amplitude of VLF signals shows the maximum daytime amplitude and presents a strong day-to-day variation during wintertime, as evidenced by the observations using different VLF paths mostly located in one hemisphere (Correia et al. 2011, 2013b). These variations in the VLF amplitude were attributed to density fluctuations produced by the 16-day planetary waves of stratospheric/tropospheric origin (Correia et al, 2011, 2013b). The lower parts of the ionosphere might be affected by the 16-day planetary waves that might modulate the 12 h tide, which is used to explain the observed variations in the mesosphere-lower thermosphere region, and are attributed to a non-linear interaction of the tide with planetary waves (Pancheva et al. 2002).

Bergeot et al. (2014) characterised the differences in the ionosphere-plasmasphere climatological patterns of TEC over Antarctica. They reprocessed the GNSS (GPS + GLO-NASS) data available from 1999 up to 2020 for stations situated at latitudes below 50°S using the ROB-IONO software (http://www.gnss.be/Atmospheric_Maps/ionospheric_maps.php#Refraction_less). The entire network comprises stations with observation duration from 60 days to more than 18 years and with more than 80 stations after 2010. The output consists of slant TEC (sTEC) estimated every 30 s between every station/satellite pair. Then the sTEC is projected to vertical, vTEC, at ionospheric pierce points (IPPs) using a mapping function (Mannucci et al. 1993) with thin shell layer at 450 km. Only data observed along ray paths with elevation angles greater than 40° were considered to avoid as much as possible the effect of multipath signals. When using a thin shell layer to estimate the IPP coordinates (Wild 1994), they estimated a daily position of all the stations in the entire network based on a pseudo-range solution using the GAMIT processing software (v10.61; Herring et al. 2018). The estimated vTEC data set is then employed to constrain an empirical model to predict the IPTEC from the F10.7P solar index (i.e. the mean of daily F10.7 of the day of interest and its average over the previous 81 days) as input using a least-square adjustment. To minimise the differences between the modelled and observed vTEC at IPPs they considered: (1) an eight-order polynomial function with monthly coefficients between the vTEC and F10.7P; (2) a discretisation concerning different zones over Antarctica region to highlight different climatological patterns. The resulting model permits the estimation of the vTEC at a given location and specific time in Coordinated Universal Time (UTC), Solar Local Time (SLT), and Magnetic Local Time (MLT) in each zone. From the output of this model, they focused on a specific region above the Antarctic Peninsula (Zone 16, top on Fig. 17) and the Eastern part of the continent (Zone 11, bottom on Fig. 17).

Regarding the resulting models in Fig. 17, we highlight the fact that the vTEC climatological patterns over Antarctica vary significantly with the location. Above the Antarctic Peninsula, the maximum vTEC occurs during the evening and afternoon times for the three time definitions and should be due to the Weddell Sea Anomaly which is nowadays explained by longitudinal changes in the neutral winds and neutral densities (e.g. Richards et al. 2017). During the winter season SLT noon TEC maximum occurs over the Antarctic Peninsula. In comparison, in the Eastern part of Antarctica, there is no clear variation over the year in the vTEC in SLT and MLT, with a maximum around local noon during the
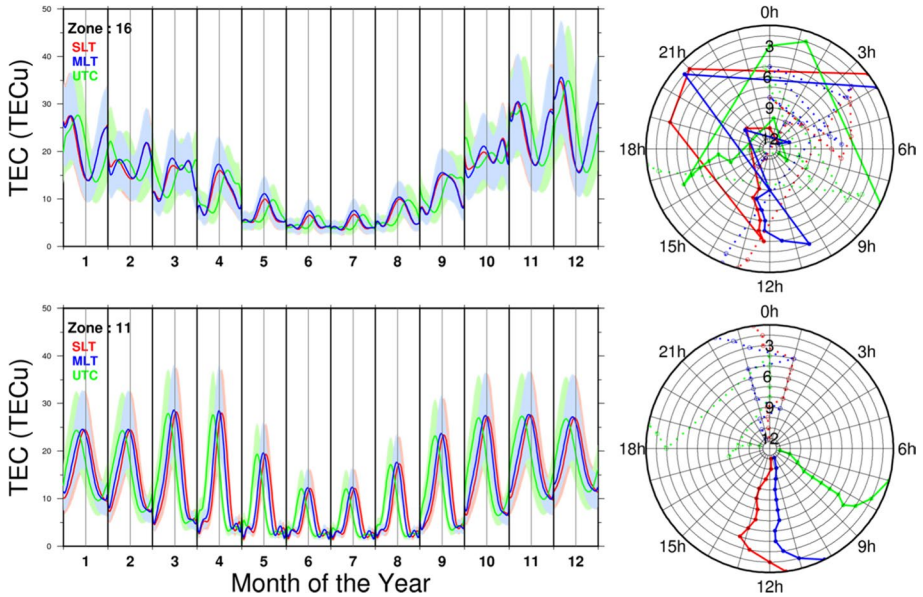
Fig. 17 Monthly climatological behaviour of the vTEC for an identified pattern and three different time definitions: solar local time (SLT, red), UTC (green), and magnetic local time (MLT, blue). The coloured lines are the diurnal variation in the vTEC (the grey line is noon) for medium solar activity level (F10.7P = 120 sfu). The spread of the colours stands for low and high solar activity (F10.7P = 80 and 160 sfu, respectively). Top: for the Antarctica Peninsula region. Bottom: for the eastern part of the continent. On the right are the corresponding time of occurrence of maximum (bold lines) and minimum vTEC (dashed lines) with the internal circles representing the month of the year with December at the centre of the picture

entire year meaning less impact of external forces (i.e. neutral atmosphere variations) than the solar elevation angle.

3.3.2 Ionospheric Scintillation Studies Using GNSS Data

Ionospheric scintillation is characterised by S4, the amplitude scintillation index derived from amplitude fluctuations averaged over 60 s, and σ_Φ, the phase scintillation index typically derived from phase fluctuations averaged over 60 s (Fremouw et al. 1978). When studied with GNSS receivers, both S4 and σ_Φ are derived from 50 Hz measurements at the L1 frequency. The scintillation climatology can be derived by assessing the occurrence of the two indices above certain thresholds. A key issue is the choice of the cut-off frequency adopted to derive the phase scintillation index. Such choice can jeopardise the proper assessment of the phase scintillation level and it is currently a matter of debate on the definition of scintillation. Indeed, some recent papers support the definition of scintillations as due to the sole diffractive (stochastic) effects, claiming that the deterministic contribution to the refractive effects can be mitigated through an adaptive choice of the cut-off frequency. Such a choice would lead to a reduction in the "phase-without-amplitude scintillation occurrence" (Mushini et al. 2012), possibly due to the choice of a fixed cut-off frequency of 0.1 Hz (Van Dierendonck et al. 1993) for phase detrending. In this framework, some promising attempts to find the optimal choice have been made by Niu et al. (2012), Wang et al. (2018), Mc Caffrey and Jayachandran

(2019), Ghobadi et al. (2020) and by Spogli et al. (2021). To assess the scintillations climate, the challenge is to find the "best" cut-off frequency to filter long-term (years) data series. De Franceschi et al. (2019) have demonstrated that this is not an easy task. For scintillation derived from GNSS ionospheric data suitable metrics and even a univocal definition of scintillation have not yet been agreed upon by researchers in the field. The analysis of the ionospheric scintillation is often made to infer the physics of the perturbed plasma, in terms of scale sizes and dynamics of the ionospheric irregularities. For the mitigation and prediction of the GNSS signal corruption due to scintillations, the analysis is focused mainly on the diffractive (stochastic) effects, which are hard to forecast and mitigate. In turn, the advancement of knowledge about the irregularities causing scintillations boosts the improvement in space weather tools. Therefore, the question is whether the deterministic effects can be included in the scintillation term. Since these effects are associated with the dynamics of the ionosphere, their study is crucial to assess the scenario potentially disruptive for GNSS signals propagation. In the end, stochastic and deterministic effects on the propagation of the radio signals should be both taken into account for scientific studies and space weather applications, but referring to pioneer and review works (Yeh and Liu, 1982; Rino, 2011) the term scintillation should be associated with the stochastic contribution from diffraction.

As a new contribution to the climatological assessment of TEC gradients and scintillations, we propose an unprecedented climatological assessment of ionospheric scintillations and TEC gradients at Antarctic sub-auroral/auroral latitudes observed from the South African Antarctic station, SANAE IV (71°40′22″S, 2°50′26″W), and from
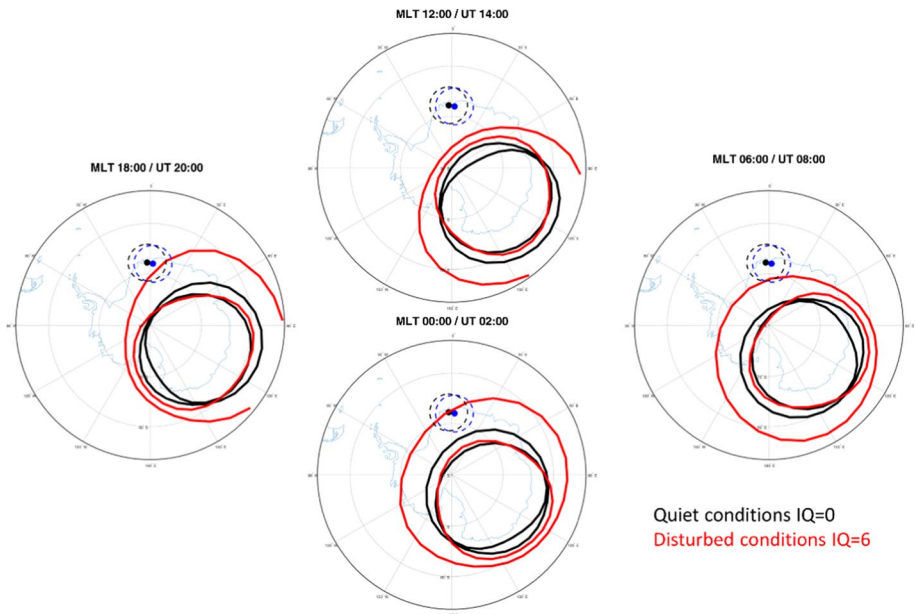
Fig. 18 Position of the poleward and equatorward boundaries of the Feldstein auroral oval for quiet (IQ = 0, black lines) and disturbed conditions (IQ = 6, red lines) at 12 MLT (top), 6 MLT (right), 00 MLT (bottom) and 18 MLT (left). The corresponding UT time is also reported in the figure. Black and blue dashed lines indicate the field of view at 350 km spanned by the receivers located at SANAE (black dot) and Troll (blue dot) considering an elevation angle mask of 30°

the Norwegian one, Troll (72°00′42″S 2°32′06″E). The receiver in SANAE is a Septentrio PolaRxS receiver, while Troll is equipped with a NovAtel GPStation-6. The GPStation-6 receiver was installed at Troll in December 2017 (Skjæveland et al. 2021). PolaRxS and GPStation-6 provide access to ionospheric delay and related measurements from not only the GPS of navigation satellites but also from the Russian GLObal NAvigation Satellite Systems (GLONASS) and European Galileo satellites. The field of view of the GNSS satellites in view from the stations is mainly sub-auroral, but under perturbed geospace conditions the station can enter the auroral oval (Fig. 18) according to the Feldstein model, the boundaries are identified by the black curve for quiet and the red curve for disturbed conditions, respectively (Holzworth and Meng, 1975).

To assess the multipath contribution to the received signal, analysis of the site characterisation has been made evaluating the variation in the mean Code Carrier standard deviation of the signal concerning the elevation angle. Such quality check (not shown) suggests applying an elevation mask of 30° to the scintillation dataset. Moreover, the high noise level recorded on the GLONASS signals and the analysis of data gaps, confine the considered dataset to the years 2017 and 2018 on the signals transmitted by GPS and Galileo satellites. Our assessment of TEC and ionospheric scintillations shows the frequent occurrence of moderate to high σ_Φ levels ($\sigma_\Phi > 0.25$ radians). The S4 climatological behaviour testifies an infrequent occurrence of moderate amplitude scintillation (S4 > 0.25). The σ_Φ index considered in our analysis is provided by the receiver firmware applying a cutoff frequency of 0.1 Hz for detrending the phase values over 1 min. Such a choice can mislead the scintillation occurrence identifying several phases without amplitude scintillation events (McCaffrey and Jayachandran 2019). De Franceschi et al. (2019) have extensively discussed how hard is the identification of the optimal cut-off frequency at a statistical level to describe the long-term variation in scintillations at high latitudes. Hence, following their method, here we consider as actual scintillations those events occurring simultaneously on the amplitude and the phase of the GNSS signals. The other enhancements of σ_Φ
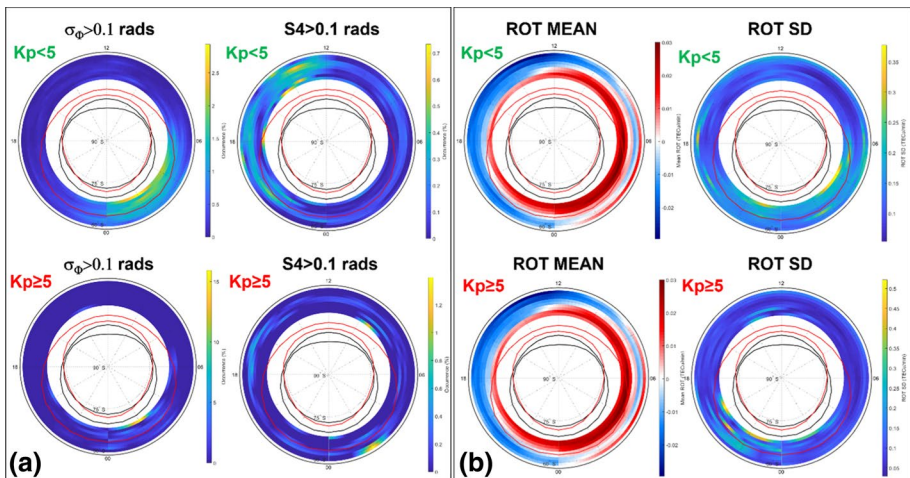
Fig. 19 Scintillation occurrence and ROT recorded over SANAE during 2017–2018. **a** Scintillation occurrence for σ_Φ (left) and S4 (right) > 0.1 (radians and dimensionless, respectively) sorted by Kp < 5 (top) and Kp ≥ 5 (bottom). **b** ROT mean (left) and standard deviation (right) sorted by Kp < 5 (top) and Kp ≥ 5 (bottom)

are considered as phase fluctuations likely due to large-scale (i.e. larger than few hundreds of meters) TEC gradients.

According to the NOAA G-scale (https://www.swpc.noaa.gov/noaa-scales-explanation), the geomagnetic field conditions are considered quiet when Kp is < 5, while Kp ≥ 5 identifies the conditions from minor to extreme stormy levels (www.swpc.noaa.gov/phenomena/geomagnetic-storms). Hence, we have sorted the scintillation and the ROT (Rate of TEC change) recorded over SANAE according to these two categories (quiet and disturbed) and we have described our results in polar maps of Altitude-Adjusted Corrected GeoMagnetic (AACGM) latitude (Baker and Wing 1989) and Magnetic Local Time (MLT) (Fig. 19). As the GNSS receiver field of view covers mainly the sub-auroral sector (see Fig. 18) we preferred the use of Kp instead of AE index to identify the quiet and disturbed conditions. Similar to Fig. 18, the modelled auroral oval is also reported on the scintillation occurrence and ROT maps. This analysis describes the ionospheric climate over SANAE during the period spanning 2017 and 2018 derived from the GNSS 1-min data, while Troll data refer to 2018. Concerning SANAE, under quiet conditions (black contours of the auroral oval) (Fig. 19(a)) S4 exceeds very rarely the weak (> 0.1) scintillation threshold (see the colour bar). As it is not associated with a σ_Φ enhancement, this increase does not seem to be due to ionospheric scintillation, but is likely due to residual multipath that is not properly removed with the 25° elevation mask. A weak increase in S4 accompanied by an evident enhancement σ_Φ in the post-midnight sector could be identified as an ionospheric scintillation signature. From Fig. 19(b) the ROT mean and standard deviation confirm the possible presence of TEC gradients with a high variability of scale sizes in the midnight and post-midnight hours, especially at higher latitudes. The comparison between the S4 and the σ_Φ occurrence under stormy conditions (Fig. 19(b)) identifies very well a region of enhancement around 02:00 MLT from lower to higher latitudes. In that sector, the ionospheric scintillations occur frequently because they are detectable at a climatological level over two years of 1-min data. The interpretation of the maps of ROT mean and standard deviation under perturbed conditions (Fig. 19(b)) testifies to the presence of large-scale TEC gradients in the auroral and sub-auroral regions and a significant variety of irregularities at different scale sizes around midnight. In the post-midnight, the presence of irregularities with
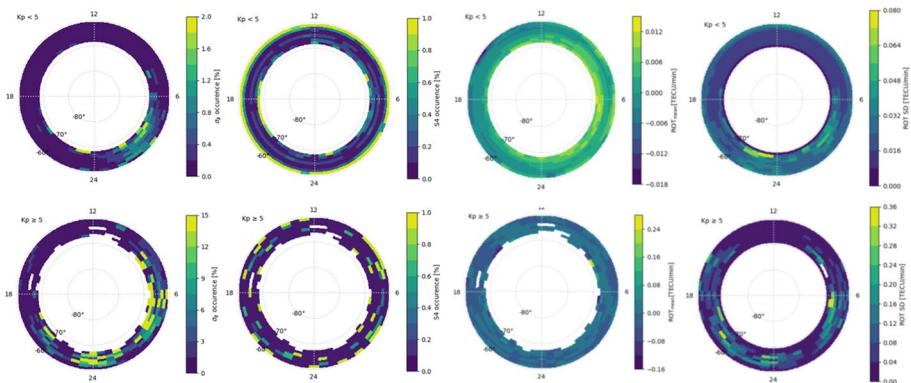

Fig. 20 Occurrence of scintillations indices σ_Φ and S4 with values larger than 0.2 (radians and dimensionless, respectively), as well as mean ROT and its standard deviation for Kp < 5 and Kp ≥ 5. Results correspond to the measurements for the year 2018 over Troll station. The plots are shown in the MLAT-MLT coordinates

different scale sizes results to be more confined to higher latitudes, suggesting a possible role of the irregularities originating from the polar cap (such as polar cap patches) and entering the auroral region (red curve boundaries in the figure).

In Fig. 20, the statistics of the parameters for the whole year of 2018 over the Troll station are shown for low (Kp < 5) and high (K > = 5) geomagnetic activities in a similar format as in Fig. 19. To calculate the statistics, we used the threshold elevation angle of 30°. For the scintillation indices σ_Φ and S4, we show the occurrence of values larger than 0.2 (radians and dimensionless, respectively). We also present the mean rate of change of TEC (ROT) and the standard deviation of ROT over the whole year. In the analysis, we use the IPP at the altitude of 350 km and AACGMv2 for mapping to the MLAT-MLT coordinate system. The results from Troll largely agree with the observations over SANAE-IV. We also observe that there are more frequent scintillations over Troll, which is located further south, especially during geomagnetically active periods.

3.3.3 Satellite-Based Studies

Polar-orbiting satellites can provide additional and complementary information to fill knowledge gaps, by allowing for in-situ measurements of ionospheric parameters along their orbits and also characterising the top-side ionosphere with the help of GNSS signals. Although polar-orbiting satellites in low-earth orbits have rather short pass times over regions of interest and their orbits longitudes are often changing fast, they can provide long-term statistics and allow for climatology studies.

Recently, such statistical studies have been carried out with several satellite missions as mentioned earlier in this section, including the Swarm mission, which is a constellation of three identical satellites. One example of such study is the interhemispheric climatology study of the polar cap patches, which are regions of significantly enhanced plasma density relative to the background that is being convected over the polar cap. The occurrence of polar cap patches in the northern hemisphere is significantly higher in the local
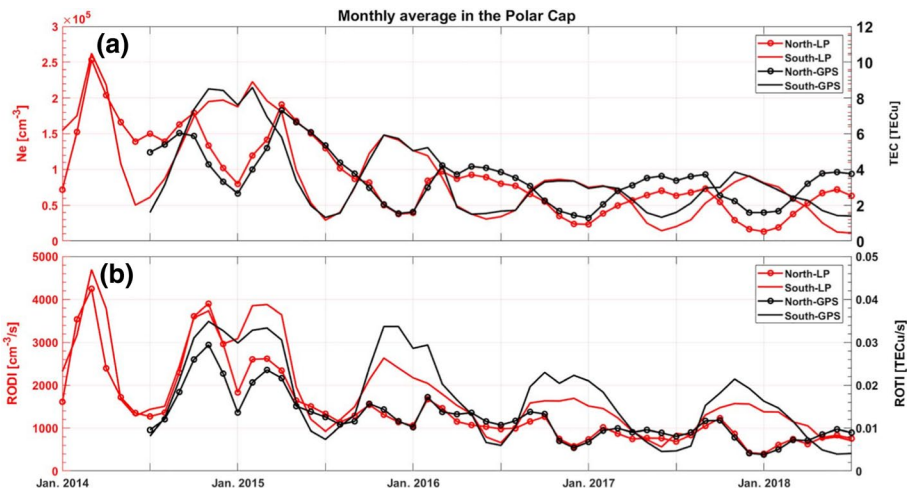
Fig. 21 **a** Seasonal variations in the plasma density (Ne), measured by the Langmuir Probe (LP), and TEC, measured by the GPS receivers, in the polar cap region (> 81 MLAT) as measured by Swarm. **b** Corresponding variability of plasma in terms of RODI and ROTI. Figure from Jin et al. (2019)

winter season, while in the southern hemisphere this pattern is still observed, but the seasonal variations are less pronounced (Spicher et al. 2017). This can be attributed to a different illumination in the southern hemisphere due to the offset of the magnetic pole and thus different background conditions. However, other results have also been obtained based on different definitions of plasma density enhancements and reporting that the ionospheric plasma in the southern hemisphere is more structured at kilometre-scales than in the northern hemisphere (Chartier et al. 2018; Noja et al. 2013). Climatology studies with the Swarm data reveal that the background plasma density Ne and TEC of the topside ionosphere follow clear seasonal variations, and also correlate with the solar activity (Jin et al. 2019). In Fig. 21(a) (from Jin et al. 2019) the seasonal variations in the Ne and TEC in the polar cap region (> 81° MLAT) as measured by Swarm are shown. In Fig. 21(b) Jin et al. (2019) have plotted the corresponding variability of plasma in terms of RODI and ROTI, where RODI is defined as the Rate Of change Density Index and ROTI is defined as the Rate Of the change of TEC Index. However, the variability of plasma in the polar cap, which is assessed in terms of the standard deviation of RODI and ROTI, is consistently larger in the southern hemisphere. The same is valid for large-scale density gradients (Jin and Xiong 2020). Again, the offset of the geomagnetic pole and the geometry of the magnetic field in the southern hemisphere can lead to a larger intake of plasma density into the polar ionosphere and larger structuring at all seasons. In general, the distribution of irregularities depends on the geomagnetic conditions, and in particular on the orientations of the IMF Bz and By components.

3.3.4 SuperDARN

The space science accomplished by SuperDARN (Chisham et al. 2007; Lester 2013, Nishitani et al. 2019) is formidable, with well over 600 published papers in research journals. It is therefore not possible to cover all aspects of scientific achievements, but the aim here is to highlight its significant contribution to space research and, in particular, to the investigation on the magnetosphere-ionosphere coupling.

After 30 h of quiet solar wind conditions, Walker et al. (1998) presented observations of flow bursts, exceeding 2000 ms^{-1} (electric fields > 50 mV m^{-1}), by combining Doppler velocity components from the SANAE (SAN) and Halley (HAL) radars, whose fields of view are shown in Fig. 4(b). They occurred quasi-periodically for more than two hours on the nightside magnetosphere. This initiated much research into this area. Events with similar characteristics to this, lately became to be known as TRINNI (Tail Reconnection IMF North Non-substorm Interval) events, were interpreted as sporadic energy releases from re-configuration of a 'twisted' magnetotail.

Using SuperDARN observations, fundamental solar wind-magnetosphere coupling phenomena occurring at the dayside magnetopause have been unveiled as well. Neudegg et al. (1999) observed for the first time the "flow channels'' due to newly-opened cusp field lines. Moreover, numerous studies based on SuperDARN data permitted to estimate the reconnection rate at the dayside magnetopause and in the geomagnetic tail for extended time intervals (e.g. Milan et al. 2003 and Pinnock et al. 2003). SuperDARN measurements have also been fundamental for the study of the effects of the reconnection occurring poleward of the cusps during northward IMF intervals (Huang et al. 2000; Imber et al. 2006; Marcucci et al. 2008).

The spectral width parameter of the Halley radar (and magnetically conjugate Goose Bay radar) was employed to identify the polar cusp and Lower Latitude Boundary Layer

regions of the magnetosphere (Baker et al. 1995). This was the first ground-based observation to provide useful inter-calibration of such regions with the DMSP satellite. This type of observation provides valuable inputs to the Geospace Environment Modelling (GEM) program.

SuperDARN has proven to be a very successful tool for observing ULF magnetohydrodynamic waves with periods in the 45–600 s range. Their direct observation in the ionosphere allows for their morphology to be determined, unlike magnetometers that are limited in this regard as they receive an integrated signal. This point is well demonstrated in Bland and McDonald (2016) who calculated the polarisation vector of ULF waves in the ionosphere using the South Pole Station (SPS) and Dome C East (DCE) radars (see Fig. 4(b) for fields of view). Such waves are an important means of energy transfer into and within the magnetosphere. Stephenson and Walker (2002) were the first to demonstrate that coherent oscillations in the solar wind were a candidate for exciting a field line resonance observed by the SANAE (SAN) radar. The Field Line Resonance was estimated to deposit more than 10 MW into the ionosphere in the form of Joule heating.

As meteors move through the Earth's upper atmosphere, they create ionisation trails, which are scattering targets for SuperDARN in their near ranges. Jenkins and Jarvis (1999) used data from the Halley radar (HAL) to derive ground-based observations of mesospheric winds above Antarctica. Another near-range scattering target is unusual echoes that occur between 180 and 315 km range (80–100 km altitude) with different characteristics to those produced by meteors. They have become known as Polar Mesospheric Summer Echoes whose targets are ice crystals. They were first observed by the Syowa East radar (SYE) by Ogawa et al. (2002). The Antarctic summer mesosphere is the coldest place on Earth and these ice clouds provide an important indicator in tracking climate change.

Sky noise (atmospheric noise) is routinely recorded by SuperDARN radars and for many years this was regarded as metadata. However, Bland et al. (2018) have successfully shown that this parameter can be used to track Solar Proton Events (SPEs) as well as Energetic Electron Precipitation (EEP) events (Bland et al. 2019), as it is significantly attenuated during such periods (Fig. 22). This is an important result, as understanding the effect of EPPs on the ionosphere is critical for predicting communication quality in the modern world.

SuperDARN observations have been used extensively to conduct research on the ion-neutral coupling, permitting a deeper insight into the link between the ionosphere and the thermosphere, see Billett and McWilliams (2020) for an overview of SuperDARN related results on this topic.

In their work of comparison of SuperDARN peak electron density estimates with measurements from the ionosonde and the incoherent scatter radar in Canada from 2008 to 2017, Koustov et al. (2020) concluded that the SuperDARN electron density estimates are a valuable resource for their use in statistical studies, such as those focused on seasonal and solar cycle effects.

3.4 Magnetic Perturbation Events Relevant to Geomagnetically Induced Currents

The impact of extreme space weather events on human technological systems has received growing attention worldwide in the past two decades. The magnetic perturbation events (MPEs), that cause geomagnetically induced currents (GICs) that can damage electrical power grids and pipelines, mainly (but not only, see, e.g., Piersanti and Carter 2020) originate in ionospheric currents in the auroral zone, which expands equatorward during major geomagnetic storms, thus putting at risk regions at middle and even lower latitudes.
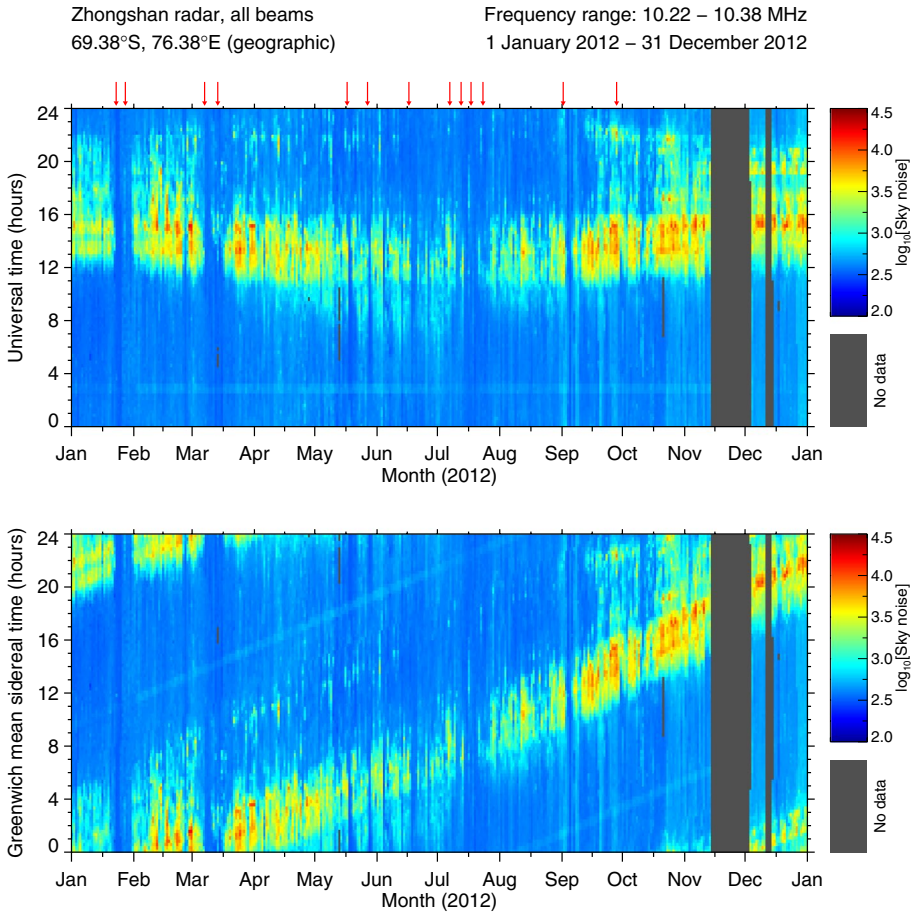
Zhongshan radar, all beams
69.38°S, 76.38°E (geographic)

Frequency range: 10.22 – 10.38 MHz
1 January 2012 – 31 December 2012

Fig. 22 Background noise for the year 2012 as recorded by the Zhongshan (ZHO) radar. Red arrows indicate the onset of Solar Proton Events characterised by vertical blue lines indicating the absorption of sky-noise (from Bland et al. 2018)

However, dangerously large MPEs have been shown to occur mostly at higher latitudes, where the auroral zone is more commonly situated, and the poorly understood physical mechanisms that produce MPEs and GICs appear to be the same under expanded or contracted auroral oval conditions. A number of large statistical and event studies of MPEs (and in some cases the associated GICs) using the IMAGE array in Scandinavia (ranging, for example, from Viljanen, 1997 and Viljanen and Tanskanen, 2011 to Belakhovsky et al. 2019 and Dimmock et al. 2020) have now been extended to Arctic Canada (Engebretson et al. 2021 and Weygand et al. 2021). The latter study applied spherical elementary current systems (SECS) analysis and included all-sky imager data in statistical and case studies of MPEs in order to clarify their association with localised and/or extended ionospheric and field-aligned currents. A conjugate study using both Arctic and Antarctic data by Engebretson et al. (2020) showed that large MPEs can occur in magnetically conjugate locations at these high and very high latitudes, and based on their relative amplitude and ionospheric

conductivity provided evidence that their generation follows a magnetospheric current generator model rather than a voltage generator model.

4 Ionospheric Weather

The part of our scientific community that works on studies of the lower atmosphere deals mainly with the long-term variation in its constituents. Contrarily, the community investigating the upper atmosphere, which is strongly affected by geospace conditions, deals both with long-term trends and with short-term events that have durations from minutes to several days. This section addresses the latter community through a focus on ionospheric weather through the review of case studies complemented by new results.

The investigation of the ionospheric behaviour during strong geomagnetic storms has improved our knowledge about the upper atmosphere responses to space weather events, leading to a deeper knowledge of the electrodynamic processes in the ionosphere/thermosphere from low to high latitudes at different longitudinal sectors.

The ionospheric dynamics is driven by coupling processes involving the solar wind, the IMF and the magnetosphere, which results in electric fields, neutral winds and composition changes. The induced electric fields are mapped along magnetic field lines to the high latitude ionosphere, but they can also penetrate the auroral latitudes and impact the low and mid-latitude ionosphere, in the form of prompt penetration electric fields (PPEFs). The PPEFs were first identified during substorms (Nishida 1968), but their effect has been observed as dominant during the first hours of the main phase of geomagnetic storms (Astafyeva et al. 2015, 2016; Correia et al. 2017; Huang et al. 2005; Macho et al. 2020; Mannucci et al. 2008; Sahai et al. 2004; Shreedevi et al. 2016, 2017; Spiro et al. 1988; Tsurutani et al. 2004, 2008;). The PPEFs generated during strong geomagnetic storms can lift the dayside equatorial plasma to higher altitudes than the normal Equatorial Ionospheric Anomaly (EIA), resulting in the crests being pushed to mid-latitudes (Tsurutani et al, 2008). The precipitation of energetic particles into the thermosphere at high latitudes generates intense electric currents in the ionosphere (Buonsanto and Witasse 1999), which heat the auroral zone, changing its composition and driving large-scale neutral winds (Buonsanto and Witasse 1999; Danilov and Lastovicka 2001; Fuller-Rowell et al. 1994). The combination of these processes results in a large-scale ionospheric plasma density increase redistribution from mid-latitude or even the equator to high latitudes, and at dusk, the plasma of the EIA crests can contribute to the plumes of Storm Enhanced Density (SED, Huba et al. 2017; Sandel et al. 2001). These plumes can be transported through the dayside cusp and across the polar cap into the night side where they form structures called Tongues Of Ionisation (TOI, Foster et al. 2005) or polar cap patches (Foster et al. 2021; Zou et al. 2021a).

Despite several milestones that have been reached in high latitude ionospheric studies, there are still open questions, e.g. how variable the ionospheric storm-time response is, how it is driven, and its strong longitudinal and latitudinal asymmetries, just to mention a few, that would benefit from a multi-instrument approach. After the International Polar Year (IPY 2007–2008), the multi-instrument probing of the ionosphere from low to high latitudes was consolidated (e.g. Alfonsi et al. 2008a; Zou et al. 2014, 2017a, 2021b). Many different techniques are now available, particularly at high latitudes, in both hemispheres, where the ionosphere contains the footprints of processes that have their origin in the interplanetary space. A multidisciplinary approach is required for the advancement of

Table 4 Dates of geomagnetic storms identifying the case studies

Event
29–30 October 2003
26 September 2011
25 January 2013
22 June 2015
17–18 March 2013
17–18 March 2015
25 December 2015
16–18 July 2017
7–9 September 2017
11 May 2019

the current knowledge: when a geoeffective solar perturbation occurs, the succession of the events in the near-Earth space needs to be monitored by different sensors to improve the physical understanding and modelling of the response of the near-Earth space in response to natural perturbations.

In this section, we discuss ten geomagnetically disturbed periods (Table 4) by using a radio-based multi-instrument approach, sometimes supported by ancillary measurements that contributed to the understanding of the physical mechanisms responsible for extreme events in the polar upper atmosphere during solar cycles 23 and 24. In some cases, the survey of the existing literature is corroborated by new results. For each selected event the geospace conditions and the magnetic activity are characterised by investigating the Interplanetary Magnetic Field components (Bx, By, Bz) and its total intensity (Btot), the solar wind velocity (v) and proton density (ρp), the geomagnetic indices SYM-H (Wanliss and Showalter, 2006 and references therein), AE (World Data Center for Geomagnetism, 2015; Perrone and De Franceschi, 1998) and Polar Cap Index (PCI) for both North (PCN) and Southern Hemisphere (PCS) (Stauning, 2013; Perrone and De Franceschi, 1998). The IMF components are measured every second by the Magnetic Field Experiment (MAG) (Smith et al. 1998) onboard the Advanced Composition Explorer (ACE) satellite orbiting at the first Lagrangian point (L1) point. For our purposes, we use the 4-Minute Level-2 data, the Geocentric Solar Magnetospheric (GSM) coordinate system, provided by the Coordinated Data Analysis (CDA) Web portal of NASA (https://cdaweb.gsfc.nasa.gov/). For the solar wind speed and proton density measurements, we consider the Level-2 data (sampling rate: 64 s) provided by the Solar Wind Electron, Proton, and Alpha Monitor (SWEPAM) (McComas et al. 1998), again onboard the ACE spacecraft and available through CDA Web.

4.1 The Halloween Storms of October 2003

During the descending phase of the 23rd solar cycle, two geomagnetic superstorms occurred during 29–30 October 2003. Their storm time effects impacted the ionosphere globally, with characteristics depending on the latitude and local time at different sectors. The geomagnetic activity during this period was complex due to the superposition of three strong fast ring current injections with the |SYM-H| peak reaching 400 nT and the Auroral Electrojet index, AE, exceeding 4000 nT (Fig. 23).
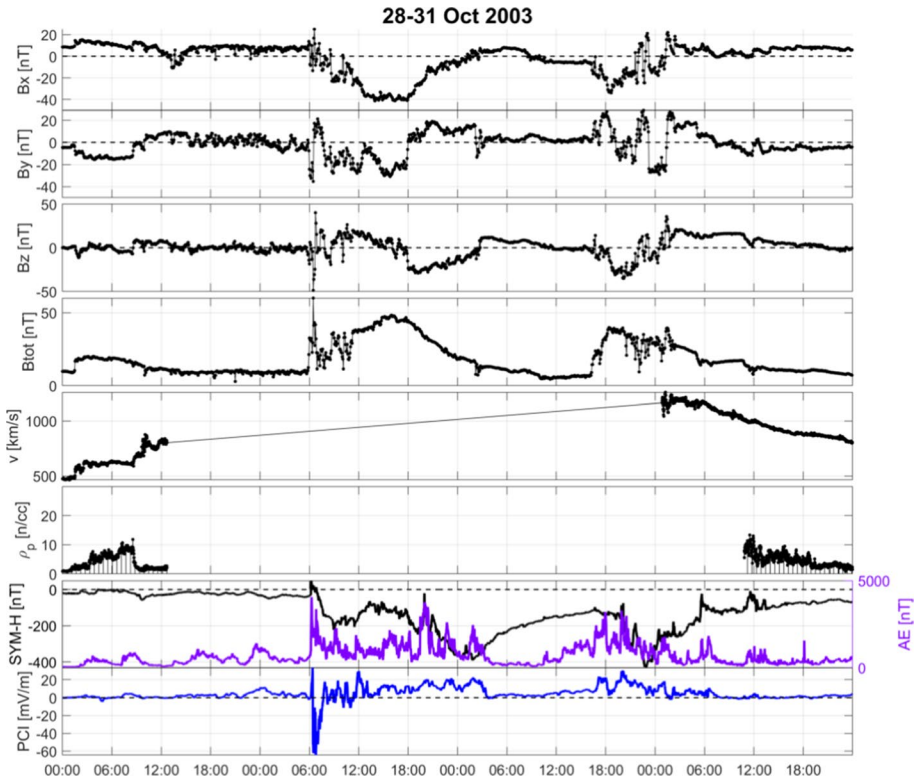
28-31 Oct 2003

Fig. 23 Summary of the geospace characteristics during the events of 28–31 October 2003. From the top to the bottom they are the following: The Interplanetary Magnetic Field components (Bx, By, Bz, Btot), the solar wind speed (v) and proton density (ρ_p), the geomagnetic indices SYM-H, AE and PCI (only PCN available), the last two mostly related to auroral and polar cap conditions. The data gaps were due to outages on the observing satellites during these periods

Investigation of GPS-TEC maps done by Ding et al. (2007) using stations over North America showed three large-scale travelling ionospheric disturbances (LSTIDs) during these superstorms. The first two occurred at local midnight, just after the onset of the big storm on 29 October, and the third one at noon during the expansion phase of the next substorm on 30 October (Ding et al. 2007). They attributed the LSTIDs that occurred on 29 October to the auroral westward electrojet. These storms produced a very strong global ULF activity during their recovery phase, with Pc5 events observed simultaneously at all local time sectors with larger amplitude at prenoon or noon hours, of which the possible cause was suggested to be the boundary layer instability (Potapov et al. 2006). Mitchell et al. (2005) demonstrated that the high TEC values observed over the Svalbard archipelago originated from North America, highlighting the presence of sharp density gradients responsible for the observed ionospheric scintillations. A deeper study of the same event identified the polar cap patches as possibly responsible for scintillation occurrence (De Franceschi et al. 2008).

Under conditions where empirical models are not adequate, like the Halloween storm in 2003, the use of EISCAT, in combination with ionospheric models, was revealed to be very effective to provide constraints on the neutral composition of the

atmosphere. Enell et al. (2008) modelled the response of the lower ionosphere to the X class solar flare that occurred on 28 October 2003. The chemical response to the X-ray ionisation was studied with the time-dependent version of the Sodankylä Ion Chemistry model (Turunen et al. 1996; Verronen 2006). The modelled electron density profile at the peak of the event was then brought into agreement with the corresponding EISCAT VHF D- and E-layer ionospheric profiles, retrieved using the theory of Fukuyama and Kofman (1980) for the negative ion region. This was accomplished by scaling the nitric oxide (NO) profile since NO is the main ionisable component of the lower ionosphere.

4.2 The Prompt Penetration Electric Fields (PPEFs) and Disturbance Dynamo Processes in September 2011 and June 2015

The investigations of ionospheric storms have shown that during the first few hours of a geomagnetic storm, the PPEF penetrates both the dayside and nightside ionosphere (Astafyeva et al. 2016; Correia et al. 2017; Mansilla 2018). The normal eastward dawn-to-dusk electric field on the dayside is reinforced by the PPEF, which lifts the equatorial ionospheric plasma to higher altitudes and latitudes, forming the dayside ionospheric superfountain (DIS) effect (Tsurutani et al. 2004). The DIS results in an overall dayside low-latitude ionospheric electron density increase, with EIA crests reaching mid-latitudes. The positive storm at midlatitudes is dominated by the PPEF during the early main phase and the disturbance dynamo processes later. On the nightside during the main phase of the storm, from middle to high latitudes the westward dawn-to-dusk electric fields are dominated by the dynamo disturbance, causing a downward plasma drift, which increases the recombination process and decreases the electron density. This mechanism was identified in the geomagnetic storms that occurred on 26 September 2011 (Correia et al. 2017), and 22–23 June 2015 (Astafyeva et al. 2016; Mansilla 2018). The studies showed that during these storms the ionosphere is highly structured and dynamic as a consequence of solar wind coupling with the magnetosphere-ionosphere system, suggesting a combination of effects associated with PPEFs and disturbance dynamo processes. The investigations have been carried out through a complementary analysis of data acquired by the ionosondes, GNSS receivers and SuperDARN radars that were used to evaluate the electron density changes and the modifications of the ionospheric plasma dynamics induced by the storm.

The 26 September 2011 storm was triggered by the arrival of the interplanetary shock (IP) produced by a ICME, which occurred in association with an M7 long-duration X-ray event. This disturbance resulted in the geomagnetic storm (G2 level) on 26–27 September with |SYM-H| about 100 nT on 26 September (Fig. 24). The interplanetary shock arrived on 26 September 2011 at 12:40 UT when a sudden change in parameters was observed resulting in a sudden impulse (SI). Sudden variations were observed in the solar wind and interplanetary magnetic field (IMF) parameters (Fig. 24) with increases in the solar wind speed and proton density, and with the enhancement of total IMF (Btot) and the beginning of fast fluctuations in the IMF components Bz, By and Bx. The Polar Cap indices for the Northern and Southern Hemisphere (PCN/PCS) showed intensification at 12:40, ~17:00, and ~20:00 UT in association with Sudden Storm Commencement (SSC) and the two peaks in AE, respectively.

During the September 2011 event, SED (Foster, 1993) were observed at middle latitudes in the American (dayside) sector. Zhang et al. (2013) reported a direct observation of the evolution of polar cap ionisation patches in the Artic. The SED signatures were visible
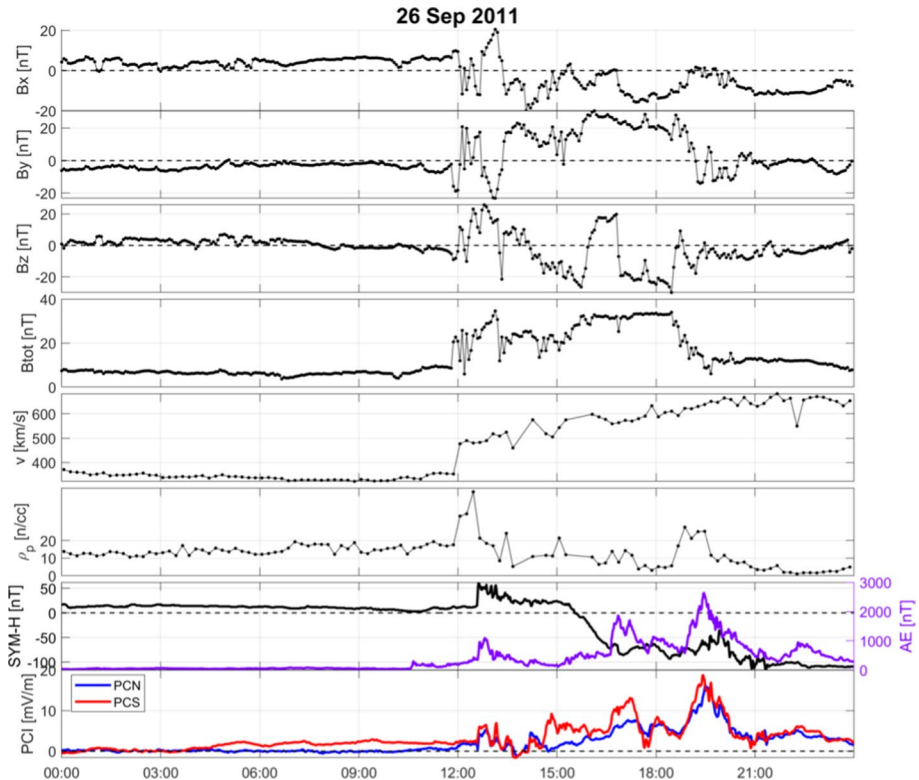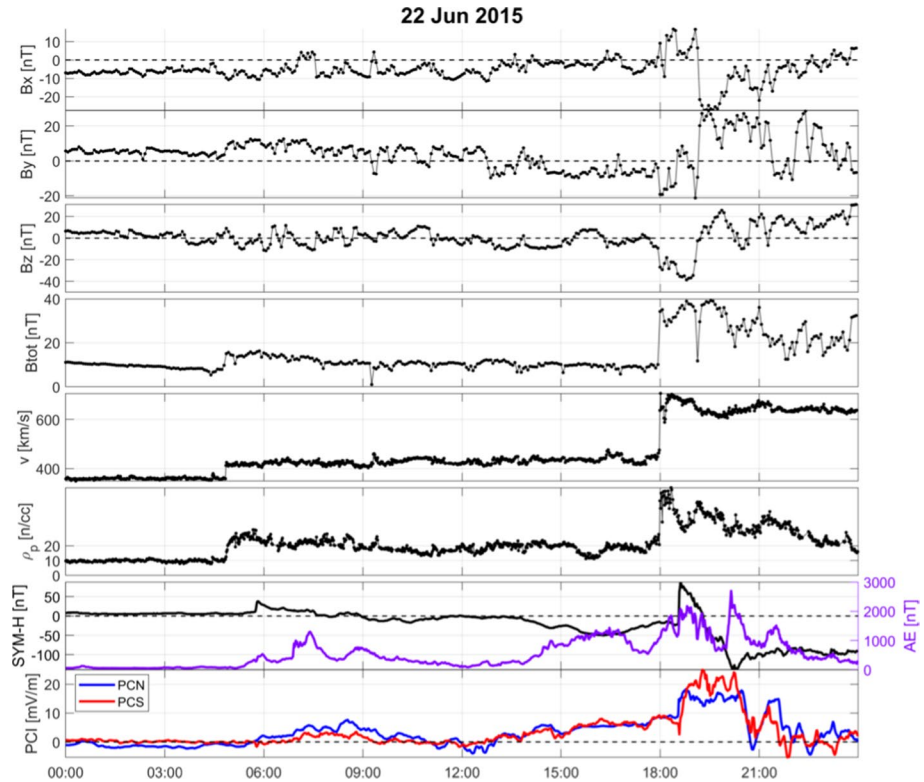
Fig. 24 Summary of the geospace characteristics during the event of 26 September 2011. From the top to the bottom they are the following: The Interplanetary Magnetic Field components (Bx, By, Bz, Btot), the solar wind speed (v) and proton density (ρ_p), the geomagnetic indices SymH, AE and PCI, the last two mostly related to auroral and polar cap conditions. PCN and PCS refer to the Polar Cap Index (PCI) at Northern (N) and Southern (S) hemispheres, respectively

in the Antarctic American sector, with an evident uplift of the F2 ionospheric layer. In the Australian sector, contrarily, the storm caused a decrease in the electron density for the quiet day and an interesting increase in TEC at the Mario Zucchelli Station in Antarctica. The latter, together with evidence from SuperDARN backscattering and scintillations, is interpreted as proof of the formation of TOI from SED plumes formed at middle latitudes that entered the polar cap passing through the cusp (Correia et al. 2017). Contrary to the TOI occurrence in the southern ionosphere, the same event in the northern hemisphere did not show evidence of TOI formation (Thomas et al. 2013). This event has been also studied to assess the feasibility of ionospheric nowcasting and forecasting. Indeed, an exercise of GNSS data assimilation into a physics-based model has demonstrated the improved capability of nowcasting the ionospheric response to the September 2011 storm at European high latitudes (Solomentsev et al. 2015). Chen et al (2016) demonstrated an improvement, at global scale including high latitudes, of ionospheric forecasting for this storm by assimilating the GNSS TEC observations into the thermosphere-ionosphere-electrodynamics general circulation model (TIE-GCM). The data acquired during the storm that occurred on 26 September 2011 have also been used to demonstrate how the use of COSMIC Radio
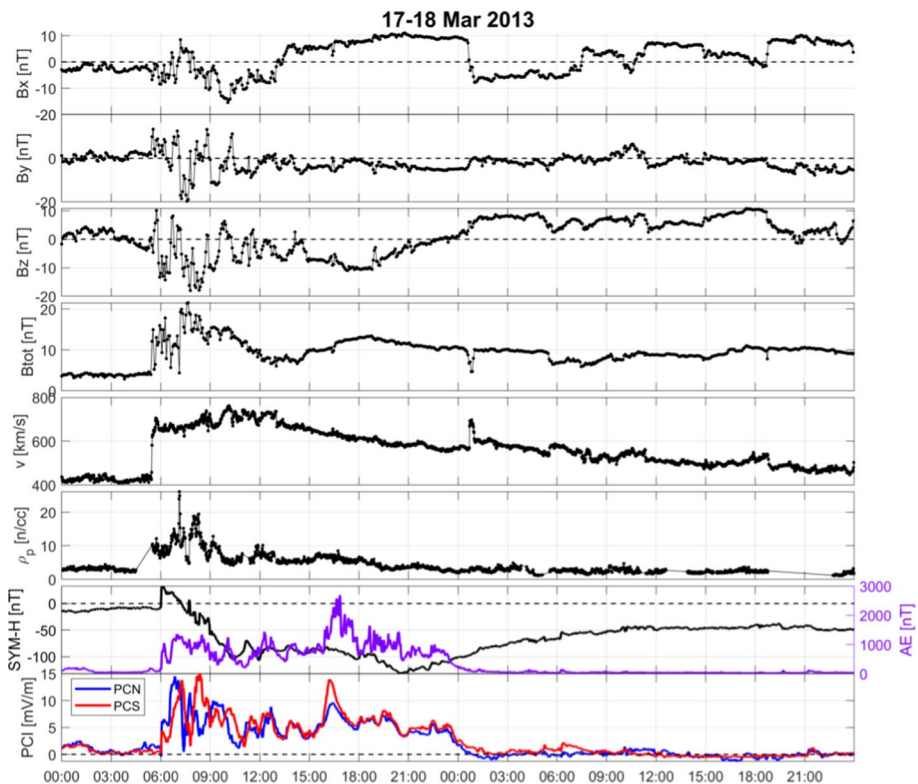
Fig. 25 Summary of the geospace characteristics during the event of 22 June 2015. From the top to the bottom they are the following: The Interplanetary Magnetic Field components (Bx, By, Bz, Btot), the solar wind speed (v) and proton density (ρ_p), the geomagnetic indices SYM-H, AE and PCI, the last two mostly related to auroral and polar cap conditions. PCN and PCS refer to the Polar Cap Index (PCI) at Northern (N) and Southern (S) hemispheres, respectively

Occultation (RO) profiles in GPS tomography helps to improve the vertical imaging accuracy, which is validated by ionosondes and ISR scans (Yin and Mitchell 2014).

June 2015 was characterised by several IPs that affect the near-Earth environment. Specifically, the responses of the geomagnetic field to the IPs that hit the Earth at 05:02 UT and 18:07 UT on June 22, (labelled as IP2 and IP3 in Fig. 23 of Piersanti et al. 2018) were significantly different. The former did not have a significant geospace effect, while the latter resulted in SYM-H dropping to below −100 nT (Fig. 25), as a consequence of the solar wind velocity and the proton density suddenly increased. Total B (Btot) increased and related components sharply reacted with a negative Bz (peak at about −40 nT), lasting a couple of hours, followed by a long duration positive and pulsating IMF Bz. A global investigation of the TEC variations associated with this intense geomagnetic storm was done by Mansilla (2018), whose results show a considerable interhemispheric asymmetry in the ionospheric response at low and mid-latitudes during the evolution of the main phase of the storm. Yang et al. (2020a) processed over 5500 GPS/GNSS receivers precise point positioning (PPP) solutions worldwide to examine the impact of the ionospheric responses during this storm. Their work found that up to 70% of the high latitude receivers experienced degraded position solutions and that the

Southern hemisphere impact was more severe. A regional study of the same storm has been performed by D'Angelo et al. (2018a) by analysing data from auroral, cusp and polar cap GNSS stations located in Antarctica and the Arctic. The work, supported by SuperDARN measurements and by an in-depth description of the ionosphere-magnetosphere coupling derived from in-situ and ground-based data, revealed similarity in the behaviour of the ionospheric response at high latitudes of the two hemispheres. Nevertheless, the same authors reported that their conclusions are based on a partial picture of the ionospheric scintillations because of the lack of data from auroral latitudes. At these latitudes, Cherniak and Zakharenkova (2017) reported large plasma density fluctuations over both hemispheres. The impact of this storm was also investigated in the South American sector, from low to high latitudes, by Macho et al. (2020). The work based on GNSS and ionosonde data, evidenced the expansion of the crest of EIA to higher latitudes, due to PPEF process in the daytime sector during the beginning of the main phase storm. After few hours, in the end of the main phase, the disturbance dynamo electric field becomes dominant, and TEC increases were observed from high to middle latitudes, due to the dusk effect at the end of the day.

Fig. 26 Summary of the geospace characteristics during the event of 17–18 March 2013. From the top to the bottom they are the following: The Interplanetary Magnetic Field components (Bx, By, Bz, Btot), the solar wind speed (v) and proton density (ρ_p), the geomagnetic indices SYM-H, AE and PCI, the last two mostly related to auroral and polar cap conditions. PCN and PCS refer to the Polar Cap Index (PCI) at Northern (N) and Southern (S) hemispheres, respectively
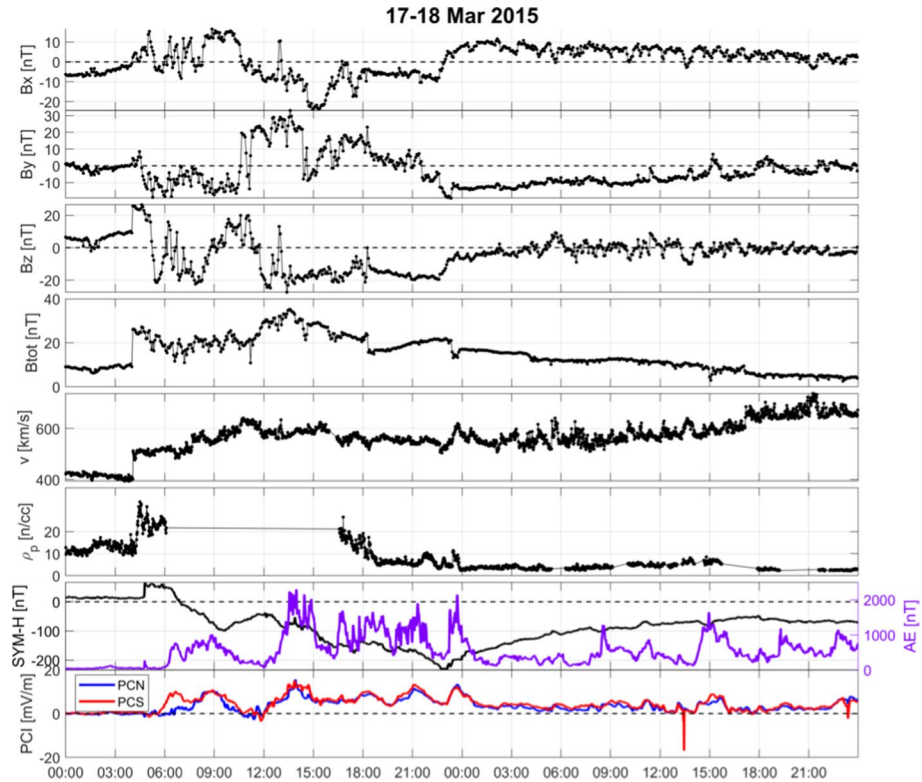
Fig. 27 Summary of the geospace characteristics during the event of 17–18 March 2015. From the top to the bottom they are plotted, vs UT: The Interplanetary Magnetic Field components (Bx, By, Bz, Btot), the solar wind speed (v) and proton density (ρ_p), the geomagnetic indices SYM-H, AE and PCI, the last two mostly related to auroral and polar cap conditions. PCN and PCS refer to the Polar Cap Index (PCI) at Northern (N) and Southern (S) hemispheres, respectively

4.3 ICMEs and HSS Driven Storms in March 2013, 2015, July and September 2017

Intense geomagnetic storms are often caused by combined impacts of ICMEs and co-rotating interaction regions (CIR) ahead of high-speed streams (HSS) from coronal holes. Such geo-effective configuration in the solar wind resulted in geomagnetic storms of 17–18 March 2013 and 2015, 16–18 July and 7–9 September 2017.

The storm that occurred on 17–18 March 2013 was triggered by an Earth-directed ICME that occurred on 15 March. The SSC occurred at ~06:00 universal time (UT) on 17 March, and SYM-H reached a minimum of about −130 nT around 21:00 UT on 17 March (Fig. 26). As a result, the substorm intensity as measured by the AE index was persistently more than 500 nT on 17 March from 06 UT onwards and reached the maximum AE = 2240 nT on 16:39 UT, in response to the PC rise to 11 mV/m.

Foster et al. (2014) reported quantitative simultaneous evidence of plasmasphere erosion on 17 March 2013, that carried cold dense plasma of ionospheric origin towards the dayside magnetopause. They used GPS TEC data combined with Defense Meteorological Satellite Program (DMSP) and Millstone Hill Radar measurements. Examining

north polar TEC maps, the authors investigated the variability of the TOI, observing patches of enhanced TEC reaching cusp and the polar cap. A global assessment of the ionospheric electron density during the event was done by Yue et al. (2016) assimilating ground and LEO satellite-based TEC into an algorithm derived from NCAR Global atmospheric, oceanic, and land field reanalysis. The authors reported the magnetic conjugacy of SED and TOI at the high latitudes of both hemispheres. In addition, multi-instrument observations from mid to high latitudes were used to study the magnetosphere-ionosphere coupling processes during this storm by Lyons et al. (2016). They identified multiple structured polar cap patches in the nightside aurora zone transported by equatorward moving fast plasma flows.

The March 2015 storm involved a two-step development, the first driven by the southward IMF in the compressed sheath region, and the second driven by the southward IMF in the magnetic cloud (Kamide and Kusano, 2015; Kataoka et al. 2015). In Fig. 27, the SYM-H profile clearly describes the occurrence of a two-step main phase storm during which IMF Bz was oscillating between positive and negative values with a constant increase in solar wind velocity and proton density. The AE index showed substorm signatures while PC indices reached four peaks at about 14:00, 18:00, 21:00, and 23:00 UT on 17 March indicating substorm conditions (Astafyeva et al 2015).

Liu et al. (2016) compared the performance of the TIE-GCM model (Roble et al. 1988) to TEC mapping from ground-based GPS stations to evaluate the ionospheric response to the March 2013 and 2015 storms at high latitudes. The two events resulted in negative ionospheric storms, presenting SED and TOI features. Their work testified to the limitation of the TIE-GCM model not being capable of capturing an electron density "hole" revealed by GPS data.

The March 2015 superstorm impacted the high-latitude ionosphere leading to considerable dynamics of ionospheric irregularities observed using GNSS data (Cherniak et al. 2015; Cherniak and Zakharenkova 2016, 2017) and revealing a relation between the GNSS phase scintillation and auroral electrojet currents (Jacobsen and Andalsvik, 2016; Prikryl et al. 2016). Cherniak and Zakharenkova (2017) highlighted the significant improvement in the global/regional GPS networks at high latitudes compared to what was available during the previous solar cycle. The exploitation of such networks, not specifically designed to probe the ionosphere, can provide results that are crucial to derive a regional picture of ionospheric perturbed conditions and their relation to a global representation of the plasma environment. Indeed, the work by Cherniak and Zarenkova (2016) revealed the formation and the evolution of SED and TOI structures from plasma density gradients identified by GPS data at high latitudes, consistent with observations from GPS onboard five LEO satellites. The authors reported interhemispheric differences possibly related to IMF orientation. This is confirmed by D'Angelo et al. (2018b), that, using in-situ satellite data (from POES and Swarm constellations) and ground-based data from SuperDARN radars and scintillation monitors, showed more intense particle precipitation in the southern polar cap with a consequent higher level of scintillations in Antarctica. Yao et al. (2016) reported the occurrence of three TIDs occurring during the main phase of the storm and first observed at the high latitudes of both hemispheres. The authors concluded that the TIDs were triggered by Atmospheric Gravity Waves (AGW) excited by auroral substorms.

Figure 28 shows the TEC maps of the southern polar region at selected times during the main phase of the St. Patrick's day storm of 2015 (Shreedevi et al. 2020). The TEC maps are overlaid with the SuperDARN convection pattern to facilitate the comparison of the changes in the TEC along the path of convection. At 1600 UT, no significant enhancements are seen in the TEC in the southern polar cap. During the period 17:00–17:30 UT, a region
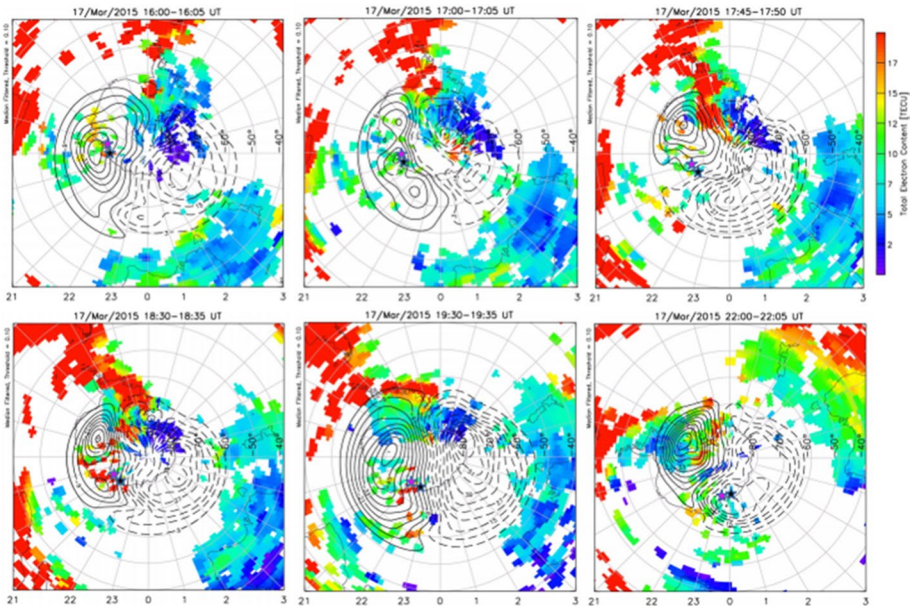
Fig. 28 Panels **a**–**f** (from top-left to bottom-right) show the TEC in the southern hemisphere at selected times (1600 UT, 1700 UT, 1745 UT, 1830 UT, 1930 UT and 2200 UT) on 17 March 2015. The SuperD-ARN convection pattern is overlaid on the TEC maps to facilitate comparison of the changes in the TEC along the path of convection. The location of Bharati and Davis stations are marked on the maps using pink and black stars, respectively (from Shreedevi et al. 2020)
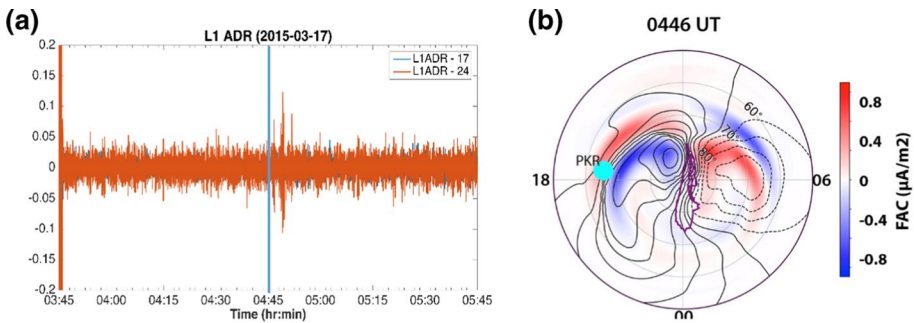

Fig. 29 **a** Phase variations (in radians) highlighting a scintillation observed by a receiver at Poker Flat during the storm sudden commencement; **b** FAC distributions from the BATSRUS MHD model (Zou et al. 2017b)

of enhanced TEC is seen to form at the magnetic noon sector. This region of enhanced TEC can be seen to extend into the polar cap along the path of convection at later intervals of time, highlighting the TOI formation. At the Bharati and Davis stations (pink and black stars, respectively) in the eastern part of Antarctica, large enhancements in the TEC were observed during the period 18:30–19:30 UT (magnetic midnight sector) owing to the passage of the TOI. Later on, the TOI is seen to break into patches as they traverse through the polar cap in response to the strengthening of ionospheric convection. Shreedevi et al.

([2020](#)) have also shown that the enhanced ionospheric convection and associated formation of polar cap patches gave rise to intense phase scintillations in the polar cap ionosphere (at Bharati) during the St. Patrick's day storm of 2015.

The EDAS network, established by the Satellite Navigation and Sensing Lab at the University of Colorado, Boulder, to study the impact of geomagnetic disturbances on the auroral ionosphere, has recorded scintillation events at Poker Flat (Alaska) (Fig. 29a). Zou et al. ([2017b](#)) reported the impact of the 17 March 2015 storm highlighting changes in ionospheric plasma characteristics (e.g. convection flow, plasma temperatures) during the sudden commencement observed by the Poker Flat incoherent scatter radar and simulated by using the University of Michigan Space Weather Modelling Framework (SWMF). The simulated large-scale field-aligned current (FAC) distribution and convection flow pattern have been validated through comparison with observations and are reproduced in Fig. 29b for convenience. Poker Flat is indicated as a cyan dot in this plot. The red and blue contours represent the upward and downward FACs. As can be seen at 04:46 UT, i.e. 1 min after the shock impact, the shock-induced preliminary impulse FACs (the pair at higher latitude) and the main impulse FACs (the pair at lower latitude) covered nearly the whole day-side auroral and high latitude regions. The FACs perturbations crossed Poker Flat in about three minutes. Figure 29a shows a short-lived phase scintillation during this storm sudden commencement observed by the EDAS receiver located at Poker Flat. The enhanced ADR (Accumulate Doppler Range) was observed starting at 04:45 UT and lasted for about three minutes. This unique data and model combination reveals that the short-lived scintillation is due to the shock-induced FACs moving across Poker Flat. This type of impulsive phase variation is better captured by the EDAS high temporal resolution measurements.
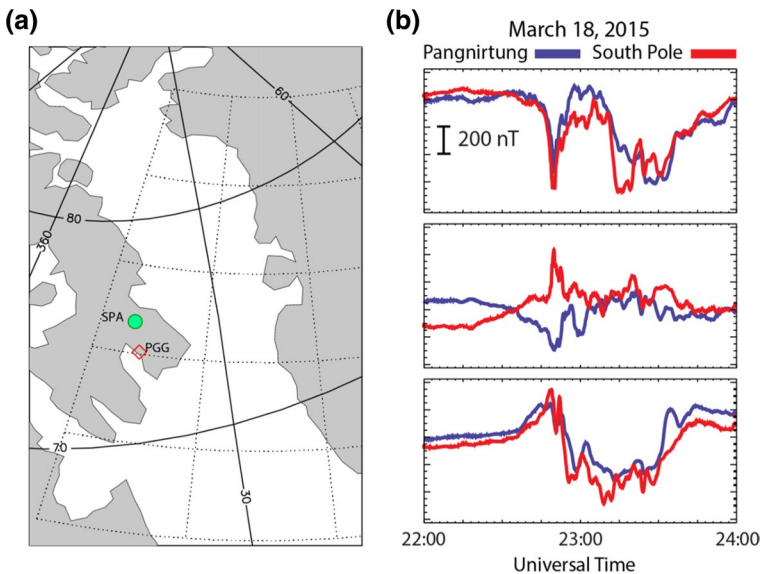
Fig. 30 a Map showing the location of Pangnirtung (PGG), Baffin Island, Canada, and the mapped magnetic conjugate location of South Pole Station (SPA), Antarctica; **b** two-hour excerpts from daily magnetograms for March 18, 2015 from Pangnirtung, Canada and South Pole Station, Antarctica. Component data are shown in local magnetic coordinates (from top to bottom Bx N-S, By E-W, and Bz vertical)

Figure 30 shows an example of the large, impulsive perturbation that peaked near 22:47 UT on March 18, 2015 at Pangnirtung, Canada (CGM Lat 73.2°, CGM Lon 19.8°) and its near magnetically conjugate location, South Pole Station, Antarctica (CGM Lat −74.5°, CGM Lon 18.7°). Very similar magnetic perturbations appeared at both stations, with ~ 5 min duration, ~ -600 nT ΔBx, and derivative amplitudes of 8.3 nT/s at Pangnirtung and 10.1 nT/s at South Pole. The relative orientations of the Bx and By perturbations most likely reflect the hemispheric difference in the circular Hall current flow around a localised field-aligned current (FAC), counter-clockwise in the northern hemisphere and clockwise in the southern hemisphere. The studies of MPEs cited in 2.4 have shown that the occurrence of very large MPEs at these high latitudes is not limited to the most intense storm time intervals. The magnetic field at these two stations was significantly disturbed during both March 17 and 18, but by far the largest MPEs occurred near the end of March 18. This event is also evident in the bottom panel of Fig. 27, reflecting a similar but weaker perturbation that appeared slightly later at Thule (not shown), corresponding to the PCN index.

The geomagnetic storm of 16–18 July 2017 was caused by a ICME ahead of a high-speed plasma stream from a coronal hole. The ICME (Richardson and Cane, 2010) showed some evidence of a rotation in field direction, but lacked other characteristics of a magnetic
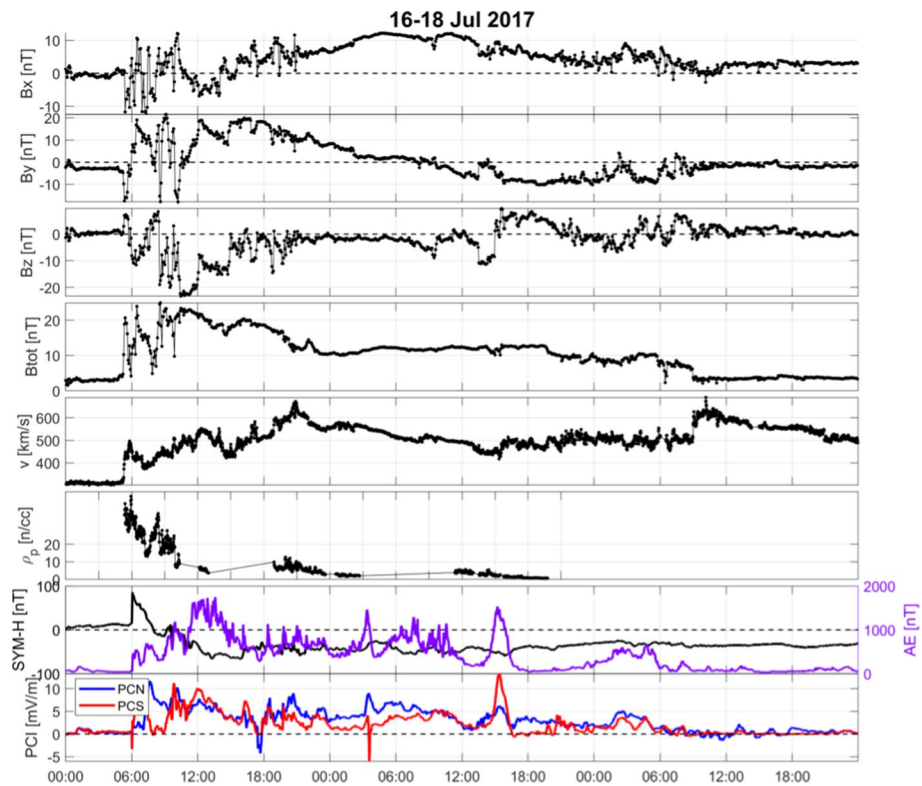
Fig. 31 Summary of the geospace characteristics during the event of 16–18 July 2017. From the top to the bottom they are plotted, vs UT: The Interplanetary Magnetic Field components (Bx, By, Bz, from top to bottom) and Btot, the solar wind speed (v) and proton density (ρ_p), the geomagnetic indices SYM-H, AE and PCI, the last two mostly related to auroral and polar cap conditions. PCN and PCS refer to the Polar Cap Index (PCI) at Northern (N) and Southern (S) hemispheres, respectively
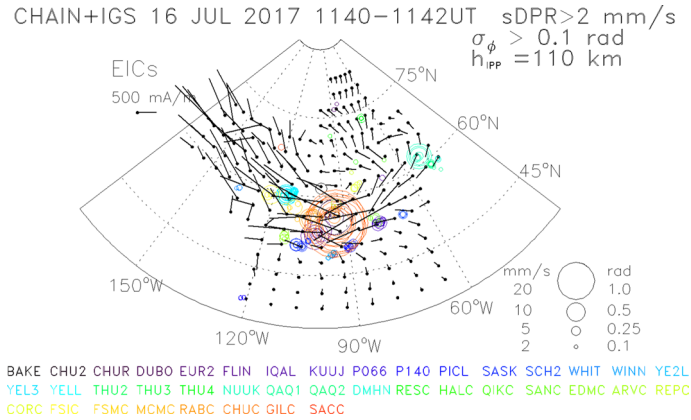
Fig. 32 Horizontal equivalent ionospheric currents observed over North America on 16 July 2017. IPPs where $\sigma_\Phi > 0.1$ rad or sDPR > 2 mm/s are shown as circles colour coded by stations and sized proportionally to σ_Φ and sDPR values

cloud, for example, an enhanced magnetic field. The result was a moderate geomagnetic storm with |SYM-H| reaching values up to 60 nT and the AE index exceeding 1600 nT (Fig. 31).

The SECS technique (Amm and Viljanen 1999) was used to obtain horizontal equivalent currents (EICs) (Weygand 2009) from an array of ground magnetometers across North America and Greenland (Weygand et al. 2011) to study this event. Assuming the shell height of 110 km for the IPP, strong GPS phase scintillation in the nightside auroral oval was co-located with the westward electrojet on July 16 (Fig. 32). The phase scintillation occurrence ($\sigma_\Phi > 0.1$ rad or the standard deviation of delta phase rate, sDPR, > 2 mm/s) is provided by CHAIN stations. The onset of GPS phase scintillation followed the southward turning of the IMF a few minutes after the IP shock that was associated with a northward IMF on 16 July around 06 UT (Fig. 32). The scintillation maximised in the auroral oval but then increased significantly during the day in the cusp and picked up again the next day in the nightside auroral oval.

Figure 33 shows the GPS phase scintillation occurrence as a function of the Altitude-Adjusted Corrected GeoMagnetic (AACGM) latitude and UT for GPS receiver stations located between 260° and 300° geographic longitude overlaid with contours of ionospheric J_y current. The J_y current shown in Fig. 33a is an average over the longitude sector between 267° and 295° with EICs transformed to geomagnetic coordinates using the magnetic declination at each grid cell. To conform to the 15 min grid span used for the scintillation occurrence map, the west-to-east J_y current component is averaged over 15 min (mean of 15 values using the 10 s EICs data decimated to one value per minute). Figure 33b shows the EIC contours colour coded with the magnitude of the J_y current. In the auroral zone, the highest occurrence of GPS phase scintillation is co-located with strong westward electrojet and the poleward edge of the eastward electrojet.

The main source of the storm that occurred between 4 and 10 September 2017 was the Solar Active Region AR2673, which produced four X-class eruptions, including the strongest flare X9.3 of Solar Cycle 24 on September 6, 2017. A ICME (started on 6 September) triggered a G4 (severe geomagnetic storm—NOAA Kp 8, Ap = 106) whose main phase was on 7–8 September 2017 (Tassev et al. 2017; Valommel and Van der Linden 2017).
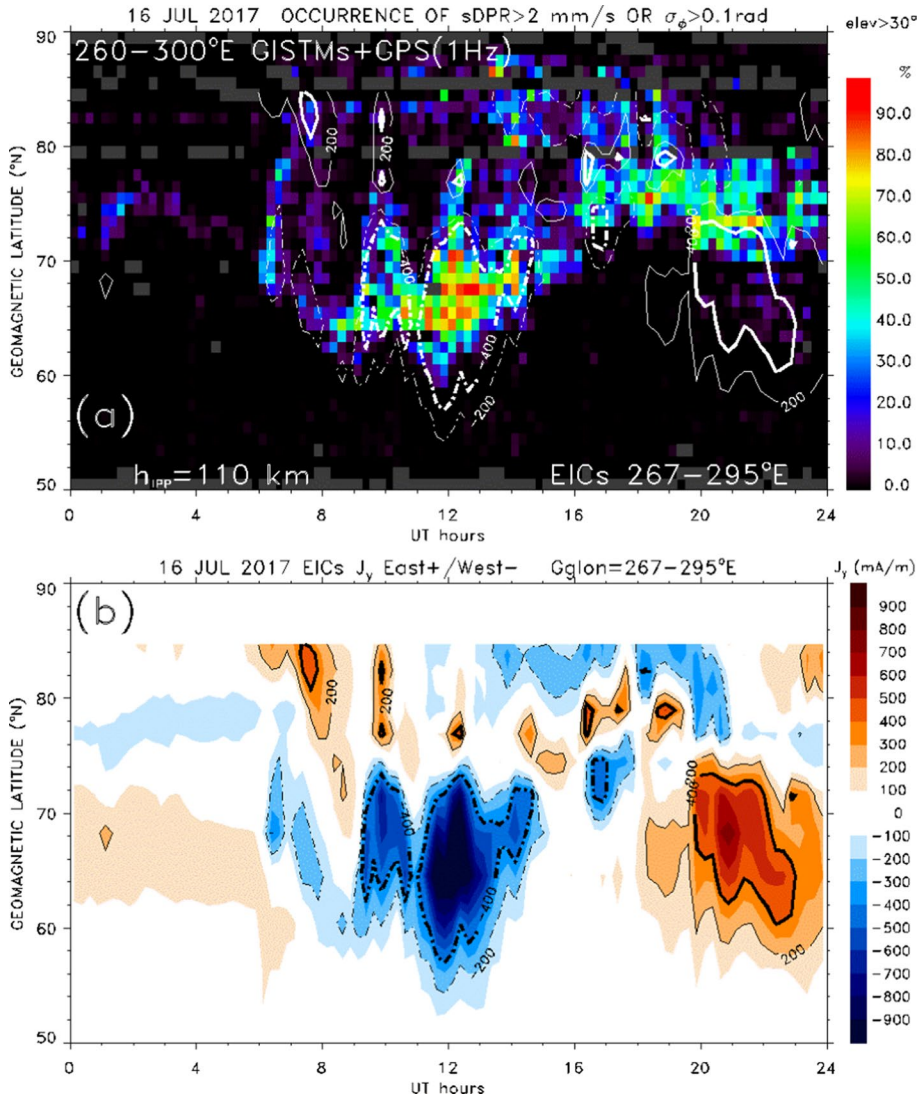
Fig. 33 a Phase scintillation occurrence of $\sigma_\Phi > 0.1$ rad or sDPR > 2 mm/s as a function of AAGCM latitude and UT for CHAIN combined with 1 Hz GPS geodetic quality receivers for data on July 16, 2017, for the longitude sector between 260° and 300°. Contour plots of the westward and eastward equivalent ionospheric currents are shown in white broken and solid lines, respectively. **b** Westward and eastward equivalent ionospheric currents (EIC) are highlighted in blue and brown shades

During the event of September 7–8, 2017 there were two distinct intervals of the interplanetary electric field rising, and correspondingly, the PC index increasing from 22:00 to 01:00 UT on September 7–8 and 12:00—14:00 UT on September 8, whereas the PCN index dropped to zero on the interval 08:00—11:00 UT on September 8. As a result, there were 2 splashes of magnetic substorm intensity with maxima of AE early at 00:00 UT and 12:00–14:00 UT on September 8. Indeed, the event consisted of two sequential storms
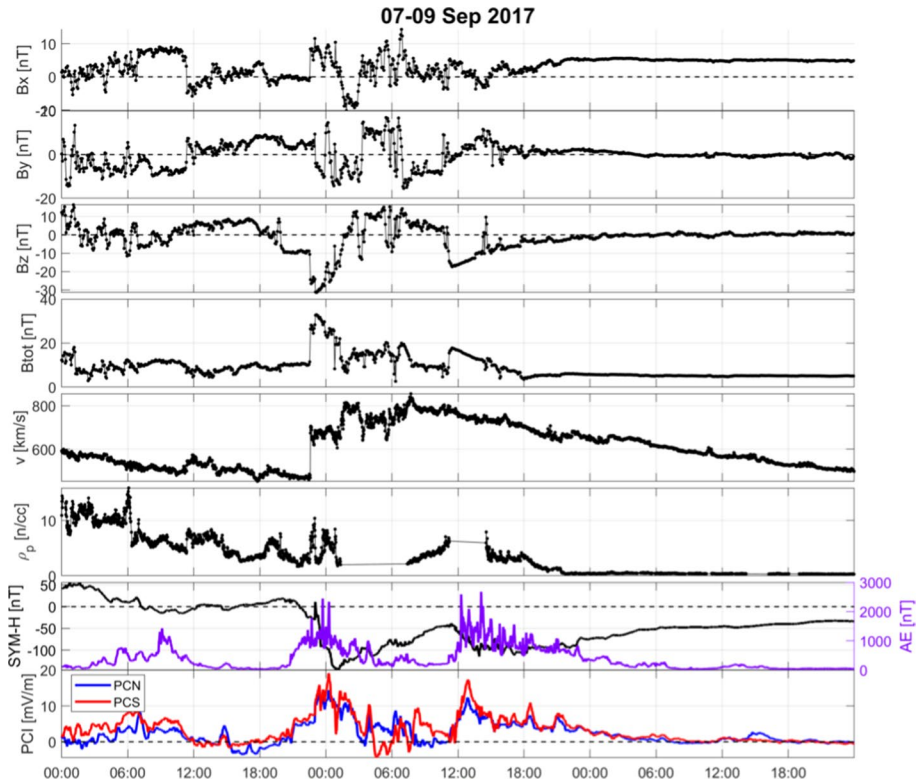
Fig. 34 Summary of the geospace characteristics during the event of 7–9 September 2017. From the top to the bottom they are plotted, vs UT: The Interplanetary Magnetic Field components (Bx, By, Bz, Btot), the solar wind speed (v) and proton density (ρ_p), the geomagnetic indices SYM-H, AE and PCI, the last two mostly related to auroral and polar cap conditions. PCN and PCS refer to the Polar Cap Index (PCI) at Northern (N) and Southern (S) hemispheres, respectively

peaking on September 8 (Blagoveshchensky and Sergeeva 2019), the first with a SYM-H minimum of -146 nT observed at 01:10 UT and the second with a SYM-H minimum of −110 nT at 16:01 UT. The geospace conditions are reported in Fig. 34.

In Antarctica, the ionogram series recorded between 13:00 and 16:00 UT on 8 September by the VIPIR (Vertical Incidence Pulsed Ionospheric Radar) ionosonde (Ham et al. 2020) in Jang Bogo station are given in Fig. 35. The reflected echoes show signatures of sporadic E-layer and spread-F testifying to the presence of ionospheric irregularities at different altitudes. The sequence also shows the lack of ionospheric reflections due to strong ionospheric absorption.

Obana et al. (2019), studied the impact of this storm on the plasmasphere using data from the Plasma Wave Experiment (PWE) onboard the Exploration of energisation and Radiation in Geospace/Arase (ERG/Arase) satellite (Kasahara et al. 2018; Miyoshi et al. 2018). From their study, the authors showed for the first time a deep erosion of the plasmasphere on 8 September 2017 during the recovery phase of the storm. The erosion consists of plasmapause radius reduced down to 2 Earth radii (R_E) compare to 4–6 R_E during normal geomagnetic conditions. The cause of the strong erosion of the plasmasphere is
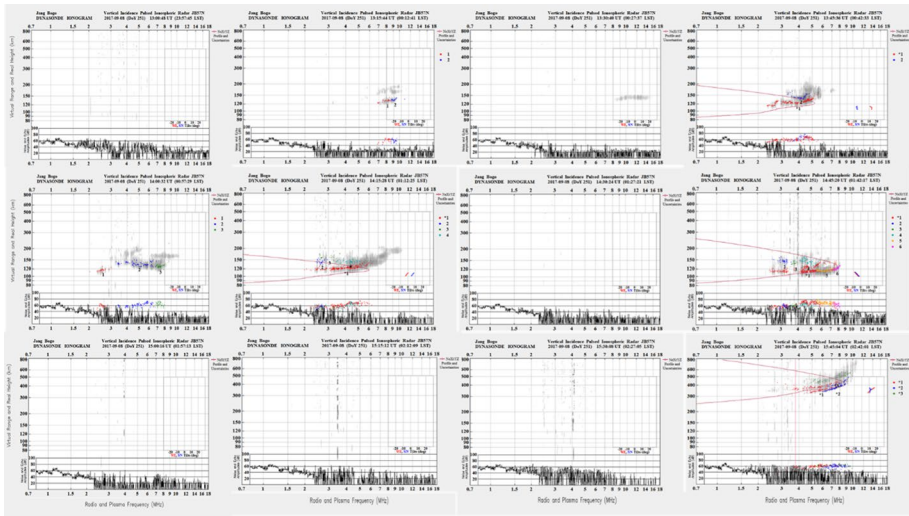
Fig. 35 Ionogram series recorded by Jang Bogo VIPIR between 13:00 and 16:00 UT on September 8, 2017

inferred as being due to electric field penetration from high latitudes to mid-latitudes during the recovery phase.

Yamauchi et al. (2018) investigated several X class solar flares and proton precipitation that occurred during three days, September 6–8, 2017. The drivers of ion upflows were investigated. During this event, the EISCAT radars ran with low-elevation pointing, intended for latitudinal cross-section observations. However, it could be concluded that ion up-flow occurred, not as a result of X-ray absorption but rather either as a result of an ICME arrival or driven by solar energetic particle precipitation. Schillings et al. (2018) investigated the oxygen ion (O^+) outflow from the polar cap and cusp in response to arrivals of ICME shocks and X-flares. They found an enhancement of the outflow by a factor of 3 in connection to one of the shock arrivals, which suggests that ICMEs may be the main drivers of the O^+ outflow. However, the outflows were in general higher than normal also before the shock arrival, suggesting that the prior X-flares and the EUV radiation associated with them caused pre-heating of the ionosphere and enhanced O^+ outflows as well. Schillings and co-authors show that during extreme geomagnetic storms an unusual condition can take place: the ion outflow velocity can be sufficient that ions pass the magnetotail X-line before reconnection occurs and therefore are permanently lost to the solar wind.

Berdermann et al. (2018) reported a significant response of not only the European-Arctic but of the entire European sector to the storm, assessing the impact on GNSS-based operations, which resulted in severe effects on precise positioning services used in maritime and aviation. The authors also reported a significant impact on the EGNOS Augmentation System supporting the safety of life services. The degradation of the GPS signals in the Arctic is also reported by Linty et al. (2018) and Yang et al. (2020b) using Software Defined Radio (SDR) and professional receivers to evaluate the increase in the position errors during the ionospheric scintillation events recorded at Svalbard on 7–8 September 2017. Blagoveshchensky and Sergeeva (2019) reported ionospheric absorption on HF signals over the high latitude Russian sector during the first minimum and no significant perturbations to radio propagation during the second peak of the storm. Zhang et al. (2019)
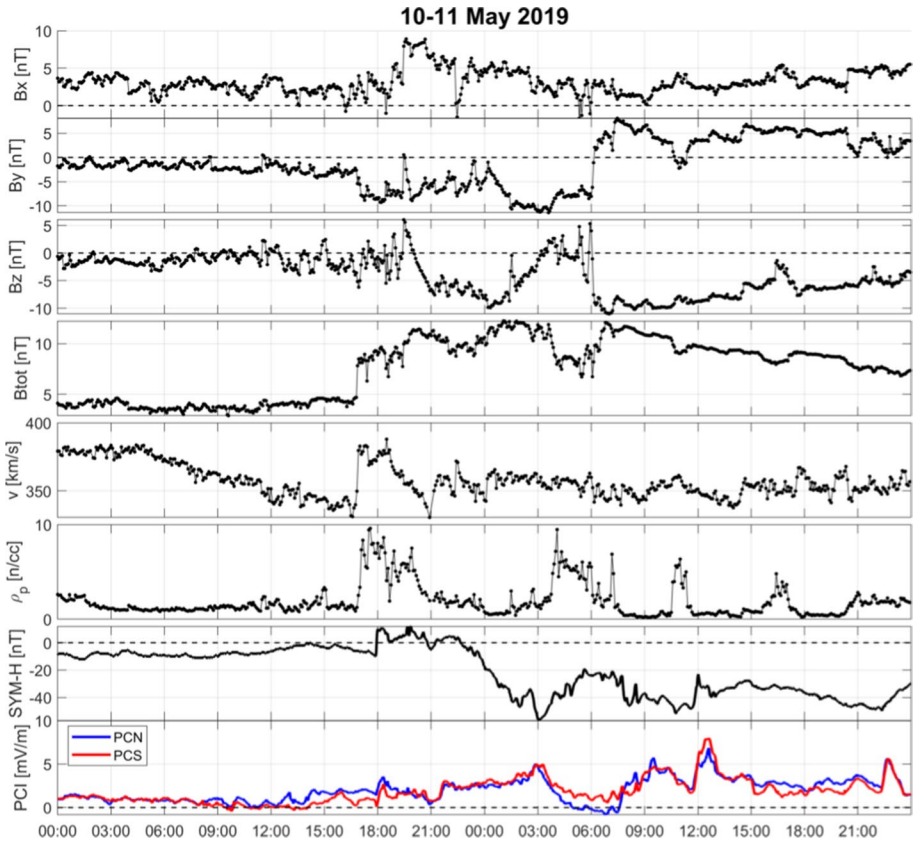
Fig. 36 Summary of the geospace characteristics during the event of 10–11 May 2019. From the top to the bottom they are plotted, vs UT: The Interplanetary Magnetic Field components (Bx, By, Bz, Btot), the solar wind speed (v) and proton density (ρ_p), the geomagnetic indices SYM-H and PCI, the last two mostly related to auroral and polar cap conditions. PCN and PCS refer to the Polar Cap Index (PCI) at Northern (N) and Southern (S) hemispheres, respectively

refer to an unexpected propagation of transpolar TIDs from dayside to nightside on 8 September, identifying the cusp region as being efficient to trigger poleward TIDs to auroral latitudes in the American and European sectors. D'Angelo et al. (2021) reported severe phase fluctuations at polar latitudes in both hemispheres and clear signature of amplitude scintillations recorded by GNSS receivers at SANAE and Concordia Antarctic stations during the main phase of the storm.

4.4 The Auroral Events in May 2019

The storm that occurred on 10–11 May 2019 is characterised by the geospace conditions described in Fig. 36.

A sudden increase occurred in the total IMF (Btot), solar wind density, solar wind speed, and solar wind dynamic pressure around 18:00 UT on 10 May. Such simultaneous enhancements indicate that the interplanetary shock, part of the ICME possibly

caused by the faint halo slow CME observed by SOHO/LASCO C2 on May 7, or by a co-rotating interaction region (CIR) observed on 9 May (Kwon et al. 2022), or by a combination of the two events, arrived at the Earth's bow shock. The source identification is out of the scope of this description, but the readers can refer to Piersanti et al. (2020) to understand the importance of the solar wind evolution to assess the actual impact on geospace. From 20:00 UT on 10 May to 06:00 UT on 11 May the solar wind density was extremely high with a peak of about 25 cm^{-3} while the bulk speed of solar wind increased up to 400 km/s (Fig. 36). After 06:00 UT on May 11, the direction of IMF Bz remained southward for 18 h or even longer. Such conditions caused a moderate geomagnetic storm in terms of temporal variation in the SYM-H index which decreased after the shock and reached a minimum of −57 nT around 03:00 UT on 11 May (Fig. 36).

Figure 37 shows the temporal developments of the aurora from the ASC (All Sky Camera) at Jang Bogo Station, Antarctica (JBS, 79.87S MLAT, 53.56 W MLON) during the geomagnetic storm of 11 May 2019. Red circles on the image indicate the spatial coverage of the Fabry Perot Interferometer (FPI) observations for neutral winds and temperature. The aurora begins to be observed at 12:15 UT near the eastern horizon. At 12:25 UT, the aurora is enhanced with broader spatial coverage over JBS in association with poleward expansion of the auroral oval. Auroral structures seem to be highly dynamic with time during this interval as shown in panel d. At 12:55 UT in panel f, the auroral intensity decreases except for the eastern sky of JBS as the poleward expansion of the auroral oval begins to return to its normal location. After 13:00 UT, the auroral activity becomes too weak to be observed from the ASC.

To compare the auroral activity with the temporal variations in the ionospheric currents, a zonal keogram derived from ASC and magnetic field measurements by magnetometer dIdD (Jee et al. 2021; Kwon et al. 2018) are shown in Fig. 38. The black and red lines in panels (b) to (d) depict the 1-min and 5-min average magnetic fields, respectively. There is no auroral activity from 08:00 UT to 12:15 UT on 11 May 2019, but the aurora starts appearing at the eastern horizon and keeps expanding westward within one hour. Between
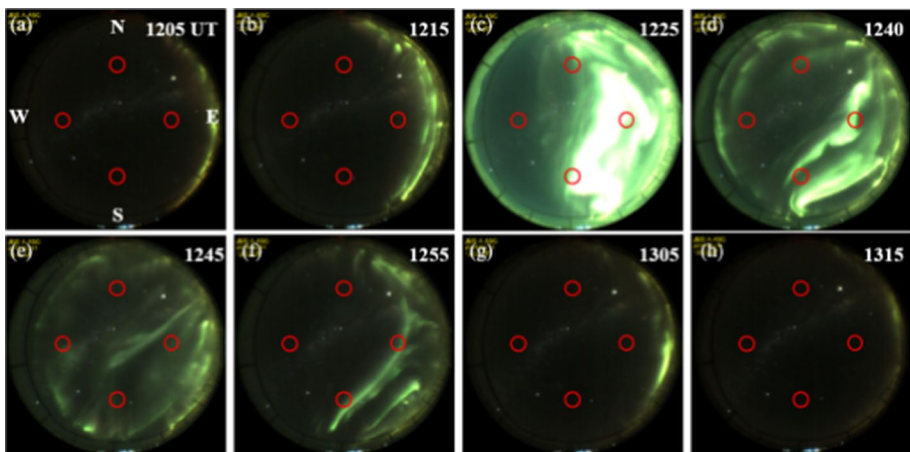

Fig. 37 All-sky images observed by Aurora All-Sky Camera (ASC) at JBS during the geomagnetic storm that occurred on May 11, 2019. The directions of the image and the observation time are indicated on each image. The red circles indicate four directions of line-of-sight for FPI observation
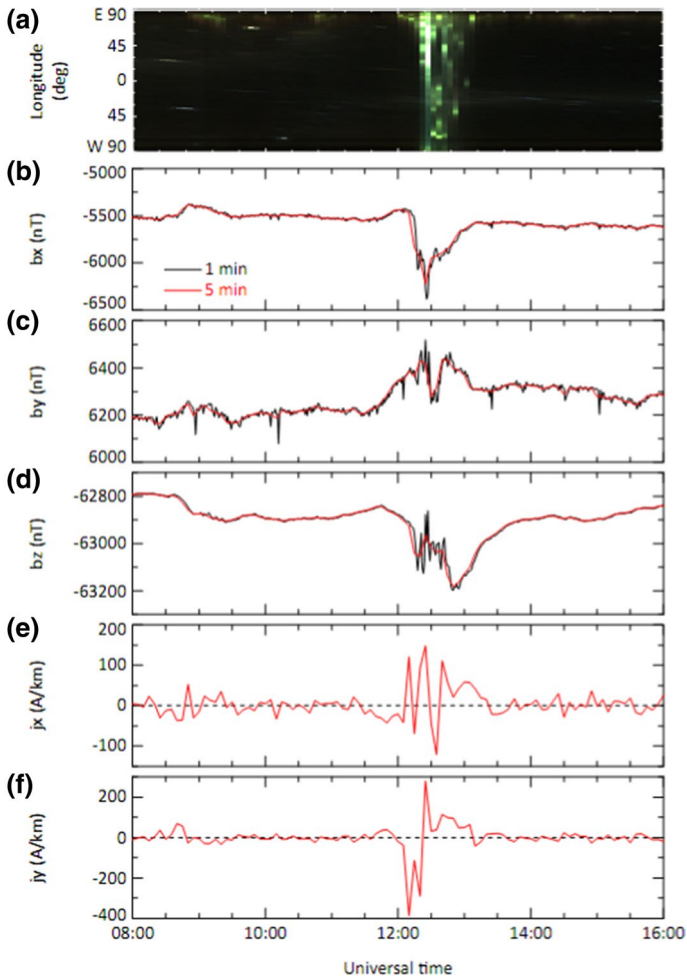
Fig. 38 (**a**) Keogram showing auroral activity in a zonal cross-section from the ASC. (**b**)–(**d**) Temporal variations in the geomagnetic field components measured by the dIdD magnetometer at JBS from 08:00 to 16:00 UT on 11 May 2019. The black and red lines in (**b**)–(**d**) indicate 1-min and 5-min averaged magnetic field, respectively. Panels (**e**)–(**f**) show the time plots of ionospheric currents derived from magnetic field measurements in (**e**) north–south and (**f**) east–west directions

12:25 UT and 13:00 UT, a bright aurora covers the whole sky and turns back to the eastern horizon at 13:30 UT. This temporal evolution of the auroral morphology is consistent with the variations in the magnetic field measured by the magnetometer. The x-component (meridional) in Fig. 38b shows obvious negative deviations from the background at the auroral breakup. When the aurora disappeared over JBS, the meridional component of the magnetic field also returned to the background level.

Figure 39a shows the neutral winds estimated from 630.0 nm airglow emissions observed by the JBS Fabry–Pérot interferometer FPI during the geomagnetic storm. The direction of the neutral wind is dominantly anti-sunward at JBS, being consistent with the ion convection in the polar cap region (Lee et al. 2017). The most remarkable feature is the minimum strength of meridional wind near the local midnight. The strong westward

Fig. 39 Ionospheric variations observed by FPI at JBS during the geomagnetic storm of 11 May 2019. **a** Two-dimensional wind vectors in geographic coordinates with local time. Time series plots of **b** intensity and **c** temperature of ionospheric airglow
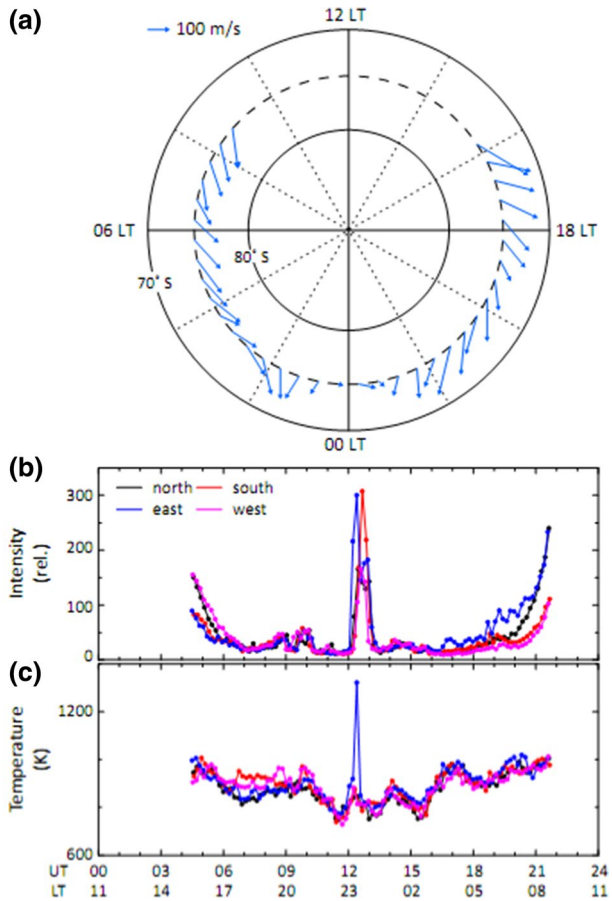
currents, as shown in Fig. 38f, drive large zonal wind but small meridional wind during the active period (Fig. 39a). As the auroral activity weakens, the meridional wind becomes larger than the zonal wind.

Clear enhancements of the airglow emissions were detected for all directions at the auroral onset at around 12:00 UT (Fig. 38a). From the measurements of airglow intensity, we found that there were auroral emissions with red colour at about 250 km, which is the peak altitude of 630.0 nm airglow mission, although the ground-based aurora ASC detected only green aurora at lower altitudes (Fig. 37). We also found that the evolution of aurora observed by the aurora ASC is consistent with the observations of the airglow intensity from the JBS FPI.

The perturbations of the ionospheric currents shown in Fig. 38e–f are assumed to be the electric field perturbations, which causes Joule heating. The Joule heating can be measured as an increase in the temperature in the upper atmosphere. When aurora appeared at the eastern edge of ASC, FPI also captured substantial temperature increases in the same direction as shown in Fig. 39c. Note that the intensity of the airglow emission was enhanced in all directions of the FPI measurement in contrast with the temperature enhancement only in the eastern sky. This spatial discrepancy between airglow intensity and temperature might

SANAE-IV and Troll, 10-11 May 2019
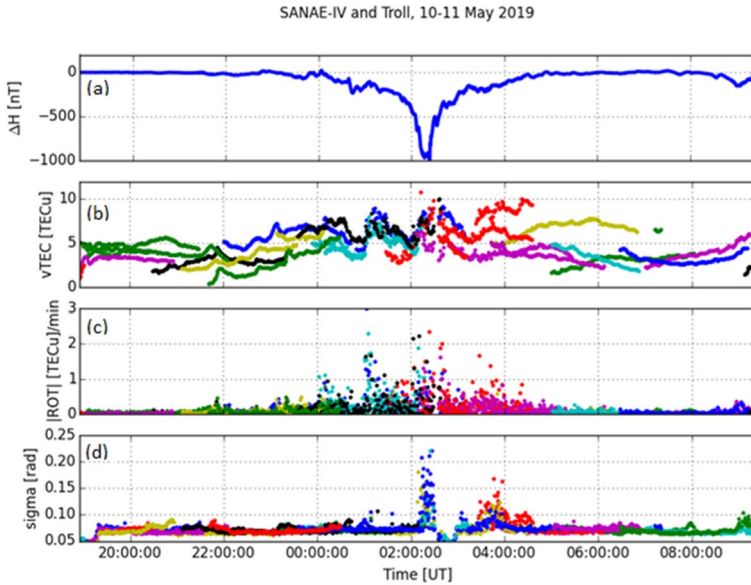
Fig. 40 **a** Magnetic field variations observed over SANAE-IV, and **b** vertical TEC, **c** ROT and **d** σ_Φ scintillation index observed over Troll on 10–11 May 2019

be related to the time delay between the aurora intensification and the enhancement of the Joule heating rate.

This geomagnetic storm was also observed at the Norwegian Research Station Troll (geographic coordinates: 71.7°S 2.8°W, magnetic coordinates: 62.8°S 47.8°E) and South African Station SANAE-IV (72.0°S 2.5°E, magnetic coordinates 62.0°S, 42.1°E) both located in Queen Maud Land, with a distance of about 200 km from each other. Figure 40 shows that there were variations in the magnetic field observed at SANAE-IV on 11 May, with the minimum ΔH at about 02:00 UT, which can be related to strong ionospheric current activity. This coincides with large variations in TEC observed over Troll, as shown in Fig. 40b. A clear peak in phase fluctuations σ_Φ indicates large structuring in the plasma. The auroral imager at Troll recorded intense emissions at 630 nm and 557.7 nm due to strong electron precipitation at about 02:30 UT, and this activity is typical for the auroral substorm (Fig. 41). The largest phase fluctuations in the GNSS signals were associated with the expansion phase of the substorm. Clear auroral arcs were observed during the onset of the substorm and in the recovery phase. Since the arcs were localised, they affected a smaller number of GNSS satellites. Variations in the ΔH component over SANAE suggest dynamic changes in the ionospheric current system, which could facilitate structuring in the plasma as reflected in TEC and scintillation data over Troll. The activity observed at Troll and SANAE-IV has about 10 h offset from the Jang Bogo station, but maximum variations in the Bz and Bx components of the magnetic field have similar characteristics at both locations. This shows that the storm of 10–11 May was a global event and that the extensive duration of IMF Bz negative was facilitating magnetosphere-ionosphere-thermosphere coupling and allowed for deposition of energy into the polar ionosphere through both auroral particle
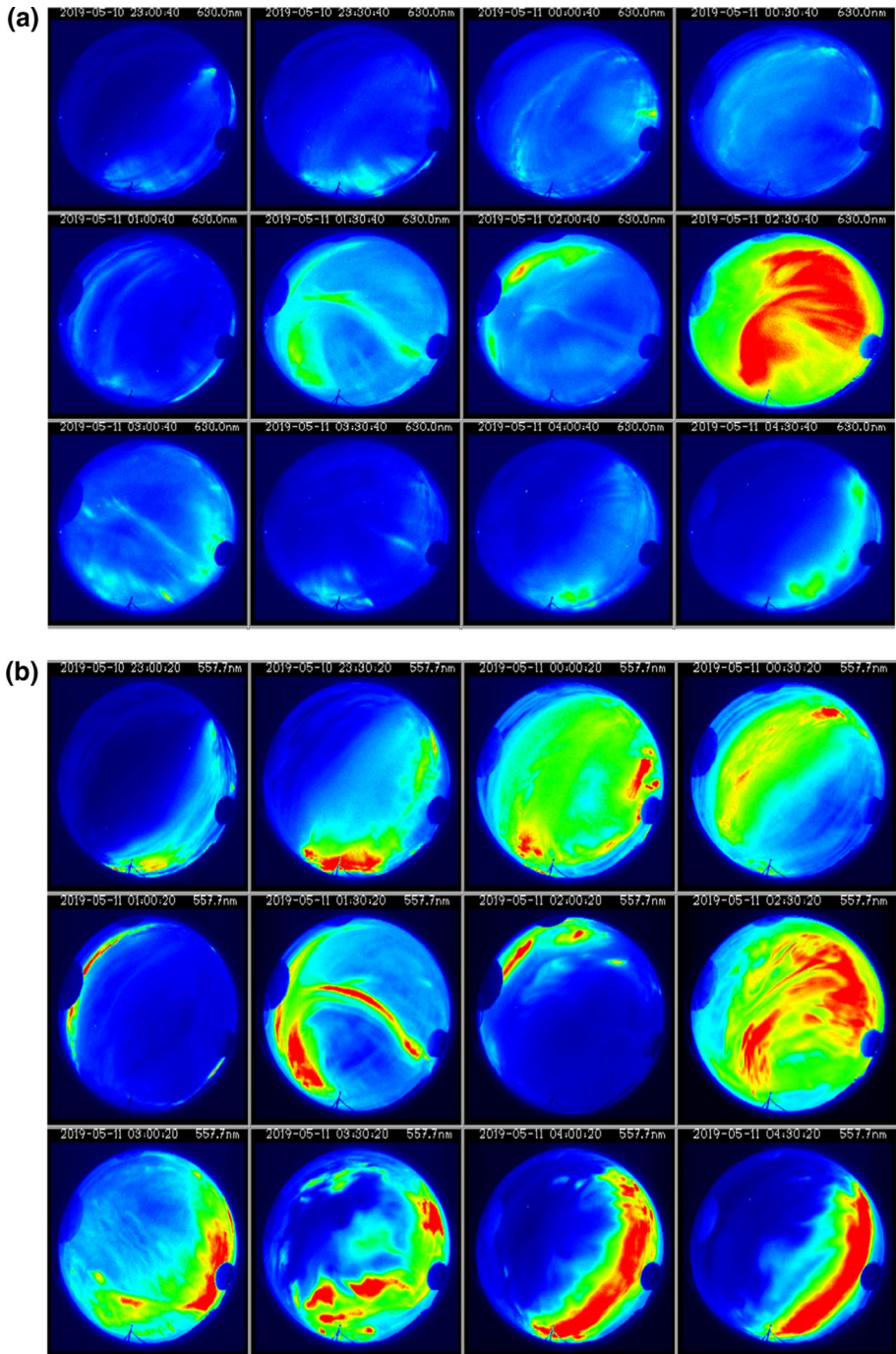
(a)

(b)

Fig. 41 All-sky imager data from Troll station showing the intensity of emissions in **a** 630 nm and **b** 557,7 nm on 10–11 May 2019. The colour scale is arbitrary

Fig. 42 Southern high-latitude SuperDARN convection maps at about one hour before the auroral maximum luminosity is observed at Troll and JBS (panel **a** and **d**), at the auroral luminosity maximum (panels **b** and **e**), and about two hours after the luminosity maximum (panel **c** and **f**). The maps are shown in a magnetic local time-magnetic latitude grid with noon at the top and dusk on the left. The solid green line is the Heppner-Maynard Boundary. The minimum latitude of the HMB is reported in the bottom left of each map. The difference between the potential maximum and minimum is indicated in the top left of each map. The interplanetary magnetic field component in the Geocentric Solar Magnetospheric GSM Y–Z plane is shown at the top right of each map

precipitation and frictional Joule heating. Analysis of data from different regions of Antarctica allows for longer monitoring and better characteristics of this event.

The global Southern ionospheric convection at the time of SANAE, Troll and Jang Bogo Station observations is presented in Fig. 42. The ionospheric convection maps are generated starting from the SuperDARN radars velocity measurements available in the Southern hemisphere for the periods of interest. The Radar Software Toolkit 4.2 (RST; SuperDARN Data Analysis Working Group, 2017, 2018, https://superdarn.github.io/dawg/files/DAWG_Report_2018.pdf) is used to produce the global convection maps according to the potential mapping technique by Ruohoniemi and Baker (1998). The statistical model of Thomas and Shepherd (2018) is chosen for adding measurements in regions where there are no observations from the radars. Such a model is parametrised by the solar wind, IMF, and dipole tilt angle conditions. The convection maps are available at 2-min intervals.

The evolution of the convection during the 00:00–04:00 UT and the 10:00–14:00 UT intervals when Troll and JBS observations are available has been studied by examining the entire set of maps generated from the radar data. In Fig. 42, six convection maps are shown. These represent the principal features of the convection evolution and possibly show the large scale magnetospheric dynamics, for the two periods under study. The maps are displayed in a magnetic local time-magnetic latitude grid with noon at the top and dusk on the left. The latitudinal extension of the convection pattern is represented by the Heppner-Maynard Boundary (HMB) determined using radar data (Shepherd and Ruohoniemi, 2000). The HMB is located at the lowest latitude for which at least three line-of-sight vectors with a velocity greater than 100 m/s lie on the boundary. In Fig. 42, the HMB is the solid green line, and the minimum latitude of the HMB, the latitude of the intersection of the HMB with the midnight meridian, is reported in the bottom left corner.

The maps cover periods at about one hour before (top row) and after (bottom row) the auroral maximum luminosity, in correspondence with the auroral maximum luminosity (middle row) as observed at Troll (panels a, b, c) and JBS (panels d, e, f)). The convection is mainly characterised by two cells with antisunward flows in the polar cap. During the first period (panels on the left column), the two cell pattern is rotated towards afternoon MLT since the IMF has a dusk-ward component. Such a convection pattern can be set in the framework where reconnection at the dayside magnetopause and in the geomagnetic tail drives the antisunward convection in the polar cap (with the return flows at lower latitudes). Moreover, it can be noted that the latitudinal extension of the convection varies between the maps of different rows. This is also highlighted by the value of the minimum latitude of the HMB. In this respect, it has to be noted that the HMB is well defined when the maps contain a sufficient number of data: for the first period the majority of maps contains more than 200 points, which has been used as a threshold in the past (Imber et al. 2013); for the second period the data points are overall fewer, but still above 100, which appears as a critical number below which the
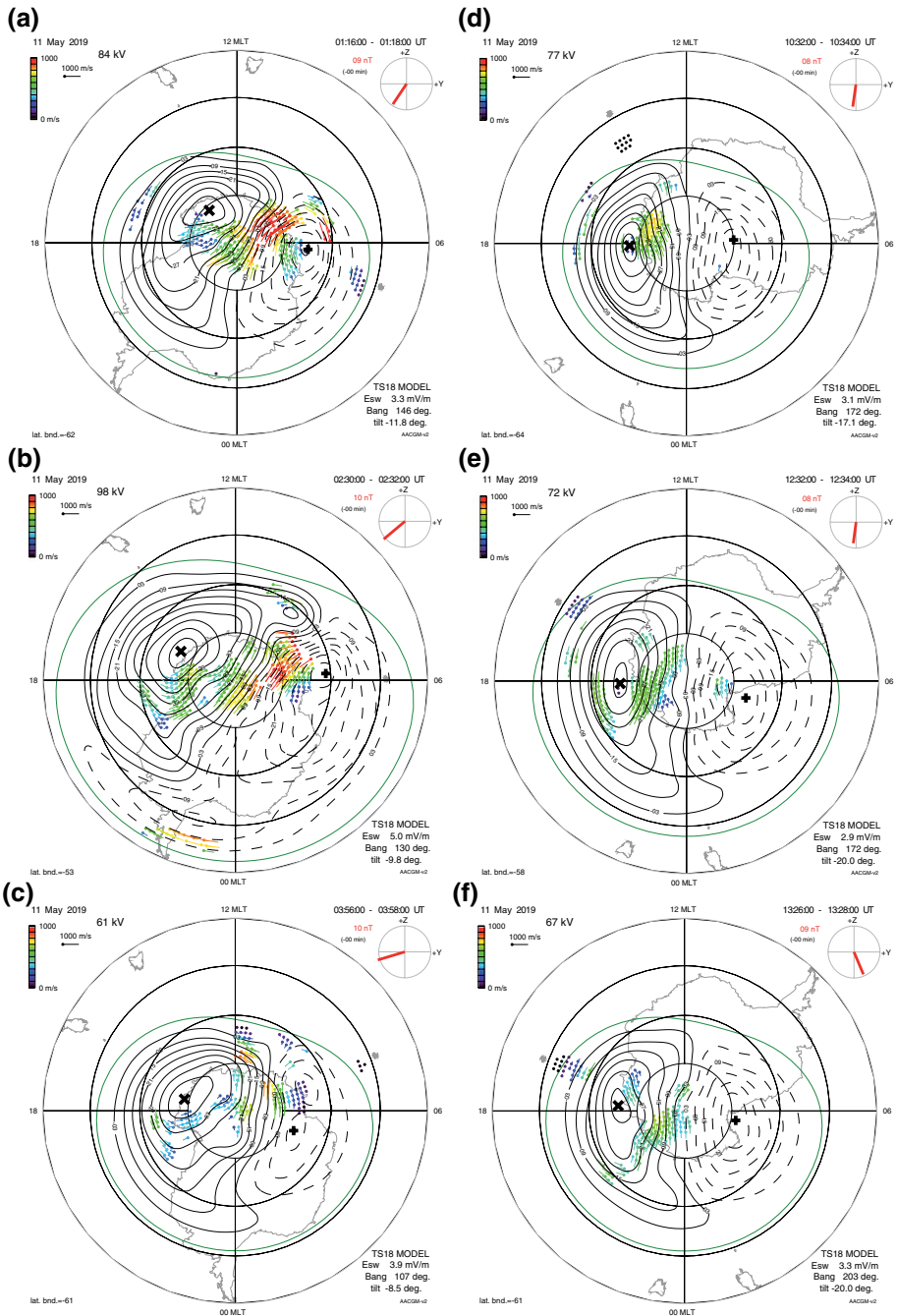
HMB attains unrealistic values, for the majority of the maps. The polar cap can expand and contract when the open terrestrial magnetic flux changes due to the variability of the dayside and nightside reconnection rate (Milan et al. 2007 and references therein).

Altogether, with the polar cap area, also the extension of the convection pattern varies (Imber et al. 2013). For both the periods considered, an expansion can be noted of the convection pattern shown in the maps of the middle row that pertains to the maximum luminosity of the auroras shown in the maps of the top row. This can be interpreted as due to the addition of open flux to the magnetosphere lobes because of ongoing reconnection at the dayside magnetopause. Indeed, the observed equatorward propagation of the equatorward edge of SuperDARN backscatter is characteristic of the substorm growth phase (Chisham et al. 2007 and references therein). Instead, a contraction of the convection pattern is observed when comparing the two maps in the middle row with the respective maps in the bottom row. Such a contraction can be related to the reconnection in the geomagnetic tail, at the origin of the auroras observed at Troll and JBS, which eventually leads to magnetic flux re-closure and the consequent contraction of the polar cap and the convection pattern. Although the sparseness of data coverage at lower latitudes could be of some relevance for an accurate determination of the convection pattern extension, the observed evolution appears in agreement with the results of the superposed epoch analysis of the HMB during substorms by Imber et al. (2013). The convection pattern in the map of panel b), when the maximum luminosity aurora is observed at Troll, is characterised by an anticlockwise vortex at very low latitudes in the midnight sector, which is present in all the maps during the 02:24–02:44 UT interval (not shown here). The nature of these flows is somewhat different from the nightside convection usually observed by SuperDARN during substorms (Grocott et al. 2002). This difference can be due to processes occurring in the inner magnetosphere (e.g. sub auroral polarisation stream). Depending on its actual origin, the presence of such a vortex could have artificially enhanced the HMB expansion to a certain degree.

5 Final Remarks and Next Steps

This survey focused on the observing capabilities and scientific knowledge gained in the last two decades by the international community that studies the atmosphere and the geospace using observations acquired at and over the polar regions by means of radio probing supported by auxiliary methods.

The polar regions are highly sensitive to geospace events, hence the poles are considered to be space weather sentinels. Indeed, observation of the upper atmosphere at the poles is crucial for a deep understanding of the physical mechanisms by which space weather drives the dynamics of the circumterrestrial space and its effects on the ground. Such a deep understanding of space weather drivers and effects are essential to develop reliable forecasting models and to adopt trustworthy mitigation actions.

To discriminate between quiet and perturbed geospace conditions scientists often make use of a norm designated as the "ambient average environment" to recognise discrepancies associated with disturbances. The norm can be derived through the use of models, data or a combination of data and models. The availability of long-term polar data series is indispensable to build up a climatological picture of the response of the atmosphere to the Sun-Earth interaction.

The combination of long-term and short-term studies of the polar upper atmosphere is central to advancing our current knowledge of the global environment and making progress

towards providing robust and reliable support for technologies that are vulnerable to impacts by space weather.

Long-term observations of the polar atmosphere are important for the study of global change. Also in this framework, the poles play a central role and their monitoring provides several key pieces of information to advance the assessment of the contribution of different factors (anthropogenic or natural) in global change that originate from below or come from outer space.

From the monitoring perspective, data from close to 350 ground observatories are currently available. These observatories allow the estimation of tropospheric water vapour content or Precipitable Water (PW), Total Electron Content (TEC), plasma properties in the ionosphere and plasmasphere, disturbances of the geomagnetic field, and many more geophysical parameters. Such a vast resource enables the investigation of the neutral and ionised atmosphere at high latitudes over long and short term periods. These observing sites cover a substantial part of the polar regions. However, the data coverage is still uneven with gaps remaining especially in Eastern parts of Antarctica and in the Arctic polar sector. While satellite data are presently used to fill these gaps, new ground-based instrumentation infrastructures should be installed in the future to improve the current coverage and provide the means for the calibration of satellite data. Additionally, national institutions or international groups should join their efforts to install co-located instrumentations to facilitate multi-disciplinary approaches to polar research.

The combined adoption of data acquired by Low Earth Orbit satellites and ground-based instruments, supported by the use of models, can effectively contribute to the investigation of global climate change throughout the monitoring of the Arctic and Antarctic troposphere. Using this approach, scientists have revealed several significant features of the atmosphere, such as the marked difference between the two poles of recent global warming. The paucity of observations in the upper part of the atmosphere over the polar regions is still a factor that limits the advancement of knowledge. This is particularly the case for mesosphere-lower thermosphere investigations that lack continuous ground-based observations in the vicinity of the stratospheric polar vortex edge, especially in Antarctica. Studies considering the interaction between the upper mesosphere and the lower thermosphere/ionosphere highlight the potential of the multi-disciplinary and multi-instruments approach. Indeed, by using VLF and ionosondes, it has been made possible to identify the oscillations associated with gravity waves in the D and E regions in the lower ionosphere. Riometers allowed a deep knowledge of the response of the lower ionosphere to energetic particle precipitation caused by several phenomena such as ICMEs, solar proton events, and solar X-ray flares.

Among others, we cite the SuperDARN facilities as one of the most flexible types of ground-based equipment with a large spectrum of possible applications to investigate the circumterrestrial space, from the magnetosphere to the lower ionosphere and mesosphere. Just to mention a few achievements, SuperDARN has been successfully used to identify the polar cusp and the Lower Latitude Boundary Layer regions of the magnetosphere, to provide valuable inputs to the Geospace Environment Modelling (GEM) program, and its observations have been used to study ionosphere dynamics, ULF waves and mesospheric winds above Antarctica.

Another formidable source of new information came with the advent of GPS in the 1990s. The exploitation of the GNSS signals received both at the ground and by LEO

satellites allowed an in-depth investigation of the ionospheric climatology in the polar ionosphere under different geospace conditions. From GNSS data analysis resulted a significant advancement in the study of the polar troposphere. More recently, GNSS data have been used to pursue studies on the plasmasphere at the poles, a topic not yet well understood. The availability of special GNSS receivers configured to monitor ionospheric scintillations boosted additional interest in the corruption of GNSS position estimation by the ionospheric perturbations. The increasing deployment of this kind of receiver requires further international efforts to identify shared common metrics to define what is the meaning of the phase scintillation and to improve the algorithms for its derivation.

Although available for shorter periods than one solar cycle, in situ data acquired by LEO satellites, such as those provided by CHAMP, COSMIC, Swarm, GRACE and FORMOSAT-3/COSMIC, have been demonstrated to provide valuable additional insights into ionospheric weather and climate. From the use of in situ data, for instance, the southern polar cap was found to show a higher variability of the plasma than the northern polar cap, possibly due to the offset of the geomagnetic pole and the geometry of the magnetic field.

Our review on ionospheric weather describes some examples of what we learnt and suggests what we do not know yet. The following list of observations and questions, even if not exhaustive, can hopefully help to address future research in our field.

1. Due to the nearly vertical geometry of the geomagnetic field lines at high latitudes, the reconnection between the Earth's magnetic field and the IMF results in a prompt response of the auroral and polar ionosphere to fluctuations in the solar wind modifications. The question is, how prompt is that reaction and how does the electric field penetrate to low latitude?
2. The effects of solar perturbations on the upper atmosphere over the poles are often asymmetric. Do we fully understand the reason for such asymmetries?
3. What is the role of the coupling between the neutral and the ionised layers in the atmosphere at the poles?
4. Can we interpret plasmaspheric erosion as the signature of electric field penetration from high to low latitudes during geomagnetic storms?
5. Can we identify when ionospheric plasma structuring at high latitudes appears as fragmentation from large to smaller-scale structures or vice versa as clustering of small-scale irregularities into larger-scale configurations? What are the mechanisms for each of these forms of restructuring?
6. Can we understand the origins of the long-term behaviour of the polar ionosphere and discriminate between natural and anthropogenic contributions to such change?
7. How can we improve the modelling of the coupling of the neutral atmosphere to the ionised atmosphere at high latitudes?
8. Is it possible to identify the contribution of anthropogenic and natural sources in the assessment of climate change over the poles?

To progress on these (and many other) open questions, the increase in monitoring through improving the current coverage and extending the number of multi-instruments sites is fundamental. The overview of long term investigations and space weather events described in Sects. 2 and 3 testifies how, despite the remoteness and harsh conditions of the polar environment, the scientific community is improving significantly its capacity

to monitor the atmosphere at high latitudes. A lot more should be done. To this end, the following actions are proposed:

- Strengthen the collaboration between atmospheric scientists with heliophysicists to learn more about solar wind forecasting (including CMEs propagation) and space weather impacts;
- Foster the collaboration among experts of different disciplines, such as astrophysics, planetology, neutral atmosphere physics and chemistry, and heliophysics to share the competencies necessary to understand the roles of different drivers of atmospheric and ionospheric dynamics from above and below;
- Facilitate the sharing of data, algorithms and models to harmonise the exploitation of the information (adoption of standards, agreement on metrics, use of shared communication tools, use of interoperable tools, etc.);
- Keep and strengthen the collaboration between the research communities that manage and exploit ground-based and in-situ observations to optimise and maximise the efforts given an increasing number of multi-instruments sites on the ground and multi-sensors payloads in space.

Our survey of the achievements gained in the last two decades in the field of the geospace environmental monitoring at both poles points out the urgent need to reinforce the existing international coordination to overcome the current gaps in the observing systems, from ground-based and satellite equipment, and to stimulate and facilitate the adoption of a multidisciplinary approach as the preferred method to significantly advance the state of the art in the knowledge of global change and the geospace environment.

Declarations

References

Alfonsi L, Kavanagh AJ, Amata E, Cilliers P, Correia E, Freeman M et al (2008) Probing the high latitude ionosphere from ground-based observations: the state of current knowledge and capabilities during IPY (2007–2009). J Atmos Solar-Terr Phys 70(18):2293–2308

Alfonsi L, De Franceschi G, De Santis A (2008) Geomagnetic and ionospheric data analysis over Antarctica: a contribution to the long term trends investigation. Ann Geophys 26(5):1173–1179

Alraddawi D, Sarkissian A, Keckhut P, Bock O, Noël S, Bekki S, Irbah A, Meftah M, Claud C (2018) Comparison of total water vapour content in the Arctic derived from GNSS, AIRS, MODIS and SCIAMACHYMeas. Tech 11:2949–2965. https://doi.org/10.5194/amt-11-2949-2018

Amante C and Eakins BW (2009) ETOPO1 1 Arc-Minute Global Relief Model: Procedures, Data Sources and Analysis. NOAA Technical Memorandum NESDIS NGDC-24 National Geophysical Data Center, NOAA https://doi.org/10.7289/V5C8276M [28.05.2018]

Amm O, Viljanen A (1999) Ionospheric disturbance magnetic field continuation from the ground to the ionosphere using spherical elementary currents systems. Earth Planets Space 51:431–440. https://doi.org/10.1186/BF03352247

Arras C, Wickert J, Beyerle G, Heise S, Schmidt T, Jacobi C (2008) A global climatology of ionospheric irregularities derived from GPS radio occultation. Geophys Res Lett. https://doi.org/10.1029/2008gl034158

Aquino M, Moore T, Dodson A, Waugh S, Souter J, Rodrigues F (2005) Implications of ionospheric scintillation for GNSS users in Northern Europe. J Navig 58(2):241–256. https://doi.org/10.1017/S0373463305003218

Astafyeva E, Zakharenkova I, Förster M (2015) Ionospheric response to the 2015 St. Patrick's Day Storm: a global multi-instrumental overview. J Geophys Res Space Phys 120:9023–9037. https://doi.org/10.1002/2015JA021629

Astafyeva E, Zakharenkova I, Alken P (2016) Prompt penetration electric fields and the extreme topside ionospheric response to the June 22–23, 2015 geomagnetic storm as seen by the Swarm constellation. Earth Planets Space 68(1):152

Bageston JV, Wrasse CM, Gobbi D, Takahashi H, Souza PB (2009) Observation of mesospheric gravity waves at Comandante Ferraz Antarctica Station (62° S). Ann Geophys 27:2593–2598. https://doi.org/10.5194/angeo-27-2593-2009

Bageston JV, Wrasse CM, Hibbins R, Batista PP, Gobbi D, Takahashi H, Fritts DC, Andrioli VF, Fechine J, Denardini CM (2011) Case study of a mesospheric wall event over Ferraz station, Antarctica (62 degrees S). Ann Geophys 29(1):209–219. https://doi.org/10.5194/angeo-29-209-2011a

Bageston JV, Wrasse CM, Batista PP, Hibbins RE, Fritts DC, Gobbi D, Andrioli VF (2011) Observation of a mesospheric front in a dual duct over King George Island, Antarctica. Atmos Chem Phys 11:12137–12147. https://doi.org/10.5194/acp-11-12137-2011b

Baker KB, Dudeney JR, Greenwald RA, Pinnock M, Newell PT, Rodger AS, Mattin N, Meng CI (1995) HF radar signatures of the cusp and low-latitude boundary layer. J Geophys Res Space Phys 100(A5):7671–7695

Baker KB, Wing S (1989) A new magnetic coordinate system for conjugate studies at high latitudes. J Geophys Res 94:9139–9143

Beirle S, Lampel J, Wang Y, Mies K, Dörner S, Grossi M et al (2018) The ESA GOME-Evolution "Climate" water vapor product: a homogenized time series of H$_2$O columns from GOME, SCIAMACHY, and GOME-2. Earth Syst Sci Data 10(1):449–468

Belakhovsky V, Pilipenko V, Engebretson M, Sakharov Y, Selivanov V (2019) Impulsive disturbances of the geomagnetic field as a cause of induced currents of electric power lines. J Space Weather Space Clim 9:A18. https://doi.org/10.1051/swsc/2019015

Béniguel Y (2002) Global ionospheric propagation model (GIM): a propagation model for scintillations of transmitted signals. Radio Sci. https://doi.org/10.1029/2000RS002393

Berdermann J, Kriegel M, Banyś D, Heymann F, Hoque MM, Wilken V et al (2018) Ionospheric response to the X9.3 Flare on 6 September 2017 and its implication for navigation services over Europe. Space Weather 16:1604–1615. https://doi.org/10.1029/2018SW001933

Bergeot N, Chevalier J-M, Bruyninx C, Pottiaux E, Aerts W, Baire Q, Legrand J, Defraigne P, Huang W (2014) Near real-time ionospheric monitoring over Europe at the Royal Observatory of Belgium using GNSS data. J Space Weather Space Clim 2014(4):A31. https://doi.org/10.1051/swsc/2014028

Bergeot N, Alfonsi L, Cilliers PJ, De Franceschi G, Correia E, Enell C-F, Engebretson MJ, Häggström I, Heygster G, Kauristie K, Kosch M, Lee C, Macotela E, Marcucci F, Miloch WJ, Morton J, Negusini M, Pottiaux E, Shreedevi PR, Prikryl P, Spogli L, Stephenson JAE, Troshichev O, Van Malderen R, Zou S, and the GRAPE EG members (2020) Polar atmosphere and Geospace: present knowledge, infrastructures and future research directions https://scar.org/scar-library/reports-and-bulletins/scar-bulletins/5570-scar-bulletin-203/

Bhawre P, Mansoori AA, Yadav R, Khatarkar P, Purohit PK, Gwal AK et al (2011) The response of polar, equatorial and low latitude ionosphere to the minor magnetic disturbance of 11 October 2008. IJEST 3:150–155

Bilitza D, Altadill D, Truhlik V, Shubin V, Galkin I, Reinisch B, Huang X (2017) International reference ionosphere 2016: from ionospheric climate to real-time weather predictions. Space Weather 15(2):418–429

Billett D, McWilliams K (2020) The SuperDARN's role in ion-neutral coupling research. Polar Sci. https://doi.org/10.1016/j.polar.2020.100624

Bjoland LM, Ogawa Y, Hall C, Rietveld M, Løvhaug UP, La Hoz C, Miyaoka H (2017) Long-term variations and trends in the polar E-region. J Atmos Solar Terr Phys 163:85–90

Blagoveshchensky DV, Sergeeva MA (2019) Impact of geomagnetic storm of September 7–8, 2017 on ionosphere and HF propagation: a multi-instrument study. Adv Space Res 63(1):239–256. https://doi.org/10.1016/j.asr.2018.07.016

Bland EC, McDonald AJ (2016) High spatial resolution radar observations of ultralow frequency waves in the southern polar cap. J Geophys Res Space Phys 121(5):4005–4016. https://doi.org/10.1002/2015JA022235

Bland EC, Heino E, Kosch M, Partamies N (2018) SuperDARN radar-derived HF radio attenuation during the September 2017 solar proton events. Space Weather 16:1455–1469. https://doi.org/10.1029/2018SW001916

Bland EC, Partamies N, Heino E, Yukimatu AS, Miyaoka H (2019) Energetic electron precipitation occurrence rates determined using Syowa East SuperDARN radar. J Geophys Res Space Physics 124(7):6353–6265. https://doi.org/10.1029/2018JA026437

Buehler SA, Östman S, Melsheimer C, Holl G, Eliasson S, John V, Blumenstock T, Hase F, Elgered G, Pscheidt I, Redl S, Steinke S (2012) A multi–instrument comparison of integrated water vapour measurements at a high latitude site. Atmos Chem Phys 12:10925–10943

Brändström BUE, Leyser TB, Steen Å, Rietveld MT, Gustavsson B, Aso T, Ejiri M (1999) Unambiguous evidence of HF pump-enhanced airglow at auroral latitudes. Geophys Res Lett 26(23):3561–3564

Brändström U (2003) The Auroral Large Imaging System—Design, operation and scientific results, PhD thesis, IRF Scientific Report 279, Swedish Institute of Space Physics, Kiruna, Sweden, ISBN 91–7305–405–4.

Browne S, Hargreaves K, Honary B (1995) An imaging riometer for ionospheric studies. Electron Commun Eng J 7(5):209–217

Buonsanto MJ, Witasse OG (1999) An updated climatology of thermospheric neutral winds and F region ion drifts above Millstone Hill. J Geophys Res Space Phys 104(A11):24675–24687

Byun SH, Bar-Sever YE (2009) A new type of troposphere zenith path delay product of the international GNSS service. J Geodesy 83:367–373. https://doi.org/10.1007/s00190-008-0288-8

Chapman S (1959) The International Geophysical Year. EOS Trans Am Geophys Union 40(2):112–119

Chartier AT, Mitchell CN, Miller ES (2018) Annual occurrence rates of ionospheric polar cap patches observed using swarm. J Geophys Res Space Phys 123:2327–2335. https://doi.org/10.1002/2017JA024811

Chen CH, Lin CH, Matsuo T, Chen WH, Lee IT, Liu JY, Lin JT, Hsu CT (2016) Ionospheric data assimilation with thermosphere-ionosphere-electrodynamics general circulation model and GPS-TEC during geomagnetic storm conditions. J Geophys Res Space Phys 121:5708–5722. https://doi.org/10.1002/2015JA021787

Cherniak I, Zakharenkova I, Redmon RJ (2015) Dynamics of the high-latitude ionospheric irregularities during the 17 March 2015 St. Patrick's Day Storm: ground-based GPS measurements. Space Weather 13:585–597. https://doi.org/10.1002/2015SW001237

Cherniak I, Zakharenkova I (2016) High-latitude ionospheric irregularities: differences between ground- and space-based GPS measurements during the 2015 St. Patrick's Day Storm. Planets Space Earth 68:136. https://doi.org/10.1186/s40623-016-0506-1

Cherniak I, Zakharenkova I (2017) New advantages of the combined GPS and GLONASS observations for high-latitude ionospheric irregularities monitoring: case study of June 2015 geomagnetic storm Earth. Planets and Space 69(1):66

Chisham G, Lester M, Milan SE, Freeman MP, Bristow WA, Grocott A, McWilliams KA, Ruohoniemi JM, Yeoman TK, Dyson PL, Greenwald RA (2007) A decade of the Super Dual Auroral Radar Network (SuperDARN): scientific achievements, new techniques and future directions. Surv Geophys 28(1):33–109

Clauer CR, Kim H, Deshpande K, Xu Z, Weimer D, Musko S et al (2014) An autonomous adaptive low-power instrument platform (AAL-PIP) for remote high-latitude geospace data collection. Geosci Instrum Methods Data Syst 3:211–227. https://doi.org/10.5194/gi-3-211-2014

Clilverd MA, Rodger CJ, Thomson NR, Brundell JB, Ulich T, Lichtenberger J et al (2009) Remote sensing space weather events: Antarctic-Arctic radiation-belt (dynamic) deposition-VLF atmospheric research konsortium network. Space Weather 7(4):1–15

Connors M, Schofield I, Reiter K, Chi PJ, Rowe KM, Russell CT (2016) The AUTUMNX magnetometer meridian chain in Québec, Canada. Earth Planets Space. https://doi.org/10.1186/s40623-015-0354-4

Correia E, Kaufmann P, Raulin JP, Bertoni F, Gavilan HR (2011) Analysis of daytime ionosphere behavior between 2004 and 2008 in Antarctica. J Atmos Solar Terr Phys 73(16):2272–2278. https://doi.org/10.1016/j.jastp.2011.06.008

Correia E, Junqueira Paz A, Gende MA (2013a) Characterization of GPS total electron content (GPS-TEC) in Antarctica from 2004 to 2011, Annals Of Geophysics; 56(2):4–2013a, 1–5, https://www.annalsofgeophysics.eu/index.php/annals/article/view/6223

Correia E, Raulin JP, Kaufmann P, Bertoni F, Quevedo MT (2013b) Inter-hemispheric analysis of daytime low ionosphere behavior from 2007 to 2011. J Atmos Solar Terr Phys 92:51–58. https://doi.org/10.1016/j.jastp.2012.09.006

Correia E, Spogli L, Alfonsi L, Cesaroni C, Gulisano AM, Thomas EG et al. (2017) Ionospheric F-region response to the 26 September 2011 geomagnetic storm in the Antarctica American and Australian sectors. In Annales Geophysicae

Correia E, Raunheitte LTM, Bageston JV, D'Amico DE (2020) Characterization of gravity waves in the lower ionosphere using very low frequency observations at Comandante Ferraz Brazilian Antarctic Station. Ann Geophys 38:385–394. https://doi.org/10.5194/angeo-38-385-2020

Cresswell-Moorcock K, Rodger CJ, Clilverd MA, Milling DK (2015) Techniques to determine the quiet day curve for a long period of subionospheric VLF observations. Radio Sci 50(5):453–468

Cully CM, Chaddock D, Daniel C, Davis E, Galts D, McGuffin N, Quinn C, Sheldon A, and Wilson C (2014) Early results on energetic particle precipitation observed by the ABOVE instrument array (Abstract SA13B-3997). Paper presented at 2014 Fall Meeting, AGU, San Francisco, CA

D'Angelo G, Piersanti M, Alfonsi L, Spogli L, Coco I, Li G, Baiqi N (2018a) The response of high latitude ionosphere to the 2015 June 22 storm. Ann Geophy. https://doi.org/10.4401/ag-7780

D'Angelo G, Piersanti M, Alfonsi L, Spogli L, Clausen LBN, Coco I et al (2018b) The response of high latitude ionosphere to the 2015 St. Patrick's day storm from in situ and ground based observations. Adv Space Res 62(3):638–650

D'Angelo G, Piersanti M, Pignalberi A, Coco I, De Michelis P, Tozzi R, Pezzopane M, Alfonsi L, Cilliers P, Ubertini P (2021) Investigation of the physical processes involved in GNSS amplitude scintillations at high latitude: a case study. Remote Sens 13:2493. https://doi.org/10.3390/rs13132493

Danilov AD, Lastovicka J (2001) Effects of geomagnetic storms on the ionosphere and atmosphere. Int J Geomagn Aeron 2(3):209–224

Davila JM, Gopalswamy N, Thompson BJ (2006). Preparing for the International Heliophysical Year (IHY) 2007. In ILWS Workshop, pp 19–24 (https://cdaw.gsfc.nasa.gov/publications/ilws_goa2006/231_Davila.pdf)

De Franceschi G, Alfonsi L, Romano V (2006) Isacco: an Italian project to monitor the high latitude ionosphere by means of GPS receivers. GPS Solut. https://doi.org/10.1007/S10291-006-0036-6

De Franceschi G, Alfonsi L, Romano V, Aquino M, Dodson A, Mitchell CN, Spencer P, Wernik AW (2008) Dynamics of high-latitude patches and associated small-scale irregularities during the October and November 2003 storms. J Atmos Solar-Terr Phys 70(6):879–888

De Franceschi G, Spogli L, Alfonsi L, Romano V, Cesaroni C, Hunstad I (2019) The ionospheric irregularities climatology over Svalbard from solar cycle 23. Sci Rep 9(1):1–14

Dee DP, Uppala SM, Simmons AJ, Berrisford P, Poli P, Kobayashi S, Andrae U, Balmaseda MA, Balsamo G, Bauer P, Bechtold P, Beljaars ACM, van de Berg L, Bidlot J, Bormann N, Delsol C, Dragani R, Fuentes M, Geer AJ, Haimberger L, Healy SB, Hersbach H, Hólm EV, Isaksen L, Kållberg P, Köhler M, Matricardi M, McNally AP, Monge-Sanz BM, Morcrette JJ, Park BK, Peubey C, de Rosnay P, Tavolato C, Thépaut JN, Vitart F (2011) The ERA-Interim reanalysis: configuration and performance of the data assimilation system. Q.J.R. Meteorol Soc 137:553–597

Di Mauro D, Cafarella L, Lepidi S, Pietrolungo M, Alfonsi L, Chambodut A (2014) Geomagnetic polar observatories: the role of Concordia station at Dome C, Antarctica. Ann Geophys. https://doi.org/10.4401/ag-6605

Dimmock AP, Rosenqvist L, Welling DT, Viljanen A, Honkonen I, Boynton RJ, Yordanova E (2020) On the regional variability of dB/dt and its significance to GIC. Space Weather 18:e2020SW002497. https://doi.org/10.1029/2020SW002497

Ding F, Wan W, Ning B, Wang M (2007) Large-scale traveling ionospheric disturbances observed by GPS total electron content during the magnetic storm of 29–30 October 2003. J Geophys Res Space Phys, 112(A6)

Donovan E, Trondsen T, Cogger L, Jackel B (2003) Auroral imaging within the Canadian CANOPUS and NORSTAR projects. Sodankyla Geophys Obs Publ 92:109–112

Dougherty JP, Farley DT (1961) A theory of incoherent scattering of radio waves by a plasma. Proc Royal Soc London Series A Math Phys Sci 259(1296):79–99

Dow JM, Neilan RE, Rizos C (2009) The international GNSS service in a changing landscape of global navigation satellite systems. J Geodesy 83(3–4):191–198

Engebretson MJ, Hughes WJ, Alford JL, Zesta E, Cahill LJ Jr, Arnoldy RL, Reeves GD (1995) Magnetometer array for cusp and cleft studies observations of the spatial extent of broadband ULF magnetic pulsations at cusp/cleft latitudes. J Geophys Res 100(A10):19371–19386. https://doi.org/10.1029/95JA00768

Engebretson MJ, Araki T, Arnoldy RL, Carpenter DL, Doolittle JH, Fukunishi H et al (1997) The United States automatic geophysical observatory (AGO) program in Antarctica. In: Lockwood M, Wild MN, Opgenoorth HJ (eds) The satellite-ground based coordination sourcebook, ESA-SP-1198. ESA Publications, ESTEC, Noordwijk, Netherlands, pp 65–99

Engebretson MJ, Kirkevold KR, Steinmetz ES, Pilipenko VA, Moldwin MB, McCuen BA et al (2020) Interhemispheric comparisons of large nighttime magnetic perturbation events relevant to GICs. J Geophys Res Space Phys 125:e2020JA028128. https://doi.org/10.1029/2020JA028128

Engebretson MJ, Ahmed LY, Pilipenko VA, Steinmetz ES, Moldwin MB et al (2021) Superposed Epoch analysis of nighttime magnetic perturbation events observed in Arctic Canada. J Geophys Res Space Phys Space 126:e2021JA029465. https://doi.org/10.1029/2021JA029465

Enell CF, Verronen PT, Beharrell MJ, Vierinen JH, Kero A, Seppälä A, Honary F, Ulich T, Turunen E (2008) Case study of the mesospheric and lower thermospheric effects of solar x-ray flares: coupled Ion-neutral modelling and comparison with EISCAT and riometer measurements. Ann Geophys 26:2311–2321

Enell CF, Kozlovsky A, Turunen T, Ulich T, Välitalo S, Scotto C, Pezzopane M (2016) Comparison between manual scaling and Autoscala automatic scaling applied to Sodankylä Geophysical Observatory ionograms. Geosci Instrum Method Data Syst 5:53–64. https://doi.org/10.5194/gi-5-53-2016

Eymard L (2002) Retrieval of integrated water vapour and cloud liquid water contents. Remote sensing of atmosphere and ocean from space: models. Instruments and Techniques Springer, Dordrecht, pp 89–106

Farley DT, Dougherty JP, Barron DW (1961) A theory of incoherent scattering of radio waves by a plasma II. Scattering in a magnetic field. Proc Royal Soc London Series A Math Phys Sci 263(1313):238–258

Feng HT, Han DS, Chen XC, Liu JJ, Xu ZH (2020) Interhemispheric conjugacy of concurrent onset and poleward traveling geomagnetic responses for throat aurora observed under quiet solar wind conditions. J Geophys Res Space Phys 125(8):e2020JA027995

Fiori RAD, Danskin DW (2016) Examination of the relationship between riometer-derived absorption and the integral proton flux in the context of modeling polar cap absorption. Space Weather 14:1032–1052. https://doi.org/10.1002/2016SW001461

Folkestad K, Hagfors T, Westerlund S (1983) EISCAT: an updated description of technical characteristics and operational capabilities. Radio Sci 18(6):867–879

Foster JC (1993) Storm-time plasma transport at middle and high latitudes. J Geophys Res 98:1675–1689

Foster JC, Coster AJ, Erickson PJ, Holt JM, Lind FD, Rideout W, McCready M, Van Eyken A, Barnes RJ, Greenwald RA, Rich FJ (2005) Multiradar observations of the polar tongue of ionization. J Geophys Res Space Phys, 110(A9)

Foster JC, Erickson PJ, Coster AJ, Thaller S, Tao J, Wygant JR, Bonnell JW (2014) Storm time observations of plasmasphere erosion flux in the magnetosphere and ionosphere. Geophys Res Lett 41:762–768. https://doi.org/10.1002/2013GL059124

Foster JC, Zou S, Heelis RA, Erickson PJ (2021) Ionospheric Storm-Enhanced Density Plumes. In: Huang C, Lu G, Zhang Y, Paxton LJ (eds), Ionosphere Dynamics and Applications. https://doi.org/10.1002/9781119815617.ch6

Francia P, De Lauretis M, Vellante M, Villante U, Piancatelli A (2009) ULF geomagnetic pulsations at different latitudes in Antarctica. Ann Geophys 27:3621–3629. https://doi.org/10.5194/angeo-27-3621-2009

Fremouw EJ, Leadabrand RL, Livingston RC, Cousins MD, Rino CL, Fair BC, Long RA (1978) Early results from the DNA Wideband satellite experiment—Complex-signal scintillation. Radio Sci 13(1):167–187

Fremouw EJ, Secan JA (1984) Modeling and scientific application of scintillation results. Radio Sci 19:687–694

Fukuyama K, Kofman W (1980) Incoherent scattering of an electromagnetic wave in the mesosphere: a theoretical consideration. J Geomagn Geoelectr 32(2):67–81

Fuller-Rowell TJ, Codrescu MV, Moffett RJ, Quegan S (1994) Response of the thermosphere and ionosphere to geomagnetic storms. J Geophys Res Space Physics 99(A3):3893–3914

Ghaffari R, Cully CM, Turner DL, Reeves GD (2020) Characteristics of electron precipitation during 40 energetic electron injections inferred via subionospheric VLF signal propagation. J Geophys Res Space Phys 125:e2019JA027233. https://doi.org/10.1029/2019JA027233

Ghobadi H, Spogli L, Alfonsi L, Cesaroni C, Cicone A, Linty N, Romano V, Cafaro M (2020) Disentangling ionospheric refraction and diffraction effects in GNSS raw phase through fast iterative filtering technique. GPS Solut 24(3):1–13

Ghoddousi-Fard R, Héroux P, Danskin D, Boteler D (2011) Developing a GPS TEC mapping service over Canada. Space Weather 9:S06D11. https://doi.org/10.1029/2010SW000621

Ghoddousi-Fard R (2014) "GPS ionospheric mapping at Natural Resources Canada". IGS Workshop 2014, June 23-27, 2014, Pasadena, California, USA

Gillies RG, van Eyken A, Spanswick E, Nicolls M, Kelly J, Greffen M, Knudsen D, Connors M, Schutzer M, Valentic T, Malone M (2016) First observations from the RISR-C incoherent scatter radar. Radio Sci 51(10):1645–1659

Gjerloev JW (2009) A global ground-based magnetometer initiative. EOS Trans Am Geophys Union 90(27):230–231

Gordon WE (1958) Incoherent scattering of radio waves by free electrons with applications to space exploration by radar. Proc IRE 46(11):1824–1829

Grandin M, Aikio AT, Kozlovsky A, Ulich T, Raita T (2017a) Cosmic radio noise absorption in the high latitude ionosphere during solar wind high speed streams. J Geophys Res Space Physics 122:5203–5223. https://doi.org/10.1002/2017JA023923

Grandin M, Kero A, Partamies N, McKay D, Whiter D, Kozlovsky A, Miyoshi Y (2017b) Observation of pulsating aurora signatures in cosmic noise absorption data. Geophys Res Lett 44:5292–5300. https://doi.org/10.1002/2017GL073901

Greenwald RA, Baker KB, Dudeney JR, Pinnock M, Jones TB, Thomas EC, Villain JP, Cerisier JC, Senior C, Hanuise C, Hunsucker RD (1995) Darn/superdarn. Space Sci Rev 71(1–4):761–796

Greenwald RA (2021) History of the super dual auroral radar network (SuperDARN)-I: pre-SuperDARN developments in high frequency radar technology for ionospheric research and selected scientific results. Hist Geo Space Sci 12(77–93):2021. https://doi.org/10.5194/hgss-12-77-2021

Grocott A, Cowley SWH, Sigwarth JB, Watermann JF, Yeoman TK (2002) Excitation of twin-vortex flow in the nightside high-latitude ionosphere during an isolated substorm. Ann Geophys 20(10):1577–1601. https://doi.org/10.5194/angeo-20-1577-2002

Gustavsson B (2000) Three Dimensional Imaging of Aurora and Airglow, PhD thesis, IRF Scientific Report 267, Swedish Institute of Space Physics, Kiruna, Sweden, ISBN:91–7191–878–7

Ham YB, Jee G, Lee C, Kwon HJ, Kim JH, Zabotin N, Bullett T (2020) Observations of the polar ionosphere by the vertical incidence pulsed ionospheric radar at jang Bogo Station, Antarctica. J Astron Space Sci. https://doi.org/10.5140/JASS.2020.37.2.143

Heino E, Verronen PT, Kero A, Kalakoski N, Partamies N (2019) Cosmic noise absorption during solar proton events in WACCM-D and riometer observations. J Geophys Res Space Phys 124(2):1361–1376

Heino E, Partamies N (2020) Observational validation of cutoff models as boundaries of solar proton event impact area. J Geophys Res Space Phys 125:e2020JA027935. https://doi.org/10.1029/2020JA027935

Herring TA, King RW, Floyd MA, McClusky SC (2018) Introduction to GAMIT/GLOBK Introduction to GAMIT/GLOBK Release 10.7, Department of Earth, Atmospheric, and Planetary Sciences Massachusetts Institute of Technology

Hocke K, Schlegel K (1996) A review of atmospheric gravity waves and travelling ionospheric disturbances: 1982–1995. Ann Geophys 14(9):917

Holzworth RH, Meng C-I (1975) Mathematical representation of the auroral oval. Geophys Res Lett 2:377

Huang CS, Murr D, Sofko GJ, Hughes WJ, Moretto T (2000) Ionospheric convection response to changes of interplanetary magnetic field B z component during strong B y component. J Geophys Res 105:5231–5243

Huang CS, Foster JC, Kelley MC (2005) Long-duration penetration of the interplanetary electric field to the low-latitude ionosphere during the main phase of magnetic storms. J Geophys Res Space 110:A11309. https://doi.org/10.1029/2005JA011202

Huba JD, Sazykin S, Coster A (2017) SAMI3-RCM simulation of the 17 March 2015 geomagnetic storm: SAMI3-RCM MARCH 2015 STORM. J Geophys Res Space Phys 122(1):1246–1257. https://doi.org/10.1002/2016JA023341

Imber SM, Milan SE, Hubert B (2006) The auroral and ionospheric flow signatures of dual lobe reconnection. Ann Geophys 24(11):3115–3129

Imber SM, Milan SE, Lester M (2013) The Heppner-Maynard Boundary measured by SuperDARN as a proxy for the latitude of the auroral oval. J Geophys Res Space Phys. https://doi.org/10.1029/2012JA018222

Jacobsen KS, Andalsvik YL (2016) Overview of the 2015 St. Patrick's day storm and its consequences for RTK and PPP positioning in Norway. J Space Weather Space Clim 6:A9. https://doi.org/10.1051/swsc/2016004

Jayachandran PT, Langley RB, MacDougall JW, Mushini SC, Pokhotelov D, Hamza AM, Mann IR, Milling DK, Kale ZC, Chadwick R, Kelly T (2009) Canadian high arctic ionospheric network (CHAIN). Radio Sci 44(01):1–10

Jee G, Ham YB, Choi Y, Kim E, Lee C, Kwon H et al (2021) Observations of the aurora by visible all-sky camera at Jang Bogo Station, Antarctica. J Astron Space Sci 38(4):203–215. https://doi.org/10.5140/JASS.2021.38.4.203

Jenkins B, Jarvis MJ (1999) Mesospheric winds derived from SuperDARN HF radar meteor echoes at Halley, Antarctica. Earth Planets Space 51(7–8):685–689

Jiao Y, Morton Y, Taylor S, Pelgrum W (2013) Characterization of high latitude ionospheric scintillation of GPS signals. Radio Sci. https://doi.org/10.1002/2013RS005259

Jiao Y, Hall JJ, Morton YT (2017a) Automatic equatorial GPS amplitude scintillation detection using a machine learning algorithm. IEEE Trans Aerosp Electron Syst 53(1):405–418

Jiao Y, Hall JJ, Morton YT (2017) Performance evaluation of an automatic GPS ionospheric phase scintillation detector using a machine-learning algorithm. NAVIGATION J Inst Navigat 64(3):391–402

Jin Y, Spicher A, Xiong C, Clausen LBN, Kervalishvili G, Stolle C, Miloch WJ (2019) Ionospheric plasma irregularities characterized by the Swarm satellites: statistics at high latitudes. J Geophys Res Space Phys 124:1262–1282. https://doi.org/10.1029/2018JA026063

Jiao Y, Morton YT (2015) Comparison of the effect of high-latitude and equatorial ionospheric scintillation on GPS signals during the maximum of solar cycle 24. Radio Sci 50(9):886–903

Jin Y, Xiong C (2020) Interhemispheric asymmetry of large-scale electron density gradients in the polar cap ionosphere: UT and seasonal variations. J Geophys Res Space Phys 125:e2019JA027601. https://doi.org/10.1029/2019JA027601

Juusola L, Archer WE, Kauristie K, Burchill JK, Vanhamäki H, Aikio AT (2016) Ionospheric conductances and current of a morning sector auroral arc from Swarm-A electric and magnetic field measurements. Geophys Res Lett 43:11519–11527. https://doi.org/10.1002/2016GL070248

Kadokura A, Yamagishi H, Sato N, Nakano K, Rose MC (2008) Unmanned magnetometer network observation in the 44th Japanese Antarctic Research Expedition: initial results and an event study on auroral substorm evolution. Polar Sci 2:223–235. https://doi.org/10.1016/j.polar.2008.04.002

Kamide Y, Kusano K (2015) No major solar flares but the largest geomagnetic storm in the present solar cycle. Space Weather 13:365–367. https://doi.org/10.1002/2015SW001213

Kasahara Y, Kasaba Y, Kojima H, Yagitani S, Ishisaka K, Kumamoto A et al (2018) The plasma wave experiment (PWE) on board the Arase (ERG) satellite. Earth Planets Space 70(1):86. https://doi.org/10.1186/s40623-018-0842-4

Kataoka RD, Shiota D, Kilpua E, Keika K (2015) Pileup accident hypothesis of magnetic storm on 17 March 2015. Geophys Res Lett 42:5155–5161. https://doi.org/10.1002/2015GL064816

Kauristie K, Myllys M, Partamies N, Viljanen A, Peitso P, Juusola L, Ahmadzai S, Singh V, Keil R, Martinez U, Luginin A, Glover A, Navarro V, Raita T (2016) Forecasting auroras from regional and global magnetic field measurements. Geosci Instrum Methods Data Syst 5(1):253–262. https://doi.org/10.5194/gi-5-253-2016

Kellerman AC, Shprits YY, Makarevich RA, Spanswick E, Donovan E, Reeves G (2015) Characterization of the energy-dependent response of riometer absorption. J Geophys Res Space Phys 120(1):615–631

Kennicutt M, Chown S, Cassano J et al (2014) Polar research: six priorities for Antarctic science. Nature 512:23–25. https://doi.org/10.1038/512023a

Kero A, Vierinen J, McKay-Bukowski D, Enell CF, Sinor M, Roininen L, Ogawa Y (2014) Ionospheric electron density profiles inverted from a spectral riometer measurement. Geophys Res Lett 41(15):5370–5375

Kilpua E, Juusola L, Grandin M, Kero A, Dubyagin S, Partamies N, Osmane A, George H, Kalliokoski M, Raita T, Asikainen T (2020) Cosmic noise absorption signature of particle precipitation during interplanetary coronal mass ejection sheaths and ejecta. Ann Geophys 38(2):557–574

Kim, H. (2021) Interhemispheric asymmetries in high-latitude magnetosphere-ionosphere coupling processes. Bull Am Phys Soc, 66

Koustov AV, Ullrich S, Ponomarenko PV, Gillies RG, Themens DR, Nishitani N (2020) Comparison of SuperDARN peak electron density estimates based on elevation angle measurements to ionosonde and incoherent scatter radar measurements. Earth Planets Space. https://doi.org/10.1186/s40623-020-01170-w

Kozlovsky A, Turunen T, Ulich T (2013) Rapid-run ionosonde observations of traveling ionospheric disturbances in the auroral ionosphere. J Geophys Res Space Phys 118:5265–5276. https://doi.org/10.1002/jgra.50474

Kozlovsky A, Shalimov S, Kero J, Raita T, Lester M (2018) Multi-instrumental observations of nonunderdense meteor trails. J Geophys Res Space Phys 123:5974–5989. https://doi.org/10.1029/2018JA025405

Koronczay D, Lichtenberger J, Clilverd MA, Rodger CJ, Lotz SI, Sannikov DV et al (2019) The source regions of whistlers. J Geophys Res Space Phys 124:5082–5096. https://doi.org/10.1029/2019JA026559

Krupnik I, Allison I, Bell R, Cutler P, Hik D, Lopez-Martinez J, Rachold V, Sarukhanian E, Summerhayes C (2011) Understanding Earth's Polar Challenges: International Polar Year 2007–2008-Summary by the IPY Joint Committee (http://www.cn-scar.es/pdf/IPY-JC-Summary-Full.pdf)

Krüger K, Naujokat B, Labitzke K (2005) The unusual midwinter warming in the Southern Hemisphere stratosphere 2002: A comparison to Northern Hemisphere phenomena. J Atmos Sci 62(3):603–613

Kuo CC, Staelin DH, Rosenkranz PW (1994) Statistical iterative scheme for estimating atmospheric relative humidity profiles. IEEE Trans Geosci Remote Sens 32(2):254–260

Kwon HJ, Lee C, Jee G, Ham Y, Kim JH, Kim YH et al (2018) Ground-based observations of the polar region space environment at the Jang Bogo Station, Antarctica. J Astron Space Sci 35(3):185–193. https://doi.org/10.5140/jass.2018.35.3.185

Kwon HJ, Kim KH, Jee G, Seon J, Lee C, Ham YB et al (2022) Disappearance of the polar cap ionosphere during geomagnetic storm on 11 May 2019. Space Weather. https://doi.org/10.1029/2022SW003054

Lanzerotti LJ, Wolfe A, Trivedi N, Maclennan CG, Medford LV (1990) Magnetic impulse events at high latitudes: magnetopause and boundary layer plasma processes. J Geophys Res 95:97–107. https://doi.org/10.1029/JA095iA01p00097

Laštovička J (2017) A review of recent progress in trends in the upper atmosphere. J Atmos Solar Terr Phys 163:2–13

Lee C, Jee G, Wu Q, Shim JS, Murphy D, Song IS, Kwon HJ, Kim JH, Kim YH (2017) Polar thermospheric winds and temperature observed by Fabry-Perot interferometer at Jang Bogo station, Antarctica. J Geophys Res-Space 122(9):9685–9695. https://doi.org/10.1002/2017ja024408

Lester M (2013) The super dual auroral radar network (SuperDARN): an overview of its development and science. Adv Polar Sci 24(1):1–11. https://doi.org/10.3724/SP.J.1085.2013.00001

Lichtenberger J, Ferencz C, Bodnár L, Hamar D, Steinbach P (2008) Automatic whistler detector and analyzer system: automatic whistler detector. J Geophys Res Space Phys, 113(A12)

Linty N, Minetto A, Dovis F, Spogli L (2018) Effects of phase scintillation on the GNSS positioning error during the September 2017 storm at Svalbard. Space Weather 16:1317–1329. https://doi.org/10.1029/2018SW001940

Liu J, Wang W, Burns A, Solomon SC, Zhang S, Zhang Y, Huang C (2016) Relative importance of horizontal and vertical transports to the formation of ionospheric storm-enhanced density and polar tongue of ionization. J Geophys Res Space Phys 121:8121–8133. https://doi.org/10.1002/2016JA022882

Lotz SI, Clilverd M (2019) Demonstrating the use of a class of min-max smoothers for D region event detection in narrow band VLF phase. Radio Sci 54(3):233–244

Love JJ, Chulliat A (2013) An international network of magnetic observatories. EOS Trans Am Geophys Union 94(42):373–374

Lukianova R, Kozlovsky A, Shalimov S, Ulich T, Lester M (2015) Thermal and dynamical perturbations in the winter polar mesosphere-lower thermosphere region associated with sudden stratospheric warmings under conditions of low solar activity. J Geophys Res Space Phys 120(6):5226–5240

Lyons LR, Gallardo-Lacourt B, Zou S, Weygand JM, Nishimura Y, Li W et al (2016) The 17 March 2013 storm: synergy of observations related to electric field modes and their ionospheric and magnetospheric effects. J Geophys Res Space Phys 121(11):10–880

MacDougall JK, Jayachandran PT (2005) Sporadic E at cusp latitudes. J Atm Solar-Terr Phys. https://doi.org/10.1016/j.jastp.2005.07.011

Macho EP, Correia E, Paulo CM, Angulo L, Vieira JAG (2020) Ionospheric response to the June 2015 geomagnetic storm in the South American region. Adv Sp Res 65(9):2172–2183. https://doi.org/10.1016/j.asr.2020.02.025

Macotela EL, Němec F, Manninen J, Santolík O, Kolmašová I, Turunen T (2019) VLF emissions with banded structure in the 16- to 39-kHz frequency range measured by a high-latitude ground-based receiver. Geophys Res Lett 46:14214–14222. https://doi.org/10.1029/2019GL086127

Mann IR, Milling DK, Rae IJ, Ozeke LG, Kale A, Kale ZC et al (2008) The upgraded CARISMA magnetometer array in the THEMIS era. Space Sci Rev 141(1–4):413–451. https://doi.org/10.1007/s11214-008-9457-6

Manninen J, Turunen T, Kleimenova N, Rycroft M, Gromova L, Sirviö I (2016) Unusually high frequency natural VLF radio emissions observed during daytime in Northern Finland. Environ Res Lett 11(12):124006

Mannucci AJ, Wilson BD, Edwards CD (1993) A new method for monitoring the Earth ionosphere total electron content using the GPS global network, In: Proceedings of ION GPS-93, pp 1323–1332

Mannucci AJ, Tsurutani BT, Abdu MA, Gonzalez WD, Komjathy A, Echer E, Iijima BA, Crowley G, Anderson D (2008) Superposed epoch analysis of the dayside ionospheric response to four intense geomagnetic storms. J Geophys Res-Space 113:A00A02. https://doi.org/10.1029/2007JA012732

Mansilla GA (2018) Ionospheric response to the magnetic storm of 22 June 2015. Pure Appl Geophys 175(3):1139–1153

Marcucci MF, Coco I, Ambrosino D, Amata E, Milan SE, Bavassano Cattaneo MB, Retinò A (2008) Extended SuperDARN and IMAGE observations for northward IMF: evidence for dual lobe reconnection. J Geophys Res 113:A02204. https://doi.org/10.1029/2007JA012466

McCaffrey AM, Jayachandran PT (2019) Determination of the refractive contribution to GPS phase "Scintillation." J Geophys Res Space Phys. https://doi.org/10.1029/2018JA025759

McComas DJ, Bame SJ, Barker P, Feldman WC, Phillips JL, Riley P, Griffee JW (1998) Solar wind electron proton alpha monitor (SWEPAM) for the advanced composition explorer. Space Sci Rev 86(1):563–612

McCrea I, Aikio A, Alfonsi L, Belova E, Buchert S, Clilverd M, Engler N, Gustavsson B, Heinselman C, Kero J, Kosch M (2015) The science case for the EISCAT_3D radar. Prog Earth Planet Sci 2(1):21

McKay-Bukowski D, Vierinen J, Virtanen II, Fallows R, Postila M, Ulich T, Wucknitz O, Brentjens M, Ebbendorf N, Enell C, Gerbers M, Grit T, Gruppen P, Kero A, Iinatti T, Lehtinen M, Meulman H, Norden M, Orispää M, Raita T, de Reijer JP, Roininen L, Schoenmakers A, Stuurwold K, Turunen E (2015) KAIRA: the Kilpisjärvi atmospheric imaging receiver array—system overview and first results. IEEE T Geosci Remote Sens 53:1440–1451. https://doi.org/10.1109/TGRS.2014.2342252

Mende S, Harris S, Frey H, Angelopoulos V, Russell C, Donovan E, Jackel B, Greffen M, Peticolas L (2008) The THEMIS array of ground-based observatories for the study of auroral substorms. Space Sci Rev 141:357–387. https://doi.org/10.1007/s11214-008-9380-x

Melsheimer C, Heygster G (2008) Improved retrieval of total water vapor over polar regions from AMSU-B microwave radiometer data. IEEE Trans Geosci Remote Sens 46(8):2307–2322

Miao J, Kunzi K, Heygster G, Lachlan-Cope TA, Turner J (2001) Atmospheric water vapor over Antarctica derived from Special Sensor Microwave/Temperature 2 data. J Geophys Res Atmos 106(D10):10187–10203

Mikhailov AV, Marin D (2001) An interpretation of the foF2 and hmF2 long-term trends in the framework of the geomagnetic control concept. Ann Geophys 19(7):733–748

Milan SE, Lester M, Cowley SWH, Oksavik K, Brittnacher M, Greenwald RA, Sofko G, Villain J-P (2003) Variations in the polar cap area during two substorm cycles. Ann Geophys 21:1121–1140

Milan SE, Provan G, Hubert B (2007) Magnetic flux transport in the Dungey cycle: a survey of dayside and nightside reconnection rates. J Geophys Res Space Phys. https://doi.org/10.1029/2006JA011642

Mitchell CN, Alfonsi L, De Franceschi G, Lester M, Romano V, Wernik AW (2005) GPS TEC and scintillation measurements from the polar ionosphere during the October 2003 storm. Geophys Res Lett. https://doi.org/10.1029/2004gl021644

Miyoshi Y, Shinohara I, Takashima T, Asamura K, Higashio N, Mitani T et al (2018) Geospace exploration project ERG. Earth Planets Space 70(1):101. https://doi.org/10.1186/s40623-018-0862-0

Mushini SC, Jayachandran PT, Langley RB, MacDougall JW, Pokhotelov D (2012) Improved amplitude- and phase-scintillation indices derived from wavelet detrended high-latitude GPS data. GPS Solut 16(3):363–373

Nava B, Coisson P, Radicella SM (2008) A new version of the NeQuick ionosphere electron density model. J Atmos Sol Terr Phys 70:1856–1862. https://doi.org/10.1016/j.jastp.2008.01.01510.1016/j.jastp.2008.01.015

Nava B, Radicella SM, Azpilicueta F (2011) Data ingestion into NeQuick 2. Radio Sci 46:RS0D17. https://doi.org/10.1029/2010RS004635

Neal JJ, Rodger CJ, Clilverd MA, Thomson NR, Raita T, Ulich Th (2015) Long-term determination of energetic electron precipitation into the atmosphere from AARDDVARK subionospheric VLF observations. J Geophys Res 120:2194–2211. https://doi.org/10.1002/2014JA020689

Negusini M, Petkov BH, Tornatore V, Barindelli S, Martelli L, Sarti P, Tomasi C (2021) Water vapour assessment using GNSS and radiosondes over polar regions and estimation of climatological trends from long-term time series analysis. Remote Sens 13:4871. https://doi.org/10.3390/rs13234871

Neudegg DA, Yeoman TK, Cowley SWH, Provan G, Haerendel G, Baumjohann W et al (1999) A flux transfer event observed at the magnetopause by the Equator-S spacecraft and in the ionosphere by the CUTLASS HF radar. Ann Geophys 17(6):707–711

Neudegg DA, Fraser BJ, Menk FW, Burns GB, Morris RJ, Underwood MJ (2002) Magnetospheric sources of Pc1–2 ULF waves in the polar ionospheric waveguide. Antarct Sci 14(1):93–103. https://doi.org/10.1017/s0954102002000627

Nikitina L, Trichtchenko L, Boteler DH (2016) Assessment of extreme values in geomagnetic and geoelectric field variations for Canada. Space Weather 14(7):481–494

Nishida A (1968) Coherence of geomagnetic DP2 fluctuations with interplanetary magnetic variations. J Geophys Res-Space 73:5549–5559

Nishitani N, Ruohoniemi JM, Lester M, Baker JBH, Koustov AV, Shepherd SG, Chisham G, Hori T, Thomas EG, Makarevich RA, Marchaudon A (2019) Review of the accomplishments of mid-latitude super dual auroral radar network (SuperDARN) HF radars. Prog Earth Planet Sci 6(1):1–57

Niu F, Morton Y, Wang J, PelgrumW (2012) GPS carrier phase detrending methods and performances for ionosphere scintillation studies," Proc. ION ITM, Newport Beach, CA

Noja M, Stolle C, Park J, Lühr H (2013) Long-term analysis of ionospheric polar patches based on CHAMP TEC data. Radio Sci 48:289–301. https://doi.org/10.1002/rds.20033

Obana Y, Maruyama N, Shinbori A, Hashimoto KK, Fedrizzi M, Nosé M et al (2019) Response of the ionosphere-plasmasphere coupling to the September 2017 storm: what erodes the plasmasphere so severely? Space Weather 17:861–876. https://doi.org/10.1029/2019SW002168

Ogawa T, Nishitani N, Sato N, Yamagishi H, Yukimatu AS (2002) Upper mesosphere summer echoes detected with the Antarctic Syowa HF radar. Geophys Res Lett. https://doi.org/10.1029/2001GL014094

Ogunmodimu O, Honary F, Rogers N, Falayi EO, Bolaji OS (2018) Solar flare induced cosmic noise absorption. NRIAG J Astron Geophy 7(1):31–39. https://doi.org/10.1016/j.nrjag.2018.03.002

Oyama S, Watkins BJ (2011) Generation of atmospheric gravity waves in the polar thermosphere in response to auroral activity. Space Sci Rev 168(1–4):463–473. https://doi.org/10.1007/s11214-011-9847-z

Palm M, Melsheimer C, Schrems O (2010) Integrated water vapour above Ny–Ålesund, Spitsbergen: a multi–sensor intercomparison. Atmos Chem Phys 10:1–12

Pancheva D, Mitchell NJ, Hagan ME, Manson AH, Meek CE, Luo Y, Jacobi C, Kürschner D, Clark RR, Hocking WK, MacDougall J (2002) Global-scale tidal structure in the mesosphere and lower thermosphere during the PSMOS campaign of June–August 1999 and comparisons with the global-scale wave model. J Atmos Solar-Terr Phys 64(8–11):1011–1035. https://doi.org/10.1016/S1364-6826(02)00054-8

Parracho AC, Bock O, Bastin S (2018) Global IWV trends and variability in atmospheric reanalyses and GPS observations. Atmos Chem Phys 18(22):16213–16237

Partamies N, Whiter D, Syrjäsuo M, Kauristie K (2014) Solar cycle and diurnal dependence of auroral structures. J Geophys Res 119:8448–8461. https://doi.org/10.1002/2013JA019631

Pettigrew ED, Shepherd SG, Ruohoniemi JM (2010) Climatological patterns of high-latitude convection in the Northern and Southern Hemispheres: dipole tilt dependencies and interhemispheric comparisons. J Geophys Res 115:A07305. https://doi.org/10.1029/2009JA014956

Peng S, Morton Y (2013) A USRP2-based reconfigurable multi-constellation multi-frequency GNSS software receiver front end. GPS Solut 17(1):89–102

Perrone L, De Franceschi G (1998) Solar, ionospheric and geomagnetic indices. Ann Geophys 41:5–6

Pezzopane M, Del Corpo A, Piersanti M, Cesaroni C, Pignalberi A, Di Matteo S, Spogli L, Vellante M, Heilig B (2019) On some features characterizing the plasmasphere–magnetosphere–ionosphere system during the geomagnetic storm of 27 May 2017. Earth Planets Space. https://doi.org/10.1186/s40623-019-1056-0

Picone JM, Hedin AE, Drob DP, Aikin AC (2002) NRLMSISE-00 empirical model of the atmosphere: Statistical comparisons and scientific issues. J Geophys Res Space Phys 107(A12):SIA-15

Pilipenko VA, Engebretson MJ (2002) Ground images at high latitudes of ULF wave processes in the outer magnetosphere. J Atmos Solar-Terr Phys 64(2):183–201. https://doi.org/10.1016/s1364-6826(01)00083-9

Piersanti M, De Michelis P, Del Moro D, Tozzi R, Pezzopane M, Consolini G, Marcucci MF et al (2020) From the sun to earth: effects of the 25 August 2018 geomagnetic storm. Ann Geophys 38(3):703–724

Pinnock M, Chisham G, Coleman IJ, Freeman MP, Hairston M, Villain JP (2003) The location and rate of dayside reconnection during an interval of southward interplanetary magnetic field. Ann Geophys 21:1467–1482

Potapov A, Guglielmi A, Tsegmed B, Kultima J (2006) Global Pc5 event during 29–31 October 2003 magnetic storm. Adv Space Res 38(8):1582–1586

Prikryl P, Jayachandran PT, Mushini SC, Chadwick R (2011) Climatology of GPS phase scintillation and HF radar backscatter for the high-latitude ionosphere under solar minimum conditions. Ann Geophys 29(2):377–392

Prikryl P, Ghoddousi-Fard R, Weygand JM, Viljanen A, Connors M, Danskin DW et al (2016) GPS phase scintillation at high latitudes during the geomagnetic storm of 17–18 March 2015. J Geophys Res Space Phys 121(10):448–465. https://doi.org/10.1002/2016JA023171

Purohit PK, Bhawre P, Mansoori AA, Khan PA, Gwal AK (2011) GPS derived total electron content (TEC) variations over Indian Antarctic Station, Maitri. World Acad Sci Engin Technol 59:597–599

Radicella SM, Leitinger R (2001) The evolution of the DGR approach to model electron density profiles. Adv Space Res 27:35–40. https://doi.org/10.1016/S0273-1177(00)00138-1

Ranta H, Ranta A (1977) Daily variation of absorption in the D-region using riometer data at high latitudes. J Atmos Terr Phys 39:309–312

Regi M, De Lauretis M, Francia P, Lepidi S, Piancatelli A, Urbini S (2018) The geomagnetic coast effect at two 80° S stations in Antarctica, observed in the ULF range. Ann Geophys 36(1):193–203. https://doi.org/10.5194/angeo-36-193-2018

Reidy JA, Fear RC, Whiter DK, Lanchester B, Kavanagh AJ, Milan SE et al (2018) Interhemispheric survey of polar cap aurora. J Geophys Res Space Phys 123(9):7283–7306

Reinisch BW, Galkin IA, Khmyrov GM, Kozlov AV, Bibl K, Lisysyan IA et al (2009) New Digisonde for research and monitoring applications. Radio Sci 44:RS0A24. https://doi.org/10.1029/2008RS004115

Reinisch BW, Galkin IA (2011) Global ionospheric radio observatory (GIRO). Earth Planets Space 63(4):377–381

Ren J, Zou S, Gillies RG, Donovan E, Varney RH (2018) Statistical characteristics of polar cap patches observed by RISR-C. J Geophys Res Space Phys. https://doi.org/10.1029/2018JA025621

Ren J, Zou S, Lu J, Giertych N, Chen Y, Varney RH, Reimer AS (2020) Statistical study of ion upflow and downflow observed by the Poker Flat Incoherent Scatter Radar (PFISR). J Geophys Res Space Phys 125:e2020JA028179. https://doi.org/10.1029/2020JA028179

Richards PG, Meier RR, Chen SP, Drob D, Dandenault P (2017) Investigation of the causes of the longitudinal variation of the electron density in the Weddell Sea Anomaly. J Geophys Res Space Phys 122(6):6562–6583. https://doi.org/10.1002/2016JA023565

Richardson IG, Cane HV (2010) Near-earth interplanetary coronal mass ejections during solar cycle 23 (1996–2009): catalog and summary of properties. Solar Phys 264(1):189–237. https://doi.org/10.1007/s11207-010-9568-6

Rietveld MT, Wright JW, Zabotin N, Pitteway MLV (2008) The Tromsø dynasonde. Polar Sci 2(1):55–71. https://doi.org/10.1016/j.polar.2008.02.001

Rinke A, Segger B, Crewell S, Maturilli M, Naakka T, Nygård T, Vihma T et al (2019) Trends of vertically integrated water vapor over the Arctic during 1979–2016: consistent moistening all over? J Clim 32(18):6097–6116

Rino C (2011) The theory of scintillation with applications in remote sensing. John Wiley & Sons, Hoboken

Rishbeth H, Williams PJS (1985) The EISCAT ionospheric Radar - The system and its early results. Quart J Royal Astron Soc 26:478–512

Rishbeth H (1990) A greenhouse effect in the ionosphere? Planet Space Sci 38(7):945–948

Roble RG, Ridley EC, Richmond AD, Dickinson RE (1988) A coupled thermosphere/ionosphere general circulation model. Geophys Res Lett 15:1325–1328. https://doi.org/10.1029/GL015i012p01325

Rodger AS, Smith AJ (1989) Antarctic studies of the coupled ionosphere-magnetosphere system. Philos Trans Royal Soc London Series A Math Phys Sci 328(1598):271–287

Rodger CJ, Werner S, Brundell JB, Lay EH, Thomson NR, Holzworth RH, Dowden RL (2006) Detection efficiency of the VLF World-Wide Lightning Location Network (WWLLN): initial case study. Ann Geophys 24(12):3197–3214. https://doi.org/10.5194/angeo-24-3197-2006

Rogers NC, Kero A, Honary F, Verronen PT, Warrington EM, Danskin DW (2016) Improving the twilight model for polar cap absorption nowcasts. Space Weather 14(11):950–972. https://doi.org/10.1002/2016sw001527

Roininen L, Laine M, Ulich T (2015) Time-varying ionosonde trend: case study of Sodankylä hmF2 data 1957–2014. J Geophys Res Space Phys 120(8):6851–6859

Rostoker G, Samson JC, Creutzberg F, Hughes TJ, McDiarmid DR, McNamara AG, Vallance Jones A, Wallis DD, Cogger LL (1995) CANOPUS—A ground-based instrument array for remote sensing the high latitude ionosphere during the ISTP/GGS program. Space Sci Rev 71(1):743–760. https://doi.org/10.1007/BF00751349

Ruohoniemi JM, Baker KB (1998) Large-scale imaging of high-latitude convection with super dual auroral radar network HF radar observations. J Geophys Res Space Phys. https://doi.org/10.1029/98JA01288

Sahai Y, Fagundes PR, Becker-Guedes F, Abalde JR, Crowley G, Pi X et al (2004) Longitudinal differences observed in the ionospheric F-region during the major geomagnetic storm of 31 March 2001. Ann Geophys 22(9):3221–3229

Sandel BR, King RA, Forrester WT, Gallagher DL, Broadfoot AL, Curtis CC (2001) Initial results from the IMAGE extreme ultraviolet imager. Geophys Res Lett 28:1439–1442

Sangalli L, Partamies N, Syrjäsuo M, Enell C-F, Kauristie K, Mäkinen S (2011) Performance study of the new EMCCD-based all-sky cameras for auroral imaging. Int J Remote Sens 32:2987–3003. https://doi.org/10.1080/01431161.2010.541505

Schillings A, Nilsson H, Slapak R, Wintoft P, Yamauchi M, Wik DI, Carr CM (2018) O+ escape during the extreme space weather event of 4–10 September 2017. Space Weather 16(9):1363–1376. https://doi.org/10.1029/2018SW001881

Secan JA, Bussey RM, Fremouw EJ, Basu S (1997) High-latitude upgrade to the Wideband ionospheric scintillation model. Radio Sci 32(4):1567–1574

Shepherd SG, Ruohoniemi JM (2000) Electrostatic potential patterns in the high-latitude ionosphere constrained by SuperDARN measurements. J Geophys Res Space Phys. https://doi.org/10.1029/2000JA000171

Shreedevi PR, Thampi SV, Chakrabarty D, Choudhary RK, Pant TK, Bhardwaj A, Mukherjee S (2016) On the latitudinal changes in ionospheric electrodynamics and composition based on observations over the 76–77°E meridian from both hemispheres during a geomagnetic storm. J Geophys Res Space Phys. https://doi.org/10.1002/2015JA021841

Shreedevi PR, Choudhary RK (2017) Impact of oscillating IMF Bz during 17 March 2013 storm on the distribution of plasma over Indian low-latitude and mid-latitude ionospheric regions. J Geophys Res Space Phys 122:11607–11623. https://doi.org/10.1002/2017JA023980

Shreedevi PR, Choudhary RK, Yu Y, Thomas EG (2019) Morphological study on the ionospheric variability at Bharati, a polar cusp station in the southern hemisphere. J Atmos Solar Terr Phys. https://doi.org/10.1016/j.jastp.2019.105058

Shreedevi PR, Choudhary RK, Thampi SV, Yadav S, Pant TK, Yu Y et al (2020) Geomagnetic storm induced plasma density enhancements in the southern polar ionospheric region: a comparative study using St. Patrick's Day storms of 2013 and 2015. Space Weather 18:e2019SW002383. https://doi.org/10.1029/2019SW002383

Sigernes F, Syrjäsuo,M, Ellingsen PG, Lybekk B, Trondsen E, Clausen L, Moen J, Mattanen J, Kauristie K (2017) Status: the Boreal Aurora Camera Constellation (BACC), http://kho.unis.no/doc/BACC.pdf, Accessed 1 June 2021

Skjæveland AH, Kotova DS, Miloch WJ (2021) Case studies of ionospheric plasma irregularities over Queen Maud Land, Antarctica. J Geophys Res Space Phys 126(10):e2021JA029963

Smith AK, Pedatella NM, Mullen ZK (2020) Interhemispheric coupling mechanisms in the middle atmosphere of WACCM6. J Atmos Sci 77(3):1101–1118

Smith CW, L'Heureux J, Ness NF, Acuña MH, Burlaga LF, Scheifele J (1998) The ACE magnetic fields experiment. Space Sci Rev 86(1):613–632

Solomentsev D, Jacobsen KS, Khattatov B, Khattatov V, Cherniak Y, Titov A (2015) Ionosphere data assimilation capabilities for representing the high-latitude geomagnetic storm event in September 2011. J Geophys Res Space Phys 119:10581–10594. https://doi.org/10.1002/2014JA020248

Spicher A, Clausen LBN, Miloch WJ, Lofstad JY, Moen JI (2017) Interhemispheric study of polar cap patch occurrence based on Swarm in situ data. J Geophys Res Space Phys 122:3837–3851. https://doi.org/10.1002/2016JA023750

Spiro RW, Wolf RA, Fejer BG (1988) Penetration of high latitude electric field effects to low latitudes during SUNDIAL 1984. Ann Geophys 6:39–49

Spogli L, Alfonsi L, De Franceschi G, Romano V, Aquino MHO, Dodson A (2009) Climatology of GPS ionospheric scintillations over high and mid-latitude European regions. Ann Geophys 27(9):3429–3437

Spogli L, Ghobadi H, Cicone A, Alfonsi L, Cesaroni C, Linty N, Romano V, Cafaro M (2021) Adaptive phase detrending for GNSS scintillation detection: a case study over Antarctica. IEEE Geosci Remote Sens Lett. https://doi.org/10.1109/LGRS.2021.3067727

Stauning P (1996) Investigations of ionospheric radio wave absorption processes using imaging riometer techniques. J Atmos Terr Phys 58:753–764. https://doi.org/10.1016/0021-9169(95)00072-0

Stauning P (2013) The polar cap index: a critical review of methods and a new approach. J Geophys Res Space Phys 118(8):5021–5038

Stephenson JAE, Walker ADM (2002) HF radar observations of Pc5 ULF pulsations driven by the solar wind. Geophys Res Lett 29(9):8–1

Stubbe P, Kopka H, Lauche H, Rietveld MT, Brekke A, Holt O, Jones TB, Robinson T, Hedberg Å, Thide B, Crochet M (1982) Ionospheric modification experiments in northern Scandinavia. J Atmos Terr Phys 44(12):1025–1041

Swarnalingam N, Wu DL, Gopalswamy N (2022) Interhemispheric asymmetries in ionospheric electron density responses during geomagnetic storms: a study using space-based and ground-based GNSS and AMPERE observations. J Geophys Res Space Phys 127(5):e2021JA030247

Tanskanen EI (2009) A comprehensive high-throughput analysis of substorms observed by IMAGE magnetometer network: years 1993–2003 examined. J Geophys Res 114(5):A05204. https://doi.org/10.1029/2008JA013682

Tassev Y, Velinov PIY, Tomova D, Mateev L (2017) Analysis of extreme solar activity in early September 2017: G4 – severe geomagnetic storm (07÷08.09) and GLE72 (10.09) in solar minimum, Comptes rendus de l'Acadèmie bulgare des Sciences, 70(10):1437–1444

Tesema F, Partamies N, Tyssøy HN, McKay D (2020) Observations of precipitation energies during different types of pulsating aurora. Ann Geophys 38:1191–1202. https://doi.org/10.5194/angeo-38-1191-2020

Themens DR, Jayachandran PT, Galkin I, Hall C (2017) The empirical Canadian high arctic ionospheric model (E-CHAIM): NmF2 and hmF2. J Geophys Res Space Phys 122:9015–9031. https://doi.org/10.1002/2017JA024398

Themens DR, Jayachandran PT, McCaffrey AM, Reid B, Varney RH (2019) A bottomside parameterization for the empirical Canadian high arctic ionospheric model. Radio Sci 54:397–414. https://doi.org/10.1029/2018RS006748

Thomas EG, Baker JBH, Ruohoniemi JM, Clausen LBN, Coster AJ, Foster JC, Erickson PJ (2013) Direct observations of the role of convection electric field in the formation of a polar tongue of ionization from storm enhanced density. J Geophys Res-Space 118:1180–1189. https://doi.org/10.1002/jgra.50116

Thomas EG, Shepherd SG (2018) Statistical patterns of ionospheric convection derived from mid-latitude, high-latitude, and polar SuperDARN HF radar observations. J Geophys Res Space Phys. https://doi.org/10.1002/2018JA025280

Thomson NR, Clilverd MA, McRae WM (2007) Nighttime ionospheric D region parameters from VLF phase and amplitude. J Geophys Res Space Phys, 112(A7)

Titova EE, Demekhov AG, Pasmanik DL, Trakhtengerts VY, Manninen J, Turunen T, Rycroft MJ (2007) Ground-based observations at L~ 6 of multi-band structures in VLF hiss. Geophys Res Lett 34:L02112. https://doi.org/10.1029/2006GL028482

Torr MR, Torr DG (1973) The seasonal behaviour of the F2-layer of the ionosphere. J Atmos Terr Phys 35:2237–2251. https://doi.org/10.1016/0021-9169(73)90140-2

Triana-Gómez AM, Heygster G, Melsheimer C, Spreen G, Negusini M, Petkov BH (2020) Improved water vapour retrieval from AMSU-B and MHS in the Arctic. Atmos Meas Tech 13(7):3697–3715

Troshichev OA, Andrezen VG (1985) The relationship between interplanetary quantities and magnetic activity in the southern polar cap. Planet Space Sci 33(4):415–419

Troshichev OA, Janzhura A, Stauning P (2006) Unified PCN and PCS indices: method of calculation, physical sense, and dependence on the IMF azimuthal and northward components. J Geophys Res Space Phys, 111(A5).

Troshichev OA, Podorozhkina NA, Sormakov DA, Janzhura AS (2014) PC index as a proxy of the solar wind energy that entered into the magnetosphere: (1) Development of magnetic substorms. J Geophys Res Space Phys. https://doi.org/10.1002/2014JA019940

Troshichev OA, Sormakov DA (2015) PC index as a proxy of the solar wind energy that entered into the magnetosphere: (2) Relation to the interplanetary electric field EKL. Earth Planets Space 67:170. https://doi.org/10.1186/s40623-015-0338-4

Troshichev OA, Sormakov DA (2018) PC index as a proxy of the solar wind energy that entered into the magnetosphere: (3) Development of magnetic storms. J Atmos Solar- Terr Phys 180:60–77. https://doi.org/10.1016/j.jastp.2017.10.012

Troshichev OA, Sormakov D, Behlke R (2018) Relationship between PC index and magnetospheric field-aligned currents measured by Swarm satellites. J Atmos Solar-Terr Phys 168:37–47. https://doi.org/10.1016/j.jastp.2017.12.020

Troshichev OA, Sormakov DA (2019a) PC index as a proxy of the solar wind energy that entered into the magnetosphere: (4) Relationship between the solar wind dynamic pressure (PSW) impulses and PC, AL indices. J Atmos Solar-Terr Phys 182:200–210. https://doi.org/10.1016/j.jastp.2018.12.001

Troshichev OA, Sormakov DA (2019b) PC index as a proxy of the solar wind energy that entered into the magnetosphere: (5) Verification of the solar wind parameters presented at OMNI website. J Atmos Solar-Terr Phys 196:105147. https://doi.org/10.1016/j.jastp.2019.105147

Tsurutani B, Mannucci A, Iijima B, Abdu MA, Sobral JHA, Gonzalez W, Guarnieri F, Tsuda T, Saito A, Yumoto K, Fejer B, Fuller-Rowell TJ, Kozyra J, Foster JC, Coster A, Vasyliunas VM (2004) Global dayside ionospheric uplift and enhancement associated with interplanetary electric fields. J Geophys Res-Space 109:A08302. https://doi.org/10.1029/2003JA010342

Tsurutani BT, Verkhoglyadova OP, Mannucci AJ, Saito A, Araki T, Yumoto K, Tsuda T, Abdu MA, Sobral JHA, Gonzalez WD, McCreadie H, Lakhina GS, Vasyliunas VM (2008) Prompt penetration electric fields (PPEFs) and their ionospheric effects during the great magnetic storm of 30–31 October 2003. J Geophys Res-Space 113:A05311. https://doi.org/10.1029/2007JA012879

Turunen E, Matveinen H, Tolvanen J, Ranta H (1996) D-Region Ion Chemistry Model, In: Schunk RW (ed) STEP Handbook of Ionospheric Models, 1–25. Scostep

Turunen T, Cannon PS, Rycroft MJ (1980) ELF radio signals in the auroral ionosphere generated by non-linear demodulation of LF and/or MF transmissions. Nature 286(5771):375–377

Valentic T, Buonocore J, Cousins M, Heinselman C, Jorgensen J, Kelly J et al. (2013). AMISR the advanced modular incoherent scatter radar. In 2013 IEEE international symposium on phased array systems and technology IEEE, pp 659–663

Van de Kamp M, Seppälä A, Clilverd MA, Rodger CJ, Verronen PT, Whittaker I (2016) A model providing long-term datasets of energetic electron precipitation during geomagnetic storms. J Geophys Res 121:5366–5383. https://doi.org/10.1029/2015JA022224

Van Dierendonck AJ, Klobuchar J, Hua Q (1993) Ionospheric scintillation monitoring using commercial single frequency C/A code receivers. Proc ION GPS 93:1333–1342

Van Malderen R, Pottiaux E, Stankunavicius G, Beirle S, Wagner T, Brenot H, Bruyninx C (2018) Interpreting the time variability of world-wide GPS and GOME/SCIAMACHY integrated water vapour retrievals, using reanalyses as auxiliary tools, Atmos. Chem. Phys. Discuss. [preprint], https://doi.org/10.5194/acp-2018-1170

Vanlommel P, Van der Linden R (2017) STCE Newsletter 4 Sep 2017 – 10 Sep 2017, Published by the Solar-Terrestrial Centre of Excellence (STCE), https://www.stce.be/newsletter/pdf/2017/STCEnews20170915.pdf, Accessed 1 June 2021

Verhulst T, Altadill D, Mielich J, Reinisch B, Galkin I, Mouzakis A et al (2017) Vertical and oblique HF sounding with a network of synchronised ionosondes. Adv Space Res. https://doi.org/10.1016/j.asr.2017.06.033

Verronen PT (2006) Ionosphere-Atmosphere Interaction During Solar Proton Events, PhD thesis, Helsinki, Finland: Finnish Meteorological Institute, https://helda.helsinki.fi/bitstream/handle/10138/23151/ionosphe.pdf, Accessed 1 June 2021

Villante U, Vellante M, De Sanctis G (2000) An analysis of Pc3 and Pc4 pulsations at Terra Nova Bay (Antarctica). Ann Geophys 18(11):1412–1421. https://doi.org/10.1007/s00585-000-1412-0

Vickers H, Kosch MJ, Sutton E, Bjoland L, Ogawa Y, LaHoz C (2014) A solar cycle of upper thermospheric density observations from the EISCAT Svalbard Radar. J Geophys Res. https://doi.org/10.1002/2014JA019885

Viljanen A (1997) The relation between geomagnetic variations and their time derivatives and implications for estimation of induction risks. Geophys Res Lett 24(6):631–634

Viljanen A, Tanskanen E (2011) Climatology of rapid geomagnetic variations at high latitudes over two solar cycles. Ann Geophys 29(10):1783–1792

Volland H (1995) Longwave sferics propagation within the atmospheric waveguide. Handbook Atmos Electrodyn 2:65–93

Wagner T, Beirle S, Dörner S, Borger C, Van Malderen R (2021) Identification of atmospheric and oceanic teleconnection patterns in a 20-year global data set of the atmospheric water vapour column measured from satellites in the visible spectral range. Atmos Chem Phys 21:5315–5353. https://doi.org/10.5194/acp-21-5315-2021

Walker ADM, Pinnock M, Baker KB, Dudeney JR, Rash JPS (1998) Strong flow bursts in the nightside ionosphere during extremely quiet solar wind conditions. Geophys Res Lett 25(6):881–884

Wang Y, Zhang QH, Jayachandran PT, Moen J, Xing ZY, Chadwick R et al (2018) Experimental evidence on the dependence of the standard GPS phase scintillation index on the ionospheric plasma drift around noon sector of the polar ionosphere. J Geophys Res Space Phys 123(3):2370–2378

Wanliss JA, Showalter KM (2006) High-resolution global storm index: Dst versus SYM-H. J Geophys Res Space Phys, 111(A2)

Wannberg G, Wolf I, Vanhainen LG, Koskenniemi K, Röttger J, Postila M, Markkanen J, Jacobsen R, Stenberg A, Larsen R, Eliassen S (1997) The EISCAT Svalbard radar: a case study in modern incoherent scatter radar system design. Radio Sci 32(6):2283–2307

Weatherhead EC, Reinsel GC, Tiao GC, Meng XL, Choi D, Cheang WK et al (1998) Factors affecting the detection of trends: Statistical considerations and applications to environmental data. J Geophys Res 103(D14):17149–17161. https://doi.org/10.1029/98JD00995

Wenzel D, Berdermann J, Jakowski N (2016) Modelling of the solar eclipse of 20 March 2015 and its influence on VLF measurements at different radio transmissions. Jahrestagung der DGG und AEF, März 2016, Münster, 14–17 https://elib.dlr.de/104040/. Accessed 28 July 2022

Weygand JM (2009) Equivalent Ionospheric Currents (EICs) derived using the Spherical Elementary Currents Systems (SECS) technique at 10 sec Resolution in Geographic Coordinates . UCLA. https://doi.org/10.21978/P8D62B

Weygand JM, Amm O, Viljanen A, Angelopoulos V, Murr D, Engebretson MJ, Gleisner H, Mann I (2011) Application and validation of the spherical elementary currents systems technique for deriving ionospheric equivalent currents with the North American and Greenland ground magnetometer arrays. J Geophys Res 116:A03305. https://doi.org/10.1029/2010JA016177

Weygand JM, Engebretson MJ, Pilipenko VA, Steinmetz ES, Moldwin MB, Connors MG et al (2021) SECS analysis of nighttime magnetic perturbation events observed in Arctic Canada. J Geophys Res Space Phys. https://doi.org/10.1029/2021JA029839

Wernik AW, Alfonsi L, Materassi M (2007) Scintillation modeling using in situ data. Radio Sci 42(01):1–21

Wild U (1994) Ionosphere and geodetic satellite systems: permanent GPS tracking data for modelling and monitoring. Geodatischgeophysikalische Arbeiten in der Schweiz, 48, Schweizerische Geodatische Kommission, PhD thesis

Wilson T, Wiens D, Smalley B, Raymond C, Nyblade A, Huerta A, Dalziel I, Bevis M, Aster R and Anandakrishnan S, (2008) Polenet seismic and GPS network in West Antarctica, AGUFM, V11F-02

Yao Y, Liu L, Kong J, Zhai C (2016) Analysis of the global ionospheric disturbances of the March 2015 great storm. J Geophys Res Space Physics 121:12157–12170. https://doi.org/10.1002/2016JA023352

Yamauchi M, Sergienko T, Enell C-F, Schillings A, Slapak R, Johnsen MG et al (2018) Ionospheric response observed by EISCAT during the 6–8 September 2017 space weather event: overview. Space Weather 16:1437–1450. https://doi.org/10.1029/2018SW001937

Yamazaki Y, Kosch MJ, Ogawa Y (2017) Average field-aligned ion velocity over the EISCAT radars. J Geophys Res. https://doi.org/10.1002/2017JA023974

Yamazaki Y, Matthias V, Miyoshi Y, Stolle C, Siddiqui T, Kervalishvili G et al (2020) September 2019 Antarctic sudden stratospheric warming: quasi-6-day wave burst and ionospheric effects. Geophys Res Lett 47:e2019GL086577. https://doi.org/10.1029/2019GL086577

Yang Z, Morton YJ, Zakharenkova I, Cherniak I, Song S, Li W (2020) Global view of ionospheric disturbance impacts on kinematic GPS positioning solutions during the 2015 St. Patrick's Day Storm. J Geophys Res Space Phys 125(7):e2019JA027681

Yang Z, Mrak S, Morton Y (2020b) Geomagnetic storm induced mid-latitude ionospheric plasma irregularities and their implications for GPS positioning over North America: a case study, Proc. IEEE/ION PLANS meeting, 2020

Yeh KC, Liu CH (1982) Radio wave scintillations in the ionosphere. Proc IEEE 70(4):324–360

Yin P, Mitchell CN (2014) Improving the vertical electron density profile in ionospheric imaging at storm time: a case study on 25–27 September 2011. J Geophys Res Space Phys 119:7963–7971. https://doi.org/10.1002/2014JA019899

Yue X, Wan W, Liu L, Liu J, Zhang S, Schreiner WS, Zhao B, Hu L (2016) Mapping the conjugate and corotating storm-enhanced density during 17 March 2013 storm through data assimilation. J Geophys Res Space Phys 121:12202–12210. https://doi.org/10.1002/2016bJA023038

Zabotin NA, Wright JW, Zhbankov GA (2006) NeXtYZ: three-dimensional electron density inversion for dynasonde ionograms. Radio Sci 41

Zabotin N, Negrea C, Godin OA, Rietveld M, Bullett T, Zabotina L (2015) Thermospheric Gravity Wave Activity near Summer Solstice 2014 Based on Analysis of Tromsø Dynasonde Data. In EGU General Assembly Conference Abstracts, p 4029

Zhang QH, Zhang BC, Lockwood M, Hu HQ, Moen J, Ruohoniemi JM, Thomas EG et al (2013) Direct observations of the evolution of polar cap ionization patches. Science 339(6127):1597–1600

Zhang S-R, Erickson PJ, Coster AJ, Rideout W, Vierinen J, Jonah OF, Goncharenko LP (2019) Subauroral and polar traveling ionospheric disturbances during the 7–9 September 2017 storms. Space Weather. https://doi.org/10.1029/2019SW002325

Zhao B, Wan W, Liu L, Mao T, Ren Z, Wang M, Christensen AB (2007) Features of annual and semiannual variations derived from the global ionospheric maps of total electron content. Ann Geophys 25:2513–2527. https://doi.org/10.5194/angeo-25-2513-2007

Zou S, Moldwin MB, Ridley AJ, Nicolls MJ, Coster AJ, Thomas EG, Ruohoniemi JM (2014) On the generation/decay of the storm-enhanced density (SED) plumes: role of the convection flow and field-aligned ion flow. J Geophys Res 119:543–8559. https://doi.org/10.1002/2014JA020408

Zou S, Ridley A, Jia X, Boyd E, Nicolls M, Coster A, Thomas E, Ruohoniemi JM (2017a) Multi-instrument observations of intense ion upflow fluxes associated with SED observed during the June 1, 2013 geomagnetic storm. J Geophys Res. https://doi.org/10.1002/2016JA023697

Zou S, Ozturk D, Varney R, Reimer A (2017b) Effects of sudden commencement on the ionosphere:PFISR observations and global MHD simulation. Geophys Res Lett 44:3047–3058. https://doi.org/10.1002/2017GL072678

Zou S, Perry GW, Foster JC (2021a) Recent Advances in Polar Cap Density Structure Research. In: Huang C, Lu G, Zhang Y, Paxton LJ (eds) Ionosphere Dynamics and Applications. https://doi.org/10.1002/9781119815617.ch4

Zou S, Ren J, Wang Z, Sun H, Chen Y (2021) Impact of storm-enhanced density (SED) on ion upflow fluxes during geomagnetic storm. Front Astron Space Sci. https://doi.org/10.3389/fspas.2021.746429

Authors and Affiliations

Lucilla Alfonsi[1] · Nicolas Bergeot[2] · Pierre J. Cilliers[3] · Giorgiana De Franceschi[1] · Lisa Baddeley[4] · Emilia Correia[5,6] · Domenico Di Mauro[1] · Carl-Fredrik Enell[7] · Mark Engebretson[8] · Reza Ghoddousi-Fard[9] · Ingemar Häggström[7] · Young-bae Ham[10] · Georg Heygster[11,12] · Geonhwa Jee[10] · Antti Kero[13] · Michael Kosch[3,14,15] · Hyuck-Jin Kwon[10] · Changsup Lee[10] · Stefan Lotz[3] · Liliana Macotela[16,17] · Maria Federica Marcucci[18] · Wojciech J. Miloch[19] · Y. Jade Morton[20] · Takahiro Naoi[21] · Monia Negusini[22] · Noora Partamies[4,23] · Boyan H. Petkov[24,25] · Eric Pottiaux[2] · Paul Prikryl[26] · P. R. Shreedevi[27] · Rikard Slapak[7] · Luca Spogli[1,28] · Judy Stephenson[14] · Arantxa M. Triana-Gómez[11] · Oleg A. Troshichev[29] · Roeland Van Malderen[30] · James M. Weygand[31] · Shasha Zou[32]

1. Istituto Nazionale di Geofisica e Vulcanologia, 00143 Rome, Italy

2. Royal Observatory of Belgium, 1180 Brussels, Belgium

3. South African National Space Agency, Hermanus 7200, South Africa

4. University Centre in Svalbard, 9170 Longyearbyen, Norway

5. Instituto Nacional de Pesquisas Espaciais, São Paulo 12227-010, Brazil

6. CRAAM-Universidade Presbiteriana Mackenzie, São Paulo 01302-907, Brazil

7. EISCAT Scientific Association, 98128 Kiruna, Sweden

8. Department of Physics, Augsburg University, Minneapolis, MN 55454, USA

9. Canadian Geodetic Survey, Natural Resources Canada, Ottawa K1A0Y7, Canada

10. Korea Polar Research Institute, Incheon 21990, South Korea

11. Institute of Environmental Physics, University of Bremen, 28334 Bremen, Germany

12. Geophysical Remote Sensing Lab (GEORG-Lab), 28209 Bremen, Germany

13. Sodankylä Geophysical Observatory, University of Oulu, 99600 Sodankylä, Finland

14. School of Chemistry and Physics, University of KwaZulu-Natal, Durban 3209, South Africa

15. Physics Department, Lancaster University, Lancaster LA14YB, UK

16. Centre for Space, Atmospheric and Oceanic Science, University of Bath, Bath BA27AY, UK

17. Leibniz-Institute of Atmospheric Physics at the University of Rostock, 18225 Kühlungsborn, Germany

18. INAF-Istituto di Astrofisica e Planetologia Spaziali, 00133 Rome, Italy

19. Department of Physics, University of Oslo, 0371 Oslo, Norway

20. University of Colorado, Boulder 80309, USA

21. Space Environment Laboratory, Applied Electromagnetic Research Institute, National Institute of Information and Communications Technology, Tokyo 184-8795, Japan

22. Istituto di Radioastronomia, Istituto Nazionale di Astrofisica, 40129 Bologna, Italy

23. Birkeland Centre for Space Science, University of Bergen, 5007 Bergen, Norway

24. Dipartimento di Tecnologie Innovative in Medicina e Odontoiatria, Università degli Studi "G. D'Annunzio", 66100 Chieti-Pescara, Italy

25. Istituto di Scienze Polari, Consiglio Nazionale delle Ricerche, 40129 Bologna, Italy

26. University of New Brunswick, Fredericton E3B5A3, Canada

[27] Institute for Space Earth Environment Research (ISEE), Nagoya University, Nagoya 464-8601, Japan

[28] SpacEarth Technology, 00143 Rome, Italy

[29] Arctic and Antarctic Research Institute, St.Petersburg, Russia 199397

[30] Royal Meteorological Institute of Belgium, 1180 Brussels, Belgium

[31] Department of Earth, Planetary, and Space Sciences, University of California, Los Angeles, CA 156704, USA

[32] Department of Climate and Space Sciences and Engineering, University of Michigan, Ann Arbor 48109-2143, USA